NTNU
Norwegian University of
Science and Technology

Computed Tomography of Chemiluminescence in interacting reacting flows

Tomas Falkhytten

Mechanical Engineering
Submission date: June 2018
Supervisor: Nicholas Worth, EPT

Norwegian University of Science and Technology
Department of Energy and Process Engineering

O NTNU

Norwegian University
of Science and Technology

Department of Energy
and Process Engineering

EPT-M-2018-29

MASTER THESIS

for

Tomas Falkhytten

Spring 2018

Computed Tomography of Chemiluminescence in interacting reacting flows

Background and objective

While planar and standard integrated measurement techniques such as OH-PLIF and OH*
imaging can provide significant insight into combustion processes, previous studies have
demonstrated that closely confined flames in an annular chamber subject to transverse excitation
exhibit a number of significant asymmetries. Computed tomography of chemiluminescence
(CTC) is a promising new technique in which multiple chemiluminescence images are recorded
from different angles, and a tomographic reconstruction algorithm is applied in order to
transform these 2D projections into a 3D chemiluminescence distribution. As CTC has only
previously been applied to open flames, during the current project the technique will be
developed for use in closely confined flames, with the ultimate goal of characterising the full
three-dimensional structure and dynamics of flames in an annular combustor.

The project will involve taking an existing Matlab based tomographic reconstruction code,
generalizing it to handle large data sets, and run in parallel threads. A numerical study will also
be conducted in order to assess and optimize the experimental setup. Preparatory testing will also
be conducted in order to assess camera calibration methods, and also to evaluate the influence of
reflection and refraction effects of quartz glass confinement geometry. Finally a series of
measurements will be conducted in the forced annular combustor setup, and reconstructions of
the mean and phase averaged heat release distribution will be obtained and analysed.

The following tasks are to be considered:

Literature Review
1. Background reading and literature review of thermos-acoustic instabilities in single and multi-
flame configurations.
2. Background reading and literature review of CTC methods and other similar investigations.

Programming and numerical investigations
1. Generalise the existing Matlab based tomographic reconstruction code to handle large
   data sets and parallelize implementation.
2. Conduct a numerical study assessing the effect of experimental setup parameters on the
   tomographic reconstruction of a representative known scalar field.

Experimental tasks
1. Perform calibration testing on a simplified experimental mock-up, and use this to evaluate the effects of reflection and refraction from the quartz glass enclosure.
2. Perform experimental measurements of the reacting flow in the annular combustor setup, and reconstruct the three-dimensional distribution of heat release.

Within 14 days of receiving the written text on the master thesis, the candidate shall submit a research plan for his project to the department.

When the thesis is evaluated, emphasis is put on processing of the results, and that they are presented in tabular and/or graphic form in a clear manner, and that they are analyzed carefully.

The thesis should be formulated as a research report with summary both in English and Norwegian, conclusion, literature references, table of contents etc. During the preparation of the text, the candidate should make an effort to produce a well-structured and easily readable report. In order to ease the evaluation of the thesis, it is important that the cross-references are correct. In the making of the report, strong emphasis should be placed on both a thorough discussion of the results and an orderly presentation.

The candidate is requested to initiate and keep close contact with his/her academic supervisor(s) throughout the working period. The candidate must follow the rules and regulations of NTNU as well as passive directions given by the Department of Energy and Process Engineering.

Risk assessment of the candidate's work shall be carried out according to the department's procedures. The risk assessment must be documented and included as part of the final report. Events related to the candidate's work adversely affecting the health, safety or security, must be documented and included as part of the final report. If the documentation on risk assessment represents a large number of pages, the full version is to be submitted electronically to the supervisor and an excerpt is included in the report.

Pursuant to "Regulations concerning the supplementary provisions to the technology study program/Master of Science" at NTNU §20, the Department reserves the permission to utilize all the results and data for teaching and research purposes as well as in future publications.

The final report is to be submitted digitally in DAIM. An executive summary of the thesis including title, student's name, supervisor's name, year, department name, and NTNU's logo and name, shall be submitted to the department as a separate pdf file. Based on an agreement with the supervisor, the final report and other material and documents may be given to the supervisor in digital format.

☒ Work to be done in lab (Water power lab, Fluids engineering lab, Thermal engineering lab)
☐ Field work

Department of Energy and Process Engineering, 15. January 2018

Nicholas Worth
Academic Supervisor

Preface

This report presents the project conducted as part of my Master's Thesis in Mechanical Engineering during the spring of 2018, and concludes my years at the Norwegian University of Science and Technology. The project presents the attempt to reconstruct 3D OH* Chemiluminescence distribution of a single flame confined by an annular combustion chamber.

I would like to use this opportunity to thank my supervisor, Associate Professor Nicholas Worth, for the possibility to work on such an interesting project for my Master's Thesis, and for all the valuable feedback, guidance and discussions throughout the project. I would also like to thank, PhD Candidate Håkon Tormodsen Nygård, and Postdoctoral Fellow Marek Mazur, for helping me with my experiments and all the valuable discussions regarding them.

Trondheim, 11.06.2018

Tomas Falkhytten

Abstract

Computed Tomography of OH* Chemiluminescence of a single flame confined by an annular combustion chamber have been demonstrated in this thesis. 3D heat release structures were reconstructed for both unforced and acoustically forced flames.

A phantom study was performed. The methodology of the study was first thoroughly presented, before a parametric study was conducted. How camera configurations, calibration errors and reflections influenced reconstruction qualities of the implemented tomographic methods were investigated. These tests revealed that maximizing view width of the camera configuration was crucial to the final reconstruction quality. They also indicated strong coherence between reconstruction quality and processing sequence of erroneous data.

A mock experiment was used to investigate possible problems with camera calibrations. The tests showed that refraction due to the annular quartz enclosure deteriorated the calibration accuracy. The experimental methods of the Computed Tomography of OH* Chemiluminescence of the single flame confined in an annular combustion chamber were then presented. Acoustic drivers were used to force an azimuthal instability mode in the annular chamber.

3D heat release structures were reconstructed for both an unforced, and acoustically forced flame. For the unforced flame, the mean structure showed asymmetries in the heat release likely caused by limited view width and inaccurate bluff-body positioning in the burner. 12 phase-averaged volumes were reconstructed for the acoustically forced flame, spanning over a full oscillation cycle of an azimuthal mode with a mean spin ratio, $SR = 0.26$.

The results showed complicated 3D flame dynamics for acoustically forced flame. Based on the azimuthal mode characterization, the complex flame dynamics is caused by the ACW spinning component of the azimuthal mode hitting the flame brush from the side.

Despite promising results, further work needs to be done to validate the results with other experimental methods like OH-PLIF, and improve camera calibrations procedures.

Sammendrag

Computertomografi av OH* luminescens av en flamme innelukket i et ringformet forbrenningskammer er blitt demonstrert i denne avhandlingen. 3D varmefrigjøringsfordelingsstrukturer ble rekonstruert for både frie, og akustisk tvungne flammer.

Et fantomstudie ble gjort. Metodologien av studien ble først grundig presentert før en parameterstudie ble gjennomført. Hvordan kamerakonfigurasjoner, kalibreringsfeil, og refleksjoner påvirket rekonstruksjonskvaliteten til de implementerte tomografiske metodene ble undersøkt. Det ble funnet at å maksimere synsbredden til kamerakonfigurasjonen var avgjørende for den endelige rekonstruksjonskvaliteten. Indikasjoner på sammenhenger mellom rekonstruksjonskvalitet og prosesseringsrekkefølgene av feilaktige data ble også funnet.

Et forenklet eksperiment ble brukt for å undersøke mulige kalibreringsproblemer. Tester viste at refraksjon grunnet det ringformede kvarts glasset forverret kalibreringsnøyaktigheten. Videre ble oppsettet for computertomografi av OH* luminescens av en flamme innelukket i et ringformet forbrenningskammer presentert. Akustiske drivere ble brukt til å tvinge en asimut ustabilitetsmodus i det ringformede kammeret.

3D varmefrigjøringsfordelingsstrukturer for frie og akustisk tvungne flammer ble rekonstruert. For den frie flammen viste gjennomsnittsstrukturen asymmetrier i varmefordelingen, trolig grunnet begrenset synsvidde og unøyaktigheter i forbrenningskammeret. 12 fasegjennomsnittsvolumer, fordelt over en full oscillasjonssyklus, ble rekonstruert for den akustiske tvungne flammen. Den asimute ustabilitetsmodusen ble karakterisert av det gjennomsnittlige spinn forholdet, $SR = 0.26$.

Resultatene avslørte en komplisert 3D flammedynamikk for de tvungne flammene. Basert på ustabilitetsmodusanalysen er den kompliserte dynamikken forårsaket av at den spinnende komponenten av ustabilitetsmodusen treffer flammen fra siden.

Til tross for lovende resultater kreves det mer arbeid for å validere dem med andre eksperimentell metoder som OH-PLIF, samt arbeid angående forbedring av kalibreringsmetodene.

Contents

Chapter 1

Introduction

1.1 Motivation

Annular combustion system are commonly found in gas turbines used both for power genera-
tion, and propulsion in aircraft. These systems are designed to operate in stable regimes, how-
ever, sometimes unexpected oscillations are exhibited in these combustion chambers, leading
to noise and vibrations (Poinsot, 2017). Such instabilities are known as thermoacoustic combus-
tion instabilities (CIs). In the design of new, low emission gas turbines, lean operating conditions
are desired in order to reduce NO_x combustion products. Unfortunately, turbines operating in
such conditions are more prone to thermoacoustic CIs (Krebs et al., 2002).

One major reason for CIs causing problems in the development of new engines is that they
often occur during later stages in the development process and are difficult to predict (Oefelein
and Yang, 1993). Due to the geometry of annular combustion chambers, instabilities tend to
excite in azimuthal modes since the longest dimension is formed by the circumference. The
underlying mechanisms causing these modes are not well understood, but recent numerical
studies utilizing LES (Staffelbach et al. (2009), Wolf et al. (2012)), and experiments using simpli-
fied annular combustion chambers (Worth and Dawson (2013a), Worth and Dawson (2013b))
are beginning to uncover some of these mechanisms.

The azimuthal modes occur when azimuthal acoustic waves couples with fluctuating heat
release, resulting in self-reinforcing pressure fluctuations which grow in amplitude before reach-
ing a limit cycle. Such azimuthal modes can be spinning clockwise (CW) or anti clockwise

(ACW), or be a standing wave. Both experiments (Dawson and Worth, 2014) and simulations (Wolf et al., 2012) confirms that modes can degenerate and switch between characteristics over time.

To investigate these instabilities found in annular combustion chambers high-speed OH* chemiluminescence imaging have been used to investigate fluctuations in heat release rate (Worth and Dawson, 2013a). While high-speed OH-PLIF have been used to investigate flame dynamics (Dawson and Worth, 2014). Another experimental method used to investigate turbulent combustion is Computed Tomography of Chemiluminescence (CTC). This technique reconstructs a 3D chemiluminescence field of a flame based on several camera images assumed to be integral measurements of the chemiluminescence from the flame (Floyd et al., 2011). Application of this method in the investigation of azimuthal modes in annular combustion chambers have not yet been reported to the authors knowledge.

This thesis aims to utilize CTC to investigate spatial distribution of OH* chemiluminescence from a single flame confined in an annular combustor. Attempts to reconstruct a single unforced flame, and an acoustically forced flame will be done. A parametric phantom study will also be performed to guide and optimize the experimental setup, and to uncover potential problems with the methodology of the reconstruction.

1.2 Background - Thermoacoustic instabilities in annular combustion chambers

1.2.1 Gas turbines

The typical gas turbine used in both power generation and in the aviation industry consists of a compressor, combustion chamber and turbine, as illustrated in figure 1.1. Air is compressed through several stages through the compressor increasing the pressure, before entering the combustion chamber. Fuel is added to the air, and the mixture is ignited resulting in a high temperature flow of combustion gases. The energy in the gases are converted to rotational mechanical energy in the turbine stages. In gas turbines used for propulsion of aircraft, the exhaust gases are used to generate propulsion, while in gas turbines generating electric power extract

excess mechanical energy from the turbine shaft.
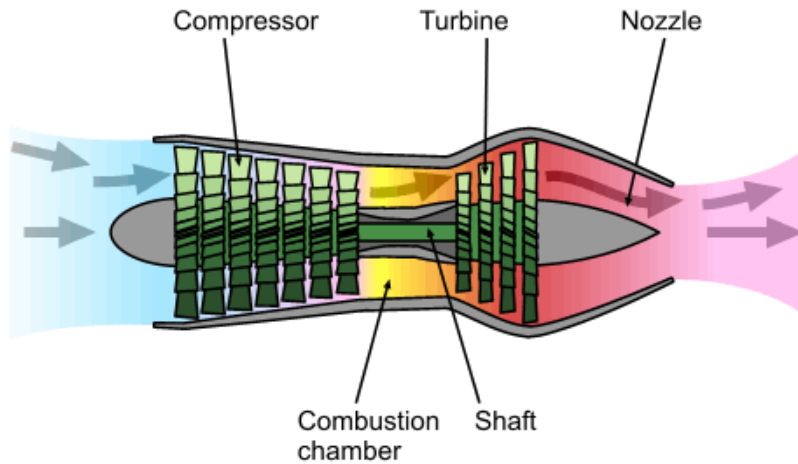
Figure 1.1: Illustration of a axial flow turbojet engine. (Reproduced from Commons (2005), under the CC BY 2.5 license)

In figure 1.2, three simplified different types of combustion chambers are illustrated. Modern aircraft gas turbines are commonly designed using the annular architecture, as this is the ideal configuration in terms of compact dimensions (Saravanamuttoo et al., 2009). In the annular combustion chamber the nozzles are equidistant distributed around the annulus, and not separated by can dividers.
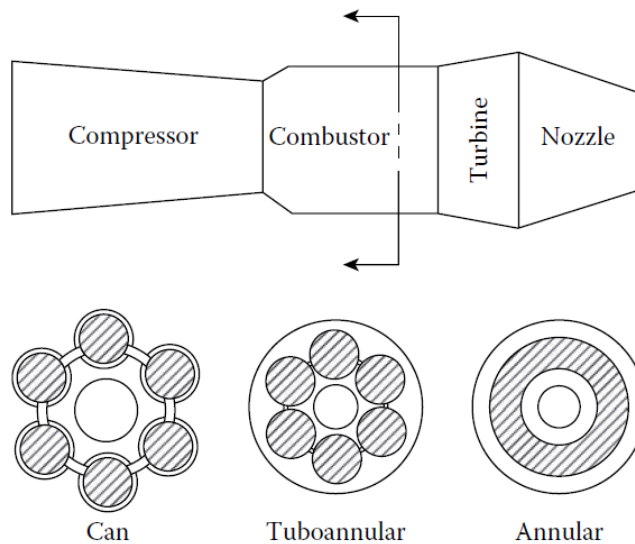
Figure 1.2: Illustration of three different combustor types. (Reproduced from Arthur H. Lefebvre (2010))

The demand for low emission gas turbines is growing, forcing the industry to design gas turbines operating at leaner conditions, in order to reduce especially nitrogen oxides, or NO_x gases. The leanness of fuel-air mixtures can be described by the equivalence ratio, ϕ, and is expressed as the inverse of the stochiometric ratio, λ.

$$\phi = \frac{1}{\lambda} \tag{1.1}$$

When $\phi < 1$, the fuel-air mixture is considered to be lean.

Unfortunately, the development of such turbines are often accompanied by problems with oscillating combustion (Arthur H. Lefebvre, 2010). This has led to a growing interest in research regarding combustion instabilities in annular chambers.

1.2.2 Thermoacustic instabilities

Almost 150 years ago the basic mechanisms leading to combustion instabilities were identified by Lord Rayleigh (1878). Since then, research regarding combustion instabilities, first in rockets (Crocco, 1951), and then jet engines (Putnam, 1971), have been done. Older studies have mostly been limited to combustion chambers with a single burner according to Poinsot (2017), but the geometry of annular combustion chambers fed by multiple burners introduces new thermoacoustic problems. Due to the annular geometry of the chamber, azimuthal instability modes may occur. According to Ghirardo and Juniper (2013) it is this instability mode that tend to develop because of the length of the circumference is much longer compared to the width and length of the chamber. The azimuthal modes are acoustic waves traveling in the clockwise (CW) and anticlockwise (ACW) azimuthal directions. When these waves couples with fluctuations in the heat release from the burners, the modes become self-excited (Worth and Dawson, 2013a). This coupling is illustrated in figure 1.3

The azimuthal modes may be standing, spinning clockwise (CW) or anticlockwise (ACW), or a combination of these. If the azimuthal mode is considered to be a pair of 1D acoustic waves travelling in opposite directions around the annular chamber, $\mathbb{R}(p_k)$ describes the pressure oscillations at all azimuthal locations, θ_k, when p_k is defined by:
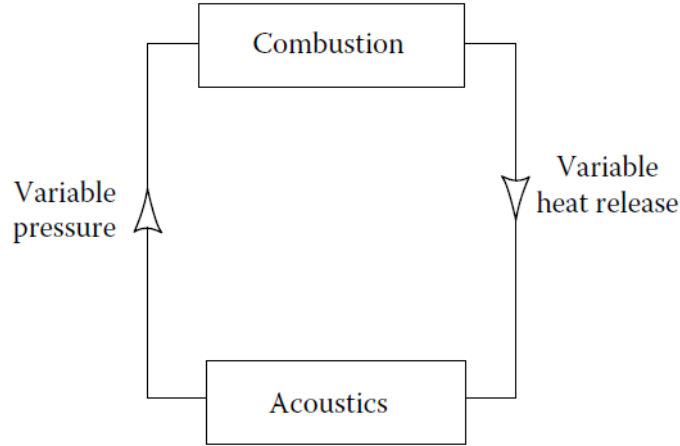
Figure 1.3: Schematic representation of the coupling between acoustics and combustion. (Reproduced from Arthur H. Lefebvre (2010))

$$p_k = \left[A_+ \cdot e^{i(\theta_k - v_\theta t/R)} + A_- \cdot e^{i(-\theta_k + v_\theta t/R)} \right] \cdot e^{-i\omega t} \tag{1.2}$$

where A_+ and A_- are the amplitudes of the ACW and CW azimuthal acoustic waves respectively, and positive real values. R is the radius of the annulus, ω the annular frequency and v_θ is the azimuthal velocity of the nodal line (Worth et al., 2017). The spin ratio, SR, introduced by Bourgouin et al. (2013), can be used to characterize the azimuthal mode. The spin ratio is defined by:

$$SR = \frac{A_+ - A_-}{A_+ + A_-} \tag{1.3}$$

With this definition, $SR = 0$ indicates a pure standing mode, while $SR = 1$ and $SR = -1$ corresponds to purely spinning modes in ACW and CW directions respectively. Modes can be a combination of spinning and standing, and are often categorized by the predominant mode. If $A_+ > 2A_-$, the mode is considered predominately ACW spinning, while for a predominately CW spinning mode $A_- > 2A_+$. In terms of the spin ratio this means the mode is predominantly spinning ACW and CW, when $SR > 1/3$ and $SR < -1/3$ respectively, while it is considered predominately standing if $-1/3 < SR < 1/3$.

1.2.3 Recent research

Recent research have shown that these modes degenerate over time. Amplitude and phase show time-varying behavior, resulting in the azimuthal modes changing over time. Staffelbach et al. (2009) used Large Eddy Simulations (LES) to model a self-excited instability in an annular combustion chamber where the oscillations grew naturally before reaching a limit cycle. Later, LES performed by Wolf et al. (2012) predicted time-varying behavior of the azimuthal mode, suggesting the modes to change between spinning and standing over time. This behavior was later reproduced experimentally by Worth and Dawson (2013a), using a simplified annular combustion chamber, which is illustrated in figure 1.4 (left image). An example of the azimuthal mode analysis performed is given by the same figure (right image).
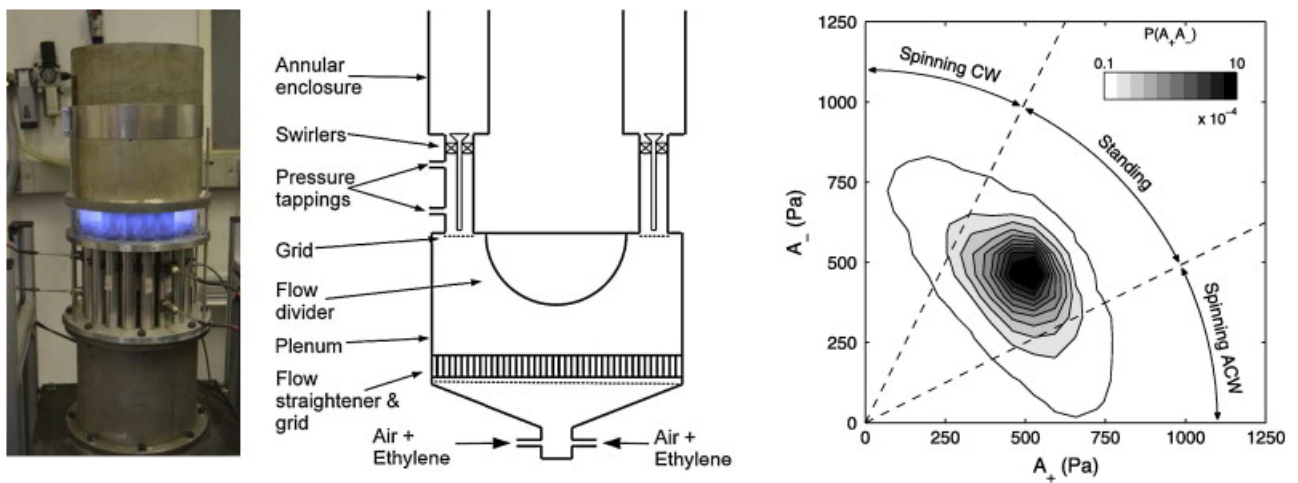
Figure 1.4: Left and center: Configuration of the Cambridge annular combustion chamber. Right: Example of a joint probability distribution function of the azimuthal mode for a certain burner configuration. (Reproduced from Worth and Dawson (2013a))

Experimental results presented by Bourgouin et al. (2013) also confirmed this unsteadiness of the azimuthal mode. Their annular combustion chamber was equipped with clockwise swirlers at each burner. Spin ratios measured over a time series were presented, and the probability density function of spin ratios they observed are shown in figure 1.5. Note that $SR = 1$ in their results indicate a CW spinning mode. They observed a non-zero mean of the spin ratio, and suggested that the favored positive spin ratio was due to CW rotational direction of the swirlers. However, the results from Worth and Dawson (2013a) shows that other parameters than swirler direc-

tions play strong roles in mode behavior. How the flame separation distance, S, fundamentally changes the preferred modes for setup where all burners are equipped with ACW swirlers can be seen in figure 1.6. Worth and Dawson (2013a) attributed this changing mode preference to the spatial rearrangement of mean heat release rate, and how axisymmetry of each flame is reduced with reduced S. The preferred azimuthal mode can also change by varying the equivalence ratio, ϕ, as reported by Worth and Dawson (2017), confirming the complexity of predicting the preferred mode characteristic for a certain configuration.
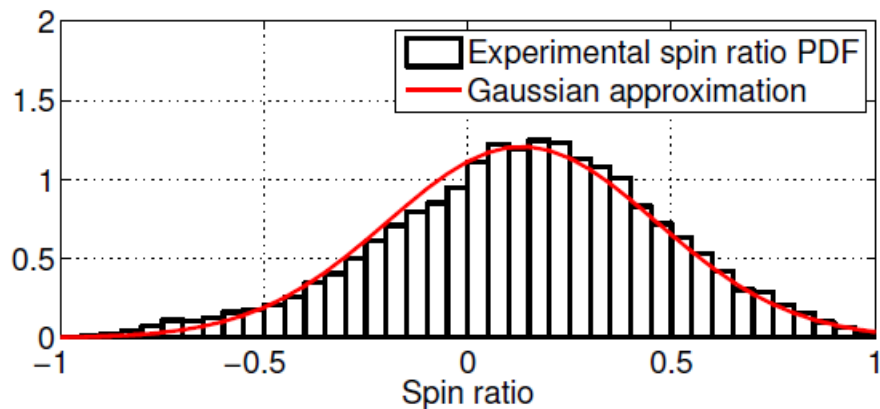
Figure 1.5: Probability density function of the spin ratio in experiments performed by Bourgouin et al. (2013).(Reproduced from Bourgouin et al. (2013))

The work elucidating the physical mechanisms of the azimuthal mode continues. Experimental techniques like high-speed OH* chemiluminescence imaging, can be utilized to investigate phase-averaged global heat release related to self-excited azimuthal modes (Worth and Dawson (2013a), Dawson and Worth (2014), Dawson and Worth (2015)). Measurements of OH* chemiluminescence are often used as an estimate of the global heat release, as done by Balachandran et al. (2005) and Palies et al. (2010) in order to construct flame transfer functions (FTF) or flame describing functions (FDF). To investigate the flame dynamics in annular chambers, phase-averaged OH planar laser-induced chemiluminescence (OH-PLIF) measurements have been used to get cross-sectional images of the interactions of adjacent flames (Dawson and Worth, 2014). It may be necessary to utilize other methods to get more insight into the underlying physics in order to gain a deeper understanding of the nature of the azimuthal modes.

(a) $S = 1.56D$, ACW Swirl   (b) $S = 1.87D$, ACW Swirl   (c) $S = 2.33D$, ACW Swirl

Figure 1.6: Joint probability density functions of A_+ and A_- for a setup with ACW swirlers and changing S. (Reproduced from Worth and Dawson (2013a))

1.3   Background - Computed Tomography of Chemiluminescence

To further increase the understanding of turbulent combustion, and guide the development of simulation techniques like LES, experimental methods able to capture the transient, three d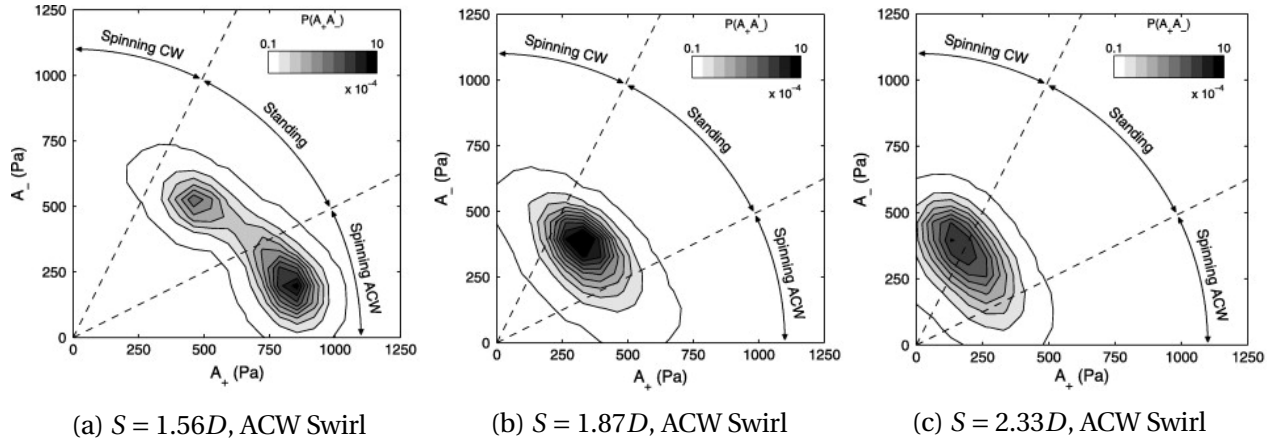imensional nature of the combustion physics are required. Computed tomography methods are well suited to resolve structures of 3D unsteady nature.

Some earlier use of tomographic methods in flame studies exists where 2D images were created by studying laser absorption phenomena to determine flame temperatures and relative concentrations of certain chemical compounds (Best et al. (1991), McNesby et al. (1995)). Also, 2D slice-reconstructions of chemiluminescence have been performed (Anikin et al., 2010).

More recent research have utilized tomographic methods to reconstruct full 3D flame structures. The general approach is to record images of chemiluminescence from several viewing angles. These images are assumed to be line integral projections of an unknown 3D intensity field, and by using different tomographic methods this 3D intensity field is recreated based on the 2D measurements.

Ishino and Ohiwa (2005) used MLEM (maximum likelihood expectation methods) to create 3D images of a turbulent, rich propane-air mixture, flame. Images were acquired using a 40-lens custom built camera. A similar setup was later used by Ishino et al. (2009) to investigate turbulent motion of the flame front and local burning velocities. Later, Upton et al. (2011) used multiplicative algebraic reconstruction methods (MART) to reconstruct the flame front of

a turbulent premixed propane-air flame. The work by Floyd et al. (2011) used a setup of 5 *commodity* cameras together with mirrors giving 10 simultaneous views of a premixed turbulent opposed jet flame. CTC using algebraic reconstruction techniques (ART) was performed, and showed that performing CTC was possible with lower equipment budgets due to the capabilities of newer machine vision cameras.

By repositioning a single camera to 48 positions, capturing the mean image of CH* chemiluminescence, Floyd and Kempf (2011) reconstructed the mean flame structure of a laminar matrix burner. Due to the need for only a single camera makes this approach very cost-efficient, although only mean structures are possible to reconstruct. Using a similar approach, Worth and Dawson (2013c) performed tomographic reconstructions of OH* chemiluminescence from two interacting turbulent flames. The flames they investigated were acoustically forced, and both mean- and phase-averaged images were recorded from 15 different views by re-positioning a single camera with an intensifier. Both phase-averaged and mean 3D structures were reconstructed using MART, and results compared to OH-PLIF and FSD measurements. The results showed that despite some differences, the reconstructed 3D structures captured both the mean flame structure, and the evolution of the phase-averaged dynamics of the acoustically forced flame. This proved that CTC can give useful information about the 3D unsteady, periodic flame dynamics, which are important in the investigation of combustion instabilities, using only a single camera.

Several other studies have used different methods of CTC in the investigation of unconfined flames (Ishino et al. (2016), Wang et al. (2016), Yu et al. (2017), Wiseman et al. (2017)). However, few have performed studies on confined flames which are normally found in practical applications such as industrial burners and gas turbine engines. Samarasinghe et al. (2013) investigated combustion of a five-nozzle can combustor. The five flames was placed in cross-configuration, stabilized by swirlers and confined by a quartz glass can. The imaging system and can combustor during operation are illustrated in figure 1.7

(a) Setup of camera and combustor

(b) Can combustor during operation
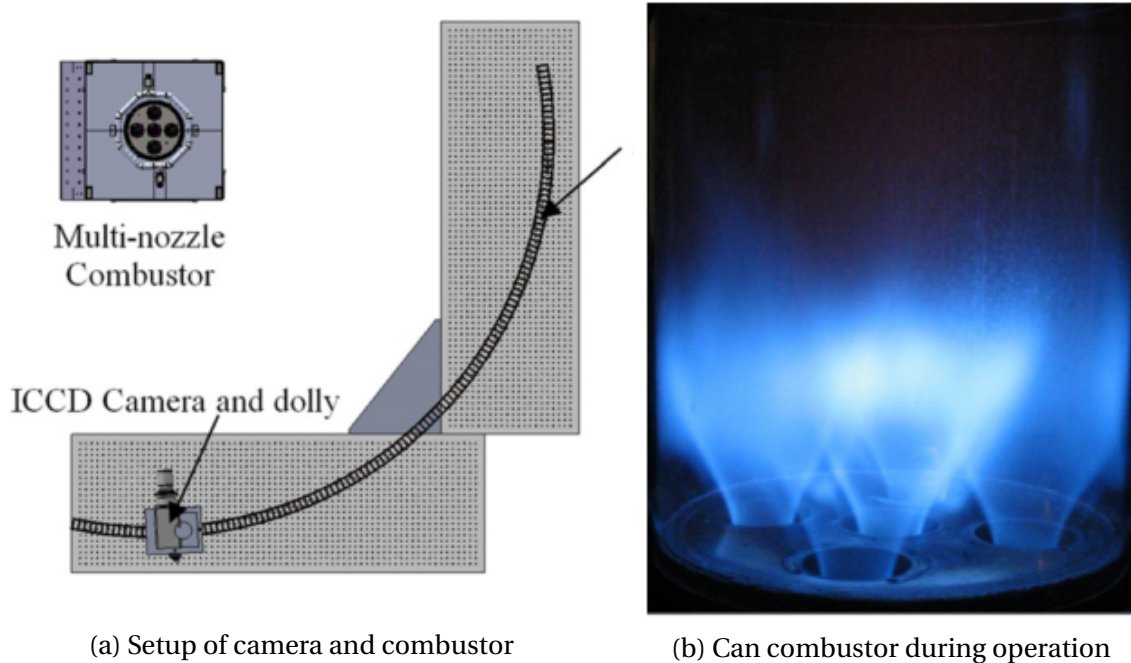
Figure 1.7: The setup used by Samarasinghe et al. (2013) to reconstruct five flames in an enclosed combustor. (Reproduced from Samarasinghe et al. (2013))

The flames was reconstructed using a filtered back projection algorithm performing an inverse Radon transform based on multi-angular projections. Horizontal slices from each images having the same z-position are used to create a 2D-slice of the volume. Doing this for all the horizontal slices, and combining these gave a volumetric measurement. This approach assumes that all the line-of-sight (LOS) of the pixels are parallel to each other. Placing the camera further away from the flame will strengthen this assumption. However, effects due to refraction between air and the quartz will affect the pixel's LOS, and has not been taken into consideration.

The study investigated both an unforced flame, and velocity forced flame. For the forced flame, amplitude of the flow of premixed fuel and air were varied 5% (u'_{rms}/u_{mean}), at a frequency of 100 Hz. Similar setup and reconstruction methods were used by Samarasinghe et al. (2015) to investigate flame-flame interaction and flame-wall interaction. To the author's knowledge, these are the only two studies using CTC to investigate confined flames.

Several of the problematic flame phenomena like the azimuthal instabilities found in annular combustion chambers only arise when the flames are enclosed by such a chamber. The enclosure makes utilizing methods like CTC, that are dependent on optical accessibility, challenging to use in investigation of such problems.

1.4   Objectives

The final goal of this thesis is to apply CTC to reconstruct 3D OH* chemiluminecensce distribution of a single flame confined in an annular combustion chamber. The flame will both be unforced and acoustically forced in order to investigate a forced azimuthal instability mode. In order to reach this goal several objectives have to be addressed.

Programming and numerical investigations

1. Implement the possibility to handle large data sets in an existing tomographic reconstruction MATLAB code.

2. Implement use of polynomial camera models into the same code.

3. Conduct a numerical study assessing the effect of experimental setup parameters on the tomographic reconstruction of a representative known scalar field.

Experimental tasks

1. Find a way to precisely reposition a calibration piece inside the experimental setup, and evaluate precision.

2. Use a simplified mock experiment in order to evaluate effects of refraction from the quartz glass enclosure.

3. Perform experimental measurements of a single reacting flow in the annular combustor setup, and reconstruct the three-dimensional distribution of heat release.

The following chapters will present the work done in order to fulfill these objectives. Chapter 2 will present the methodology of the parametric phantom study, and explain the outline of the full procedure, and how it differs from the real experiment. In chapter 3, results from the phantom study will be presented and discussed. Based on these results, experimental recommendations will be given. The experimental methods will be presented in chapter 4, including both a mock experiment, investigating potential setup problems, and the final experiment where CTC will be applied to a flame enclosed in an annular chamber. Results from both these experiment

are presented in chapter 5 and discussed. Conclusion of the work presented, and recommended further work is found in chapter 6.

Chapter 2

Phantom Study - Methodology

In this chapter, the setup of a synthetic experiment performing reconstructions of a phantom object will be presented and explained. The reasons for doing a phantom study are both to verify the reconstruction code, and to test how different experimental setup parameters impact reconstruction quality, thus being able to optimize the final experimental setup. The reconstruction code is a modified version of the code used by Falkhytten (2017). Modifications done to the code involves implementing the possibility to handle larger data sets, and implementation of an alternative camera model. The core-reconstruction code are MEX-functions written in *C*, while the rest of the framework of the synthetic experiments is written in MATLAB.

2.1 Setup of the synthetic experiments

The steps of the synthetic computed tomography of chemiluminescence experiment are illustrated in figure 2.1. First pinhole models representing cameras are specified, these are used to generate the synthetic data. Then, a phantom object representing the flame in form of an intensity field over a 3D voxel space is created. Further, synthetic experimental images of the phantom images are created based on the phantom object using the camera models. Also synthetic calibration images are generated using phantom calibration plates and the camera models. Calibration of the camera models are then done using the synthetic calibration images in order to relate each pixel to 3D space. Based on the camera calibrations and synthetic phantom images a tomographic reconstruction of the phantom object is performed. The reconstruction quality

is evaluated by comparing the reconstructed object to the generated phantom object.

This methodology is similar to that of the final experiment, but all images in the synthetic experiments are generated, while in a real experiment they would be acquired from the experimental setup. The following sections will explain each step in the procedure, and simplifications and assumptions done will be clarified.
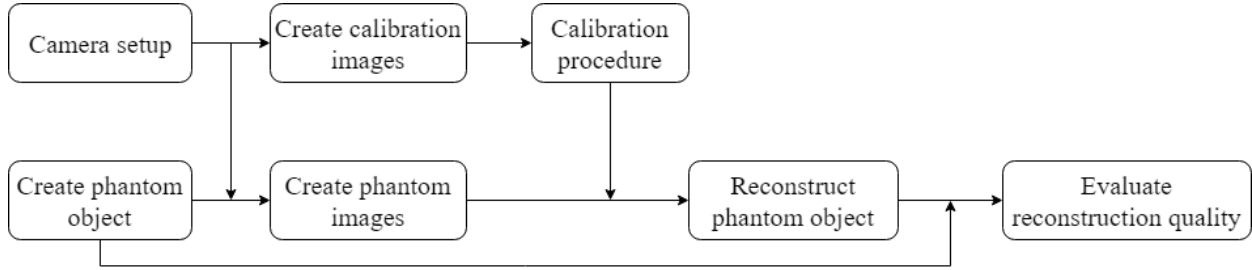
Figure 2.1: The steps of a tomographic reconstruction of a phantom object in a synthetic experiment.

2.1.1 Camera setup

Cameras in the synthetic experiment were set up in an arc configuration, where all cameras were located in the XZ-plane. The setup of the camera configuration is defined by the number of cameras, N_c, the angle between the outermost cameras, β, and the distance between the cameras and the origin, r. Camera model 1 to N_c are generated, and all are aimed toward the global origin. The angle between neighbouring cameras, α, is defined by the other parameters as:

$$\alpha = \frac{\beta}{N_c - 1} \tag{2.1}$$

How these parameters control the camera setup is illustrated in figure 2.2.

2.1.2 Camera model

In the synthetic experiments the cameras were modelled as pinhole models. The principles of this model are illustrated in figure 2.3. These models of the cameras were used to create artificial images of both the phantom object and of the calibration plate. Using such a model for image
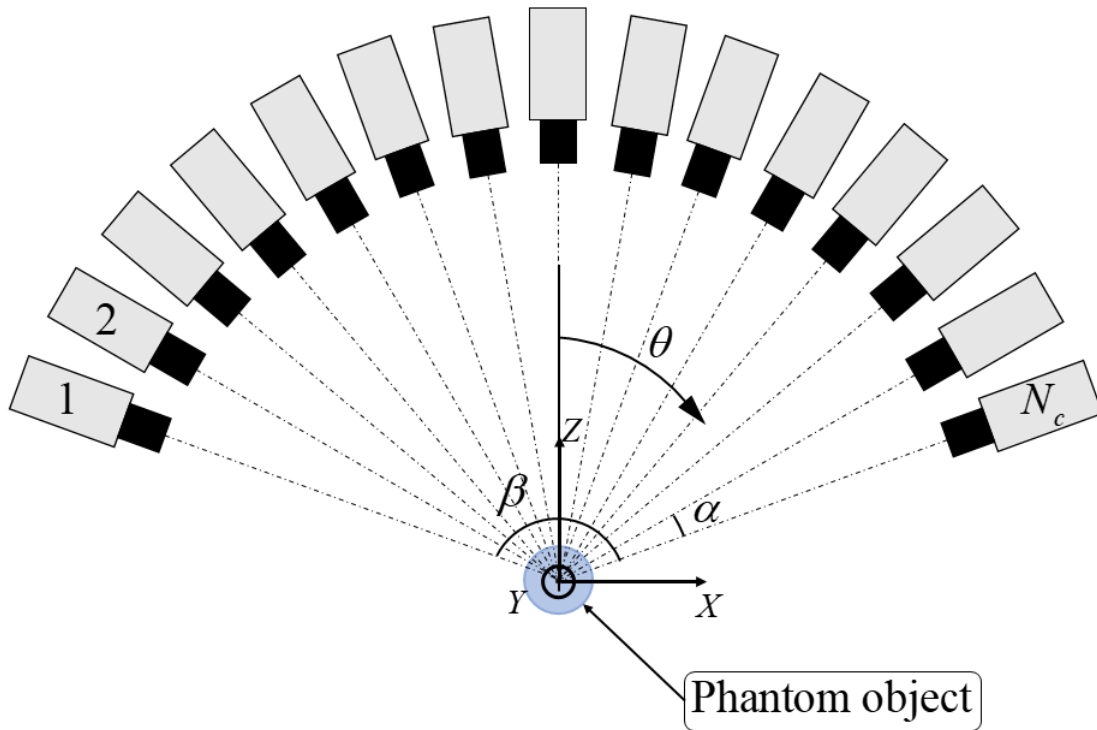
Figure 2.2: The arc configuration setup. All cameras are placed in the xz-plane, r away from the global origin. N_c cameras are equally spaced over the span of β. [STOR XYZ for å være konsistent]

generation implicates some simplifications and idealizations (Young, 1971) of the images, these are:

- No distortion due to no lens.

- Infinitesimal pinhole, but no diffraction.

- Field of focus is infinite.

The pinhole model consists of both extrinsic and intrinsic parameters. Extrinsic parameters describes the 3D position and orientation of the cameras. In the synthetic experiment, 3D positions depends on the given β and N_c, while all cameras were oriented such that the *principal point*, *center of projection* and *global origin* all lied on the same straight line. The intrinsic parameters, *focal length*, *principle point* and *image sensor format* were determined by the user. How these parameters are set will determine other parameters such as *Magnification, M*. The intrinsic parameters used in the phantom study is given in table 2.1.

Table 2.1: Intrinsic parameters

Focal length	$f = 30mm$
Image sensor format	$1mm \times 1mm$
Resolution	400×400 pixels
Principal point	$[200, 200]$

The pinhole models can be used to relate images to 3D space, which is necessary for the tomographic reconstruction. For most of the tests performed in the phantom study, the pinhole model was used due to how it simplifies the testing of many different setup cases. However, another model was also implemented and tested for some cases because this model was the one used in the final experiments. This other model is described in section 2.1.6.
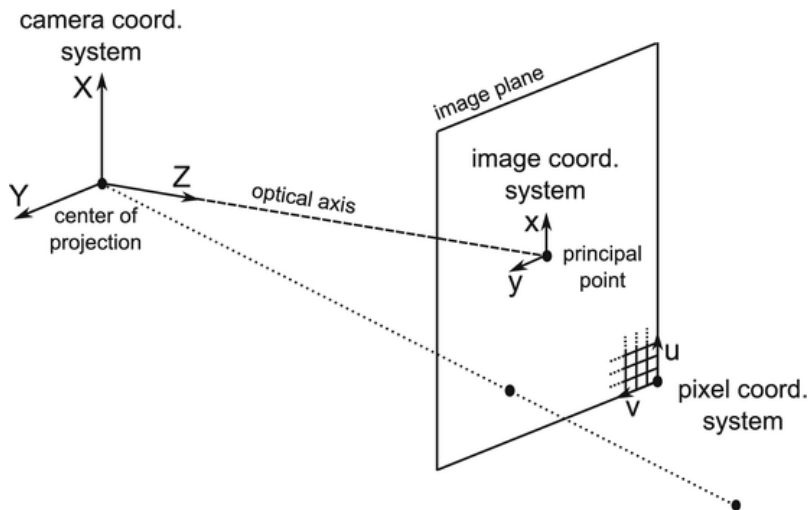
Figure 2.3: A pinhole model. Center of projection is the pinhole were light is projected through onto the image plane. *Focal length* is the distance between the *principal point* and the pinhole. *Image sensor format* is the size of the image plane. (Reproduced from Sturm (2014))

2.1.3 Create phantom object

For the synthetic experiment, a phantom object representative of a flame was created. It was based on a mean image of a swirling flame reproduced from Mazur et al. (2018). The raw image is illustrated in figure 2.4. To create the 3D phantom the image was first cropped and gray-scaled, giving us an image seen in figure 2.5a. It was assumed that the light represented in a pixel is the integrated chemiluminescence, or light amount, over the line-of-sight of that pixel through the flame. The flame in the image was also assumed axisymmetric. Based on these assumption, a

modified inverse Abel transformation (Kasim et al., 2015) was applied on the image to calculate the cross-section of the flame.
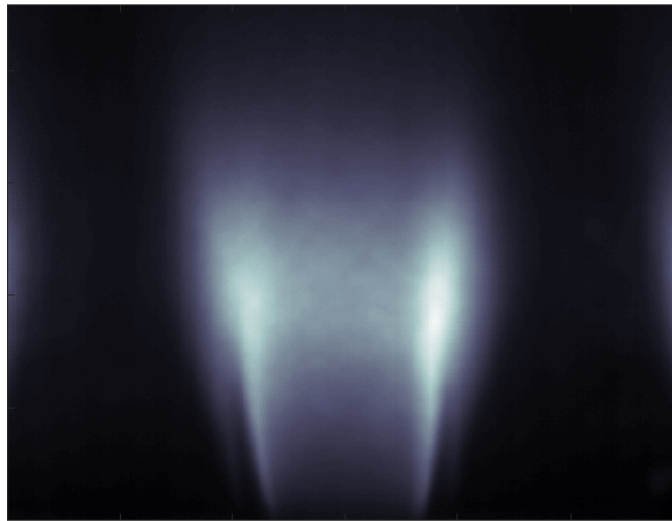
Figure 2.4: A mean image of a non-swirling flame from the side. (Reproduced from Mazur et al. (2018))

The resulting image can be observed in figure 2.5b. The image was further processed by applying a threshold filter to it where all pixels below 20% of the maximum value in the image is set to be 0. All pixels close to the symmetry axis were set to be zero as it was assumed no chemiluminescence are to be found here, and because the utilized transformation procedure generate noise close to the symmetry axis. The resulting filtered image is illustrated in figure 2.5c.

The resulting cross section was then used to generate an axisymmetric phantom flame in a discretized 3D voxel space. The reconstruction program creates a 3D voxel light intensity distribution, therefore, the phantom object was constructed in the same manner so they are easily comparable.

The voxel space was defined by setting limits of the space in $X-$, $Y-$ and $Z-$direction, and the number of voxels per mm. Based on these inputs, a volume having the form of a rectangular prism was created. Voxel values were represented by a 3D-array of doubles, and each voxel was assigned a global position, (X, Y, Z), based on the volume limits and the number of voxels per mm. The discretization of the voxel space was set to be equidistant.

Further, the image of the flame cross section was given spatial limits to relate the pixels to

(a) Cropped original image   (b) Transformed image   (c) Filtered transformed image
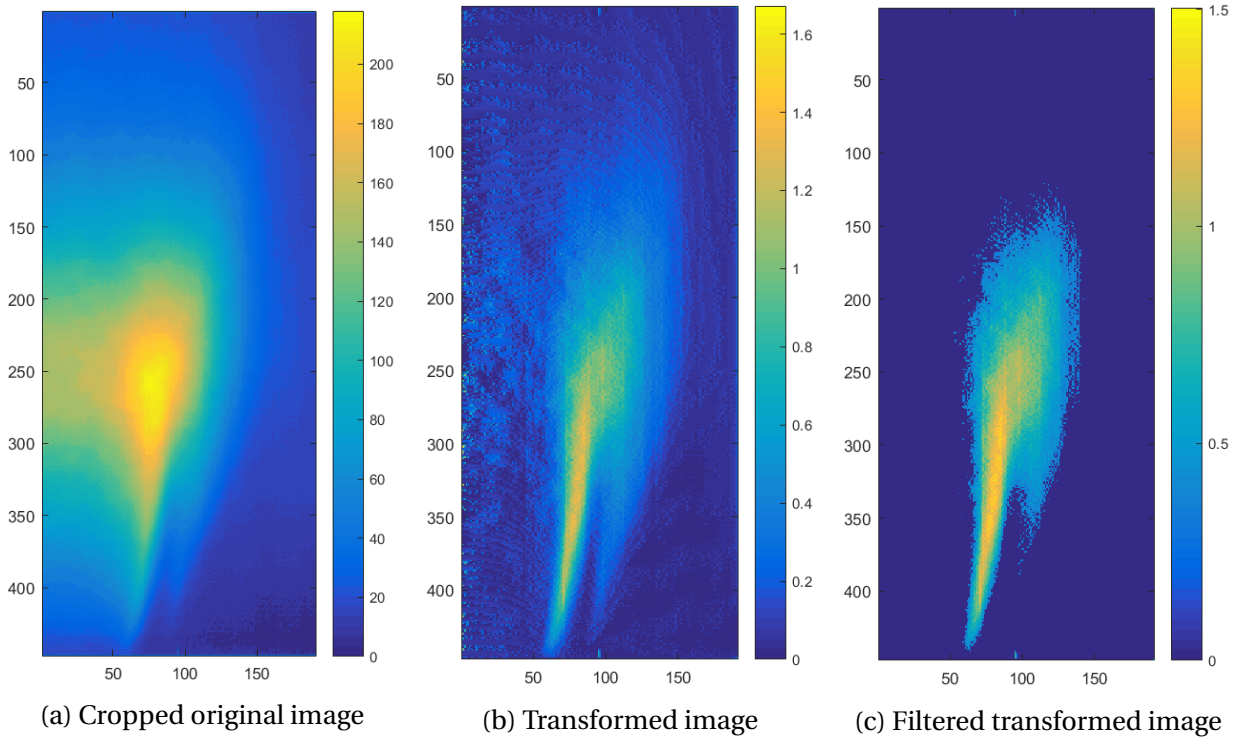
Figure 2.5: Images of the flame from figure 2.4 after processing. Cropping and grayscaling gives figure 2.5a. The inverse Abel transform gives figure 2.5b. Threshold filtering this, gives figure 2.5c

3D space. Each pixel was given a r−coordinate, and a Y-coordinate, which was the axis of symmetry for the phantom object. The image was then swept around the Y-axis. The voxels of the volume were assigned values based on the pixel values and distance between the pixels and the voxels. Each XZ−plane of the discrete voxel space was related to a strip of pixels from the image. If the Y−position of the XZ-slice lies between two strips of pixels, a new pixel strip based on the two neighbouring strips and linear interpolation was created. Each voxel in the current plane was assigned an intensity value, $E_g(X, Y, Z)$, based the pixel values and the position of the voxel in relation to the pixels. If a voxel lied between two pixels, a linear interpolation of the pixel values was also applied here to assign the voxel a value. To visualize the structure of the 3D phantom object several slices are presented in figure 2.7. Figure 2.6 show the position of the slices presented.

From the XY-slices it is observed that slices from $\pm Z$-values are equal to each other, as expected due to the axisymmetry. The axisymmetry of the XZ-slices is also apparent, but some irregularity are observed, probably due to the discretization of both the Abel transformed origi-
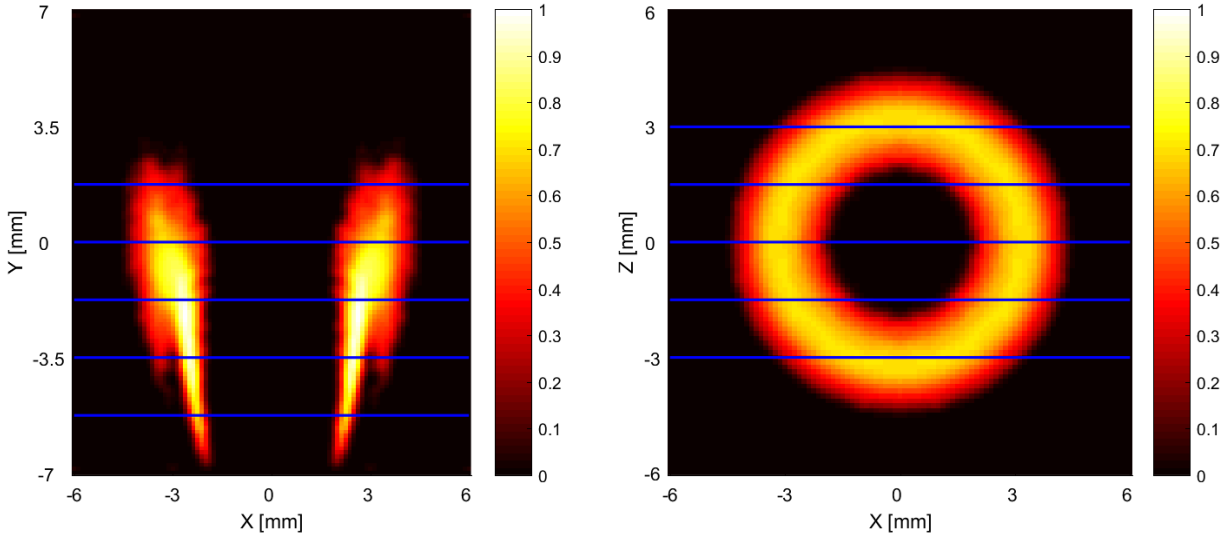
(a) Slice in xy-plane at $z = 0$

(b) Slice in xz-plane at $y = 0$

Figure 2.6: The blue lines indicate where the slices in figure 2.6 are located

nal image and the volume.
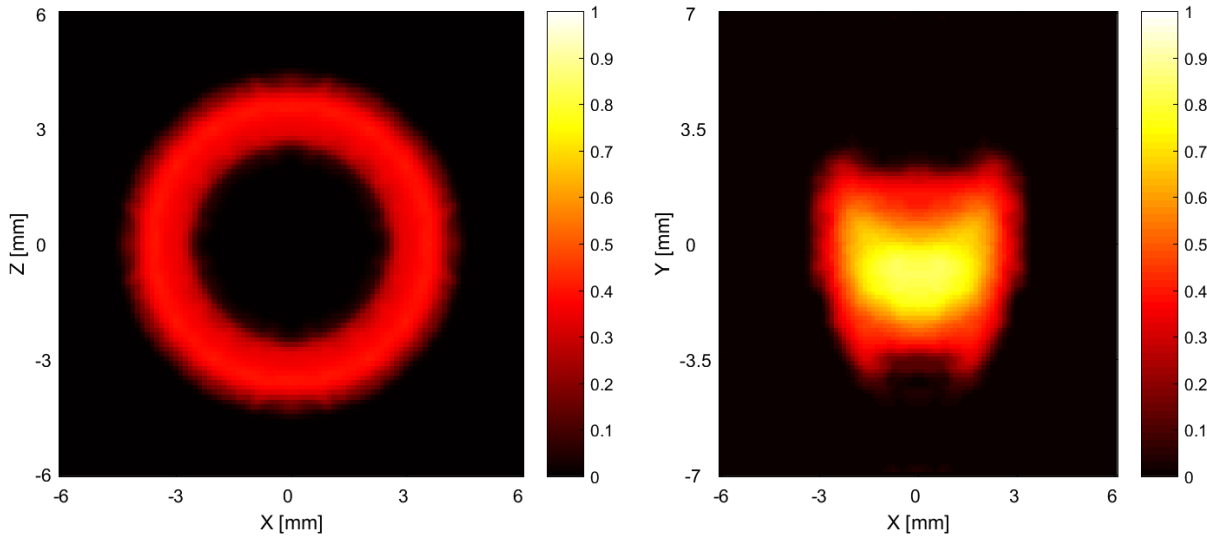
(a) xz-slice at $y = 1.75$mm

(b) xy-slice at $z = 3.0$mm
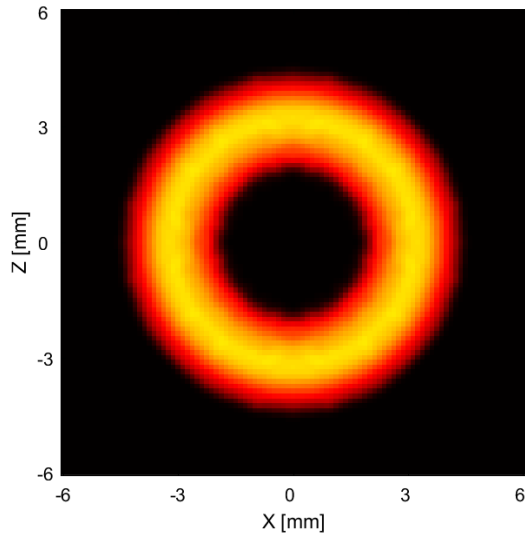
(c) *xz*-slice at *y* = 0mm
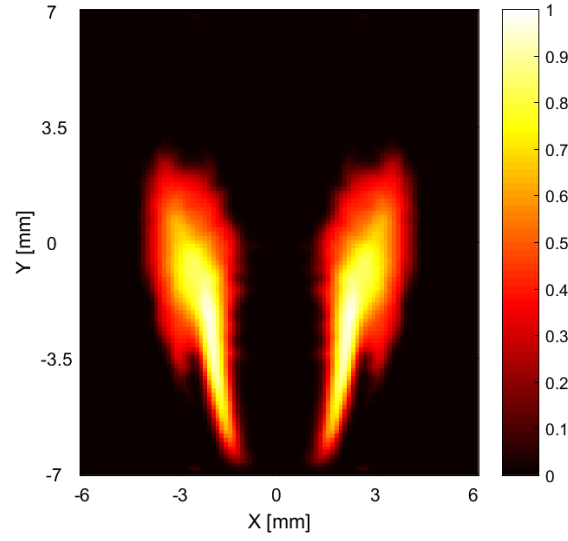
(d) *xy*-slice at *z* = 1.5mm
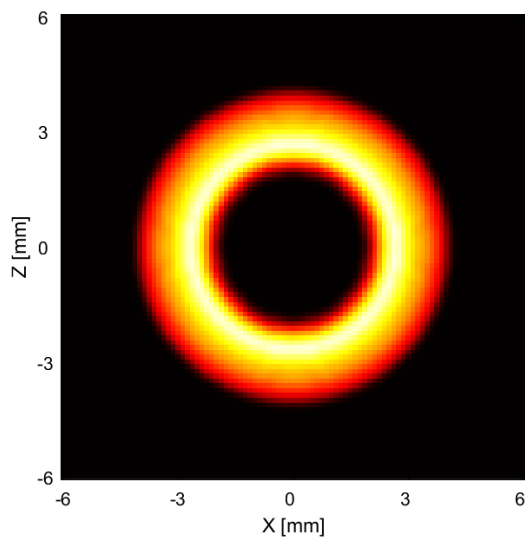
(e) *xz*-slice at *y* = −1.75mm

(f) *xy*-slice at *z* = 0.0mm

(g) *xz*-slice at *y* = −3.5mm

(h) *xy*-slice at *z* = −1.5mm

(i) *xz*-slice at *y* = −5.25mm
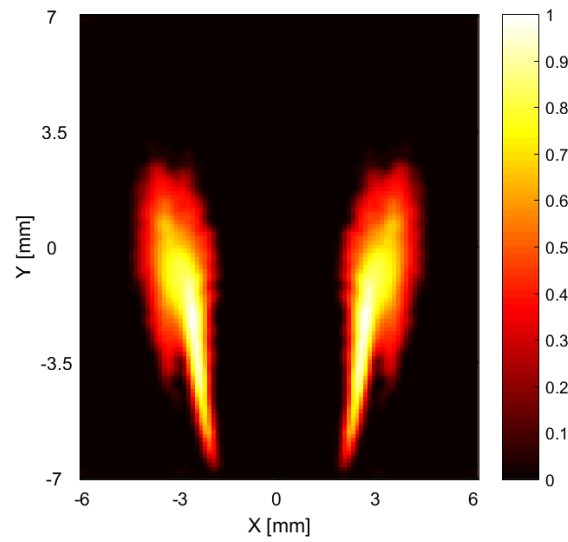
(j) *xy*-slice at *z* = −3.0mm
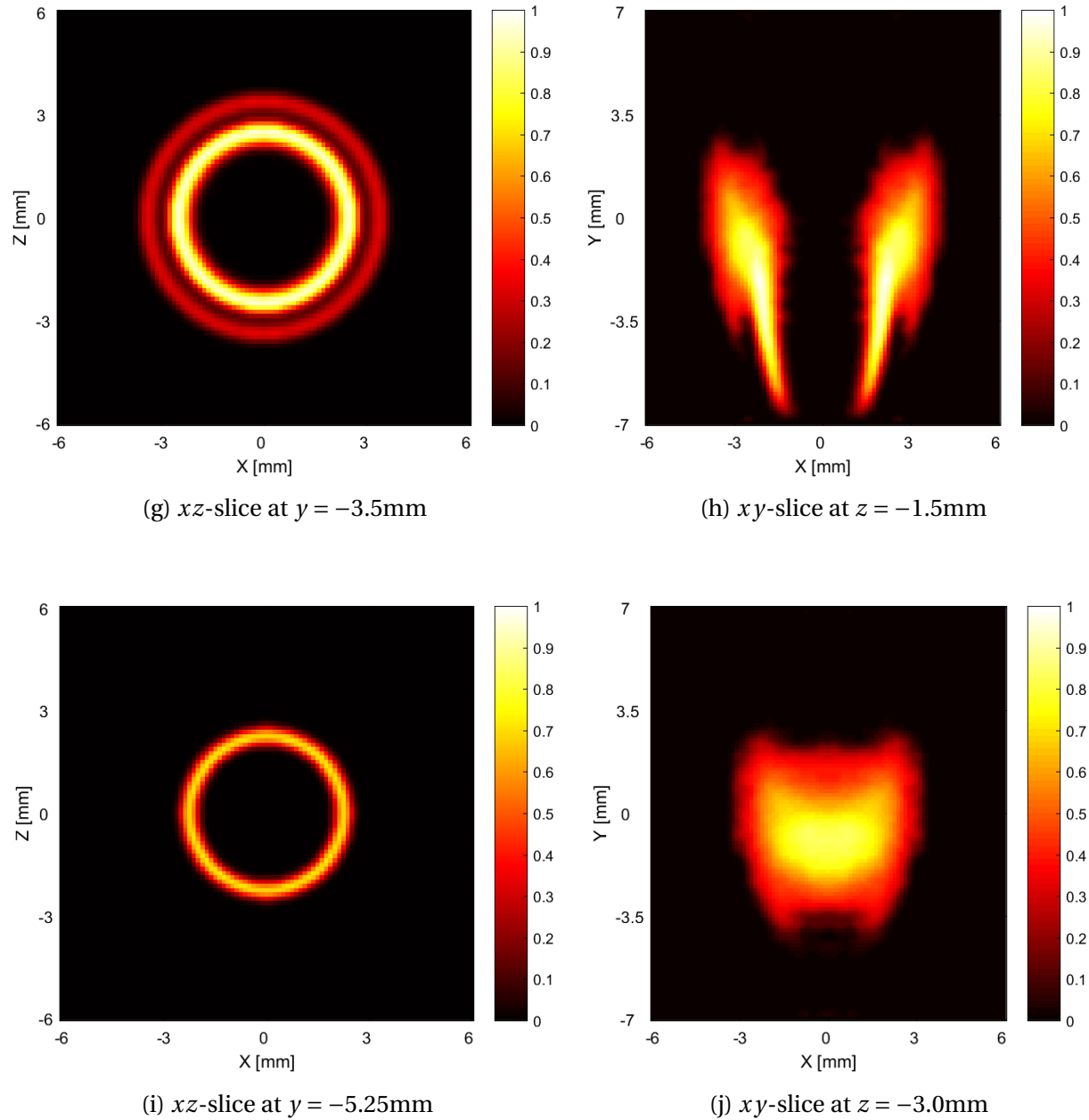
Figure 2.7: Slices of the phantom object.

2.1.4 Image generation

Each image for the respective camera was created by projecting the generated 3D light intensity voxel volume using the respective camera models into an image. The voxel's intensity was spread across the image sensor pixels based on a 2D Gaussian function to account for the discrete image sensor. Doing this for all the voxels for all cameras results in the final images. An

example of such an image is illustrated in figure 2.8. Since the images were based on the generated intensity volume and the pinhole camera models, assumptions made there were also be propagated to the images. They are,

- No image noise.

- No distortion

- All chemiluminescence relevant for a pixel's line-of-sight (LOS) is captured by the pixel.

- No optical inhomogeneities.
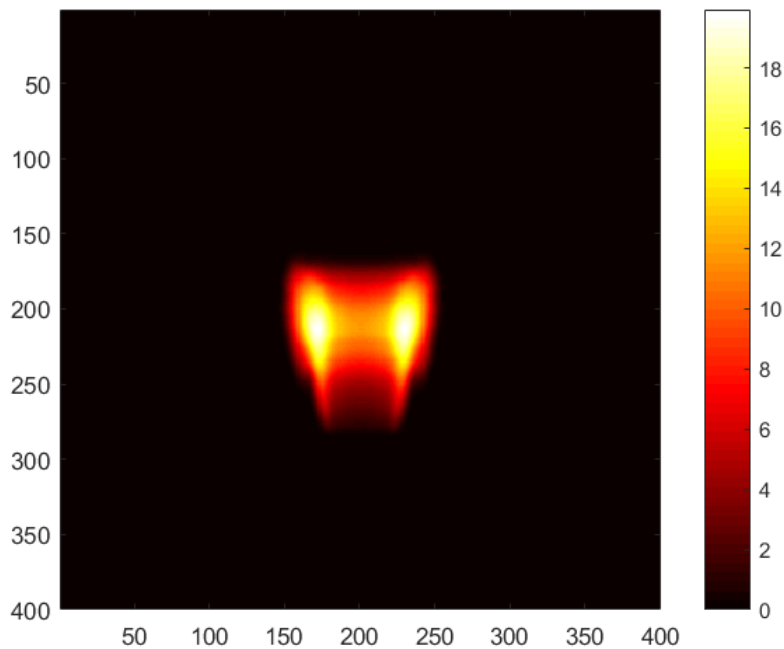
Figure 2.8: A generated synthetic image of the phantom object.

2.1.5   Create calibration images

2.1.5.1   Camera models

To perform a reconstruction of the phantom object based on the generated images, the 2D images needs to be related to the 3D space. A point, $\boldsymbol{P} = (X, Y, Z)$, where (X, Y, Z), are the coordinates in physical space, was to be related to a point in the image plane of the ith camera, $\boldsymbol{p}'_i = (x, y)$,

$$(x_i, y_i) = M_i(X, Y, Z) \tag{2.2}$$

where M_i is the mapping function relating these two domains (Soloff et al., 1997).

The two most common models used are a pinhole model (Y. Tsai, 1987) or a polynomial model (Soloff et al. (1997), Prasad (2000)). It would be possible to use the same pinhole models used to create the synthetic images as the mapping function to relate the images to the volume. Doing this would mean that doing a calibration procedure would not be necessary since the parameters of the pinhole model was already set and known.

Both models have been implemented and used in this study. The pinhole model was used when performing reconstruction test were numerous camera numbers and arc widths were investigated due to no need for human input into the calibration procedure since the pinhole model parameters are already known. The polynomial model was used for some specific cases to test reconstruction capabilities of the program, since this camera model were to be used in later experiments. Calibration of this model is further explained in the next sections.

2.1.5.2 Calibration plate

To perform a calibration of a camera model, images of a known calibration object with a known location in space were needed. To create such images, a synthetic calibration plate was generated. The plate was represented by a 2D-array of voxels, where each voxel was given a position in $X-$ and $Y-$direction. A pattern of dots was specified by positions in the XY-plane and by a diameter. If a voxel in the 2D-array was within the circumference of one of the dots, it was given the value 1, if not, the voxel value was set to 0. The resulting array represented the calibration plate with a specified dot pattern and is visualized by figure 2.9.

2.1.5.3 Calibration images

Next step in the procedure was to generate images of the calibration plate placed at two different $Z-$positions in the volume of interest. The plate was placed at a specified $Z-$position, giving the voxels representing the plate a spatial placement in all directions. Each voxel of the plate was then projected into the calibration image using the pinhole models in the same man-
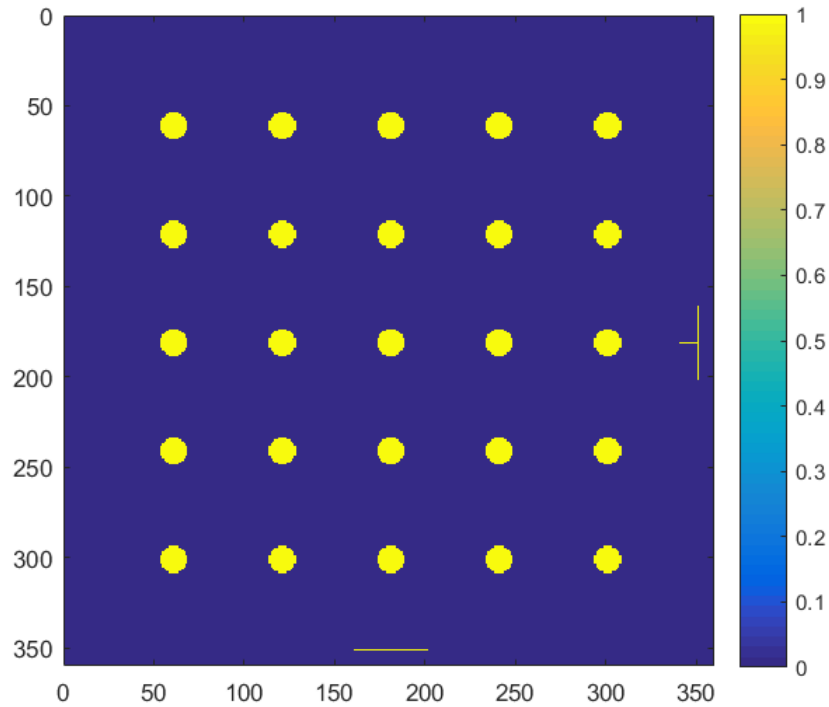
Figure 2.9: The array representing the calibration plate visualized as an image. The 'T' and the line observed at the bottom and the right of the image marks clarify the positive global $X-$ and $Y-$ direction respectively to guide when doing the calibration procedure later.

ner like when creating images of the phantom object. Some examples of the resulting artificial calibration images are illustrated by figure 2.10. This was done for all cameras for the calibration plate located at two $Z-$positions.

2.1.6   Calibration procedure

2.1.6.1   Calculating mapping function

The calculation of the mapping function was done using the same MATLAB-program used by Worth and Dawson (2013c). To do this, the spatial position of the calibration points in the images must be specified. Further, the position of the points in the images have to be found. User input is needed to locate the origin of the dot pattern, and a neighbouring dot in each direction

(a) $\theta = -70°$ (b) $\theta = 0$ (c) $\theta = +70°$
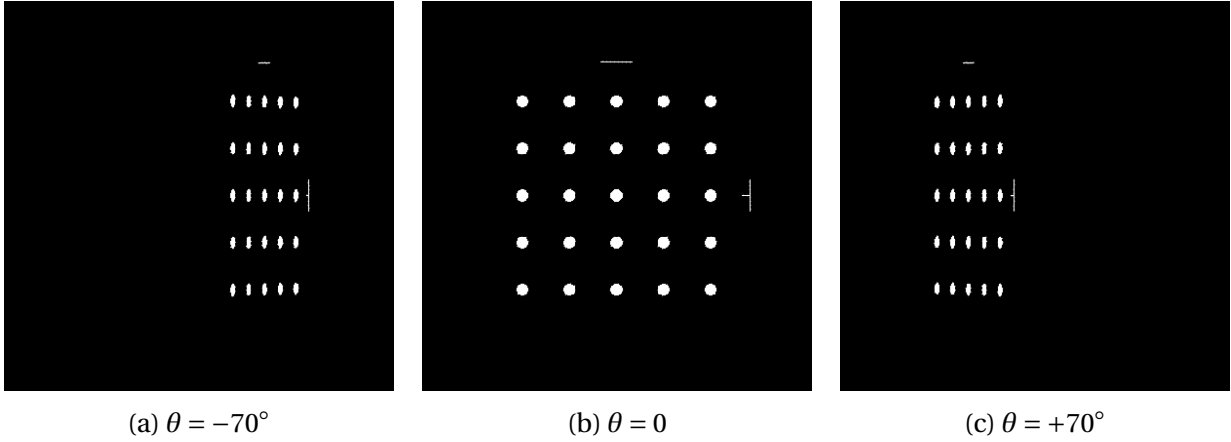
Figure 2.10: Images of the calibration plate from different angles, where θ is the angle between the camera and normal axis of the plate. Here, the position of the center dot is $[0,0,6]$mm

of the pattern to help the dot searching algorithm. Each dot position is found, giving it sub-pixel coordinates in the image coordinate system. Then, coefficients for polynomials based on Taylor expansion of an order specified by the user is found using MATLAB's built-in robust multilinear regression function (MathWorks). These polynomials are the mapping function relating image coordinates to 3D space. For the synthetic experiments, third order polynomials were used. These are on the form:

$$X_i = \beta_{0i} + \beta_{1i}x + \beta_{2i}y + \frac{1}{2!}\beta_{3i}x^2 + \frac{2}{2!}\beta_{4i}xy + \frac{1}{2!}\beta_{5i}y^2 + \frac{1}{3!}\beta_{6i}x^3 + \frac{3}{3!}\beta_{7i}x^2y + \frac{3}{3!}\beta_{8i}xy^2 + \frac{1}{3!}\beta_{9i}y^3$$

(2.3)

where X_i is the spatial coordinate, and β_{ji} the coefficient belonging to the ith spatial coordinate. x and y are the image coordinates. With these polynomials, each pixel was related to two spatial positions, one at each plane where the calibration plate was placed. A straight line between these two points was drawn for each pixel, giving it the pixel's LOS. This is illustrated in figure 2.11. If the planes lies within the volume, the lines were extrapolated until they leaves the boundaries of the volume. The polynomial model is considered to have advantages over the pinhole model when unknown aberrations in the optical path is present (Scarano, 2013).
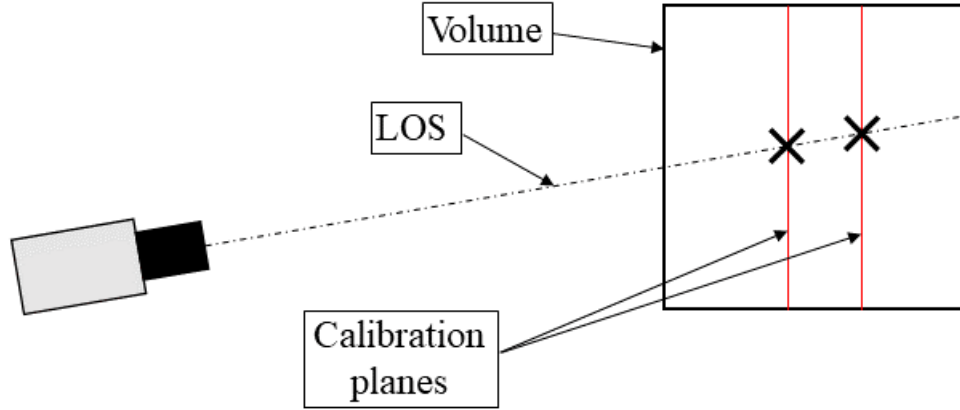
Figure 2.11: Illustration of how the LOSs are estimated based on calibrations in two planes. The red lines marks position of the calibration planes, and the crosses where the pixel is related to those two planes.

2.1.7 Reconstruct phantom object

2.1.7.1 The problem to be solved

The phantom object was to be reconstructed based on the generated images. A voxel volume equal to the one described in section 2.1.3 was created. An approach commonly used in Tomographic PIV is to discretize the volume into a 3D-array of spherical voxel elements with 3D-coordinates (X, Y, Z), and light intensity $E(X, Y, Z)$ (Atkinson and Soria, 2009). It was assumed that back-projecting the 3D light intensity distribution into the cameras results in the experimental images. Elsinga et al. (2006) expressed this as a set of linear equations:

$$\sum_{j \in N_i} w_{i,j} E(X_j, Y_j, Z_j) = I(x_i, y_i) \tag{2.4}$$

where (x_i, y_i) is the ith pixels position, and $I(x_i, y_i)$ is the intensity of this pixel. N_i represents the voxels contributing to the intensity of $I(x_i, y_i)$. $w_{i,j}$ is the weighting coefficient that describes the contribution of jth voxel intensity to the ith pixel intensity (Elsinga et al., 2006). The weighting coefficients are estimated, and knowing the pixel intensities makes this an inverse problem.

2.1.7.2   Weighting

As explained in section 2.1.6, each pixel's LOS was estimated by calibrating a camera model. The LOSs beams through the volume, intersecting with the voxels. How the pixel's LOS intersect with each voxel, determine the weighting coefficient for the specific voxel related to the relevant pixel.

If it is assumed that the voxels are spherical, and the pixels are cylinders, the weighting coefficients relating voxels and pixels becomes independent of orientation (Atkinson and Soria, 2009). This make the calculation of the weighting coefficients used in equation 2.4 much less complicated. The value of the weighting coefficient is based on the distance between the line-of-sight(LOS) and voxels. How the pixels and voxels are related by the weighting function is illustrated in figure 2.12.
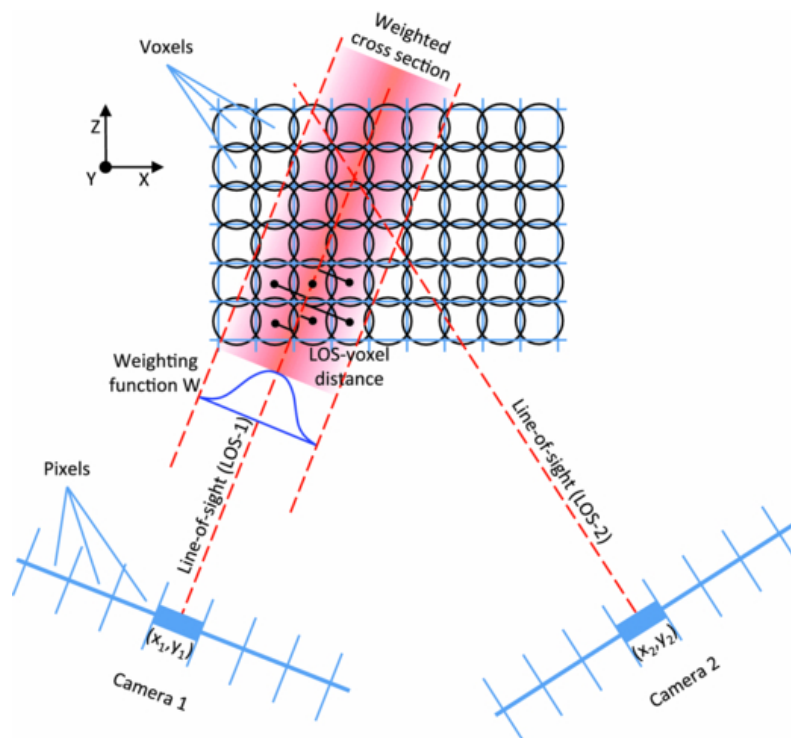
Figure 2.12: A volume discretized into spherical voxels viewed by two cameras. Voxels falling inside the weighted area of a pixel gets a non-zero weighting coefficient, $w_{i,j}$, for the relevant pixel.(Reproduced from Scarano (2013))

2.1.7.3 MFG

An initial intensity distribution guess is needed to perform a MART reconstruction. A common approach is to use an uniform first guess. Another option is the use the Multiplicative First Guess (MFG) developed by Worth and Nickels (2008) for Tomographic PIV. One of the advantages with the MFG, with regard to tomographic PIV, is that large regions of the intensity volume is found to be zero. This accelerates the reconstruction due to zero intensity regions does not have to be updated during MART iterations. In CTC, most of the volume will have an intensity value, but the MFG also gives a more accurate first guess than an uniform one. It is generally considered that a better first guess for iterative algorithms will help convergence of the solution, deeming the MFG useful for CTC too. The MFG method was implemented in the reconstruction program and used.

Using the pixel intensities and the calculated weighting coefficients, a series of intensity lines were created by projecting the pixel intensity for an image through the volume. Such an intensity volume was made for each image. The estimation of an intensity volume for a single camera can be expressed as,

$$E_c(X_j, Y_j, Z_j) = \sum_{i \in N_j} w_{i,j} I_c(x_i, y_i) \tag{2.5}$$

where $E_c(X_j, Y_j, Z_j)$ is the volume intensity at position (X_j, Y_j, Z_j) for camera c. N_j indicates the pixels affecting with voxel j. $I_c(x_i, y_i)$ is the pixel ith intensity of camera, c.

By multiplying the voxel values at the same position in respective volumes created for each image, only voxels in regions where intensity lines intersect will have a non-zero value. At last, the remaining intensity field is normalized based on the number of camera views. Multiplication of the volumes and the normalization can be expressed as:

$$E_0(X_j, Y_j, Z_j) = \left(\prod_{c=1}^{N_c} E_c(X_j, Y_j, Z_j) \right)^{1/N_c} \tag{2.6}$$

This is done for all voxel positions (X_j, Y_j, Z_j) resulting in the initial intensity guess $E_0(X_j, Y_j, Z_j)$.

2.1.7.4 MART

The iterative reconstruction algorithm implemented and used for this study were the multiplicative algebraic reconstruction technique (MART) (Herman and Lent, 1976). This technique has been widely applied in Tomographic PIV studies (Elsinga et al. (2006), Scarano (2013)). For Computed Tomography of Chemiluminescence (CTC), the algebraic reconstruction technique (ART) (Gordon et al., 1970) have been a frequently used method (Floyd et al., 2011), but the MART have also been utilized (Worth and Dawson, 2013c) and proven capable for CTC.

A single iteration of the MART procedure was described by Elsinga et al. (2006) as:

1. for each pixel in each camera ith;

    2. for each non-zero voxel jth;

$$E_{n+1}(X_j, Y_j, Z_j) = E_n(X_j, Y_j, Z_j) \left(\frac{I(x_i, y_i)}{\sum_{j \in N_i} w_{i,j} E_n(X_j, Y_j, Z_j)} \right)^{\mu w_{i,j}} \tag{2.7}$$

    end loop 2

end loop 1

where n indicates the number of iteration, and μ is a relaxation factor that must be ≤ 1 for the MART algorithm. For each iteration, $E(X_j, Y_j, Z_j)$ is updated. $E_0(X_j, Y_j, Z_j)$ would be the initial guess, either a uniform value, or an initial guess like the MFG presented earlier. Another requirement for the MART algorithm is that both E and I are strictly positive. The presented procedure is repeated for the desired number of iterations.

2.1.8 Assess reconstruction quality

To evaluate reconstruction quality, the parameter Q is used. This is the normalized correlation coefficient of the exact (generated) and reconstructed light intensity distribution (Elsinga et al., 2006). It is defined as,

$$Q = \frac{\sum_{X,Y,Z} E_r(X, Y, Z) \cdot E_g(X, Y, Z)}{\sqrt{\sum_{X,Y,Z} E_r^2(X, Y, Z) \cdot \sum_{X,Y,Z} E_g^2(X, Y, Z)}} \tag{2.8}$$

where E_g is the generated light intensity distribution created in 2.1.3, while E_r is the reconstructed one. This reconstruction quality parameter can only be used when E_g is known, in other words, in synthetic experiments like those performed in this thesis.

The quality of the reconstructions were also evaluated by investigating cross sections of the reconstructed object and compare them to the phantom object.

2.1.8.1 Numerical cost

The predicted numerical cost of the different procedures is presented in table 2.2.

Table 2.2: Operations performed for different algorithms

Procedure	Operations
MFG	$N_{vox}(8N_c + 1)$
MART	$4nN_cN_{vox}(8\overline{L} + 4)$

N_{vox} is the total number of voxels, and it is assumed that all voxels are non-zero for all iterations, n. N_c is the number of camera views used, as defined earlier. L is the LOS through the volume measured in voxels, and $\overline{L}$ is the average length of the LOS' through non-zero voxel volume. For both estimates it is assumed that the pixel-to-voxel ratio is 1. Further is it assumed that a voxel receives 4 intensity contributions from each images. These assumptions are the same as done in cost estimates done by Worth and Nickels (2008) and Atkinson and Soria (2009), regarding reconstruction done for Tomographic PIV. However, an important difference is that for estimates done here, all voxels are assumed non-zero for all iterations.

2.1.9 Case parameters

For all the synthetic reconstructions performed, the parameters presented in table 2.3 have been used, unless otherwise is stated. For the pinhole models, the parameters in table 2.1 have been used. The parameters are set such that the pixel-to-voxel ratio is close to 1. This is done because the pixel resolution of the images is the resolution of the projected information, and having a finer voxel discretization is not considered to give any better 3D information resolution.

Table 2.3: Case parameters

Domain	$12 \times 14 \times 12 mm^3$ (centered in the origin)
Discretisation	8 voxels/mm
Camera distance	$1000 mm$ from global origin
Initial guess	MFG
MART iterations	$n = 5$
Relaxation factor	$\mu = 1.0$

Chapter 3

Phantom Study - Results and Discussion

This chapter will present the results from a parametric study performed in order to try to optimize the experimental setup, and identify possible problems with the methodology of the implemented CTC program.

3.1 Parametric study

The parametric study will first investigate how setup of the camera configuration will affect reconstruction quality. Further will reconstructions performed with the two different implemented camera calibration models be compared. The influence of reflections in the images will then be investigated. Finally, the impact of calibration errors on the reconstruction quality will be evaluated. For all tests, except the calibration model comparison, the generated pinhole models were used as the camera model relating images to 3D space.

3.1.1 Number of camera views and viewing width

How the number of views utilized, and the angle between the outer views affects the reconstruction quality have been investigated. The cameras was set up in an arc configuration as illustrated in figure 2.2, where angle width, β, is varied from 60° to 140° at 10° intervals. The number of views, N_c, is varied from 3 to 19 with equal angle between views. Because of all the different camera positions, the generated pinhole models were used to relate the images to the 3D voxel space, thus eliminating the need for the user to calibrate each camera for each setup.

Using the pinhole models with known parameters implies that the mapping functions relating 2D and 3D space are perfectly calibrated, eliminating the influence of calibration errors for this test.
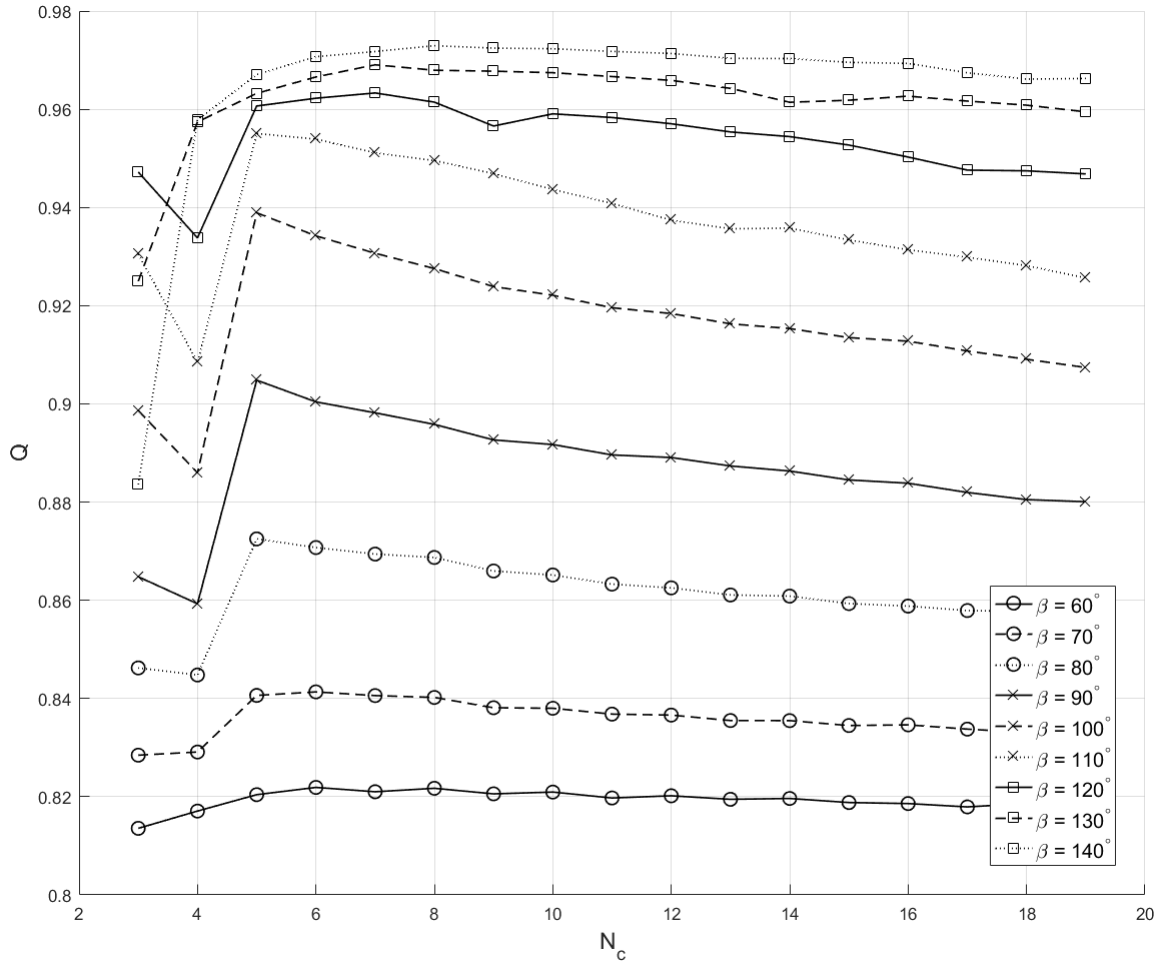
Figure 3.1: The reconstruction quality, Q, plotted against number of camera views, N_c, utilized for different arc widths, β

Results from the reconstruction tests are presented in figure 3.1. Based on the reconstruction quality indicator, Q, the results indicate that the total viewing width, β is influencing the reconstructions more than the number of views. Q increases with increasing β, and for the widest views, Q-values approaches close to 1, indicating an almost perfect reconstruction. By intuition, it is expected that the reconstruction quality will increase with a larger viewing width, due to the expectation that wider views will give more varied information about the object being imaged. Two views with 180° between them will give the same information about the object,

implicating that a β approaching 180° will give a Q value approaching a maximum for the utilized computed tomography method and experimental setup, if enough views are utilized. This is further illustrated by the figure 3.2 where number of views is kept constant at 15, while β is varied.
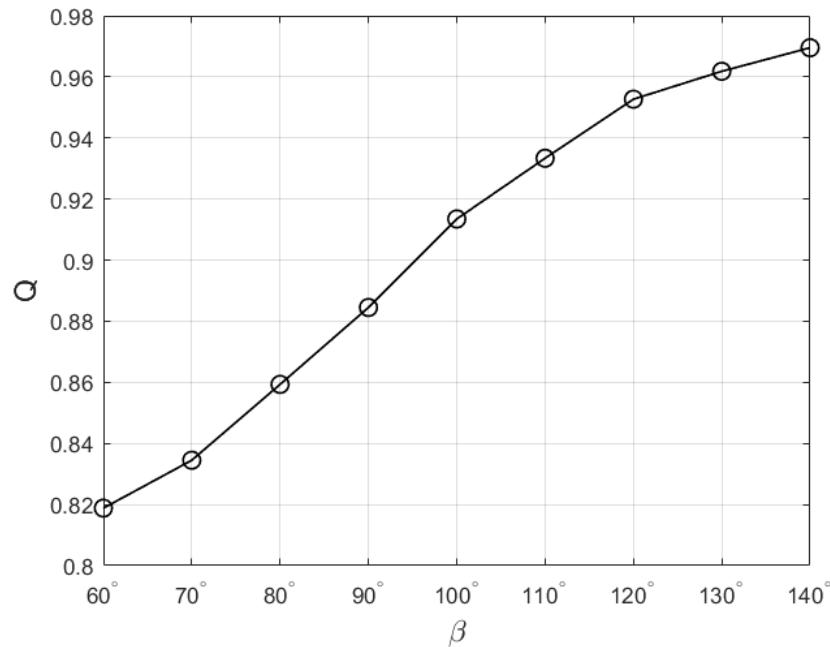
Figure 3.2: The reconstruction quality, Q, plotted against different arc widths, β, for $N_c = 15$.

As explained earlier, the parametric study uses a heavily idealized setup and this test does not imply that the reconstructions performed using data from a real experimental setup will have the same kind of quality. However, based on this test, the experimental setup width should aim to be as wide as possible.

Each β setup seems to reach a maximum Q value for 5-8 views, the widest β values seems to stabilize around this value and be constant with increasing number of camera views, while the lower β values have a trend where reconstruction quality decreases for increasing number of views. As noted before, a wider width, β, will give more information about the reconstructed object, and with a narrow width, it is suspected that the information is biased. Increasing the number of views for the narrow width, β, will give little new information, but reinforce the already biased information, making the reconstructions even more biased. This suggests that for a narrow view width, increasing the number of views not necessarily improves the reconstruction

quality.

Another interesting, but less important feature of the variation of number of views, is the inconsistency of how Q varies for the different β for $N_c = 3 - 5$. Although these observations are not directly relevant to reconstructions that will be performed later in this thesis, trying to understand some characteristics of the reconstruction method could be useful.

For the largest β values, the Q values consistently increase with increasing N_c, while for the other β-values, Q drops for $N_c = 4$, then increases again. The author has no good explanation for the drop in accuracy for $N_c = 4$. It is possible that it is due to some favorable positioning of views for the reconstruction technique. For $N_c = 3$ and all other odd number of views, one of the camera's viewing direction is normal to the global XY-plane, if this play a role in reconstruction quality, the role could be significant for few views, and minor when number of views are increased, thus not be observable for reconstructions performed with larger number of even views. If this is true, an explanation for why this effect does not become apparent for the largest βs should be given.

It is possible that this is not observed because the reconstructions performed with large β-values where $N_c = 3$ is even more problematic. If one considers a setup with $\beta = 180°$ and $N_c = 3$, two of the views would be opposite of each other. Earlier it was stated that two such views provides the same information, making such a setup in practise a two view setup where one of the views is given twice the significance to the reconstruction. If the same kind of error expected to show up in such a setup, also affects setups with β-values close to $180°$, that could explain why the drop for $N_c = 4$ is not observed for the largest β-values. Another result supporting this explanation is that the best reconstruction for $N_c = 3$ is performed for $\beta = 120°$, which would most evenly distribute the views over a span of $180°$, thus be expected to minimize this error. However, for higher numbers of N_c which will be used in the real experiment, these discussed characteristics are not observed.

To investigated the suspected bias of the narrow view width, reconstruction objects from different setups will be visually inspected. Two βs of $100°$ and $140°$, with 5 and 15 views, giving a total of 4 different setups, will be reconstructed and inspected. The reconstruction quality of the setups can be found in table 3.1. XZ-slices at $Y = 0$ of the reconstructed objects are illustrated in figure 3.3, the original slice at this position of the phantom object is found in figure 2.7f.

(a) $N_c = 5$, $\beta = 100°$

(b) $N_c = 15$, $\beta = 100°$

(c) $N_c = 5$, $\beta = 140°$

(d) $N_c = 15$, $\beta = 140°$
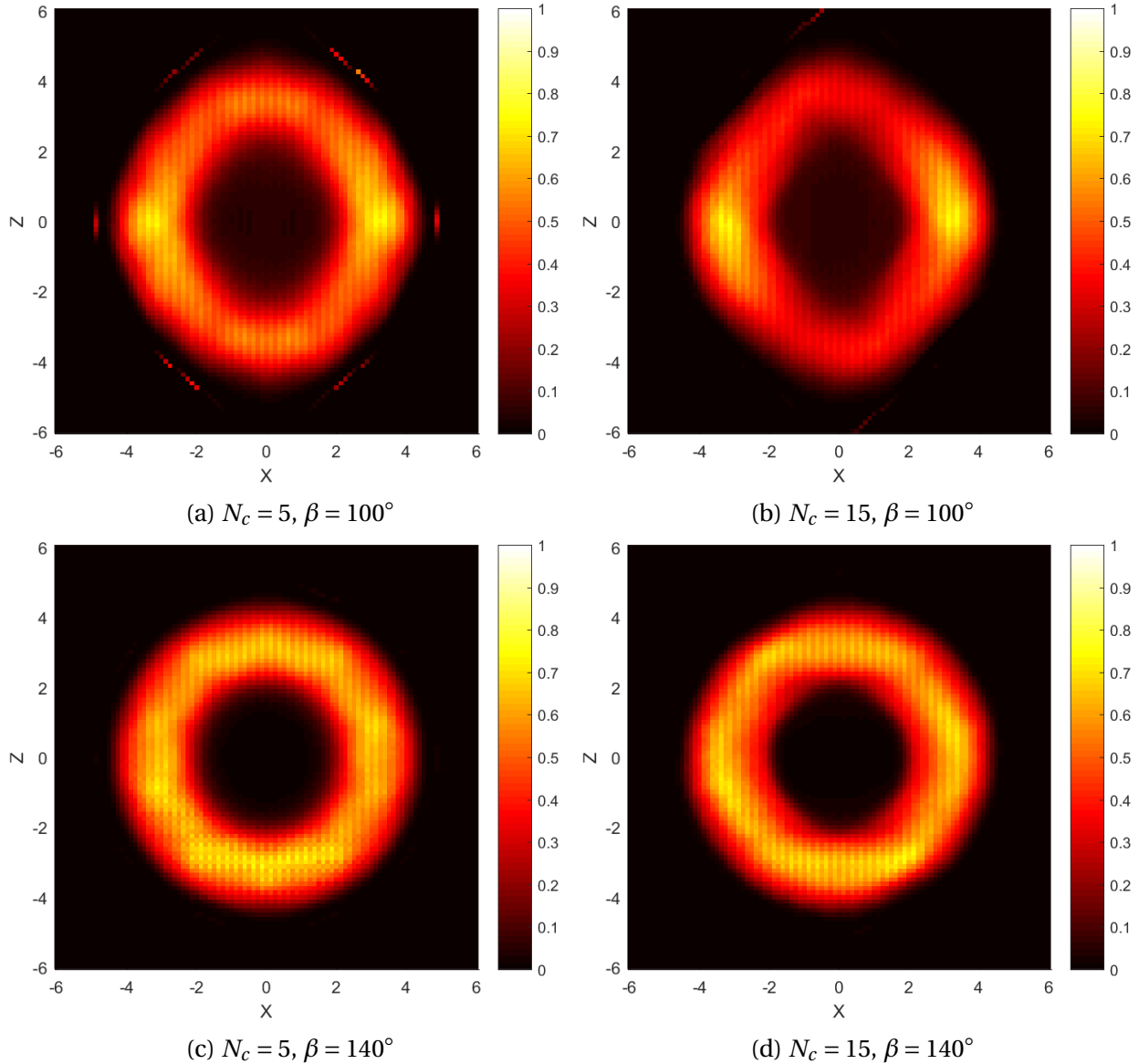
Figure 3.3: XZ-slices at $Y = 0$ for different reconstruction setups.

If one compares the two slices in figure 3.3a and 3.3b, it can be observed that the reconstruction performed with a lower number of views appear to have a higher degree of axisymmetry compared to the other. Both slices appear to have two high intensity zones located at approximately $[X, Z] = [\pm 3, 0]$, but these zones are more intense compared to the rest of the object, for the reconstruction performed with a higher number of cameras. This supports the suspicions that biased information gained from narrow views is amplified with increasing camera views. For the $\beta = 140°$ reconstructions this is not observed, and both reconstructions appear to perform relatively well.

For the setup were $\beta = 100°$ and $N_c = 5$, there appear to be some reconstruction artifacts located a small distance away from the intensity zone. Such artifacts are not present in either figure 3.3b or 3.3c, suggesting that increasing both the view width β and camera views N_c can reduce reconstruction artifacts.

3.1.2 Polynomial camera model

For the final experiment, a polynomial camera model will be used to relate images to the 3D space. To check how using the polynomial model instead of the "perfect" pinhole model affects reconstructions, several reconstructions from different setups are compared. Setups with $\beta = 100°, 120°, 140°$ and $N_c = 5, 15$, are performed, and reconstruction qualities are compared to the results when using the pinhole model. Polynomial models of order 3 is used, and they are calibrated using the described procedures in 2.1.6. Calibration errors when using the polynomial models varied with camera positions, where the outer views had highest errors. The outer views had a mean error of approximately 0.047 pixels, while the mean error of the view normal to the calibration plane was around 0.010 pixels. Results are compared in table 3.1.

Table 3.1: Comparison, pinhole and polynomial calibration model

View width, β	Number of cameras, N_c	Q, polynomial	Q, pinhole
100°	5	0.935	0.939
100°	15	0.917	0.914
120°	5	0.962	0.961
120°	15	0.956	0.953
140°	5	0.945	0.967
140°	15	0.957	0.970

Based on these result, there are no apparent differences between using the two models in regard to reconstruction quality parameter Q. This indicates that both models are able to perform sufficently accurate mapping between image coordinates and 3D space, as long as the calibrations are accurate. If one compares the calibration errors present here to results from the calibration error test performed later in the parametric study, it is indicated that errors of the same order as observed here are too small to seriously affect the overall reconstruction quality.

3.1.3 Reflection

Investigation of how reflections will influence the reconstruction quality was performed. This was done because it was suspected that the final CTC experiment could be prone to such reflections. A setup with $\beta = 140°$ and $N_c = 5$ was used. To simulate reflections, a strip of intensity was added to one of the cameras. The size of the strip was set to be 50×100 pixels large, and given a uniform intensity. The total intensity of the strip was set as a percentage of the total intensity of the original image it was added to. The reconstruction was tested for a range of percentages. The MART algorithm iterates over the camera views sequentially, and the camera experiencing reflection was varied to investigated if this also could affect the reconstructions.

The artifact intensity was varied for 0% to 50%, and added to three different images in three different tests. An example of the artifact images are shown in figure 3.4 The camera positions where artifacts was added were $\theta = -70°, 0°, 70°$, which is the 1st, 8th and 15th processed image in the iteration sequence respectively. The results are presented in figure 3.5.

(a) Image with no reflection artifacts

(b) Image with a reflection artifact with 25% intensity
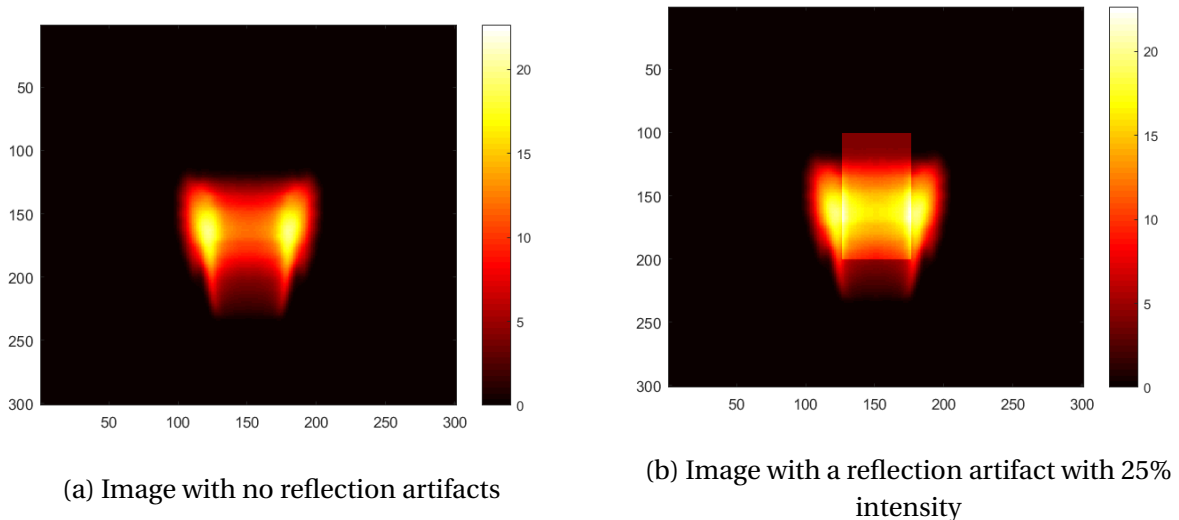
Figure 3.4

From the test, it can be observed that a reflection artifact present in the 1st and 8th image have small influence on the final reconstruction quality for all intensity percentages, while artifacts in the 15th view, has a significant effect for higher intensity percentages. A possible explanation is that in the two first cases views processed after the view with the artifact corrects the reconstruction, while in the last case it is the final view that is problematic and no correction
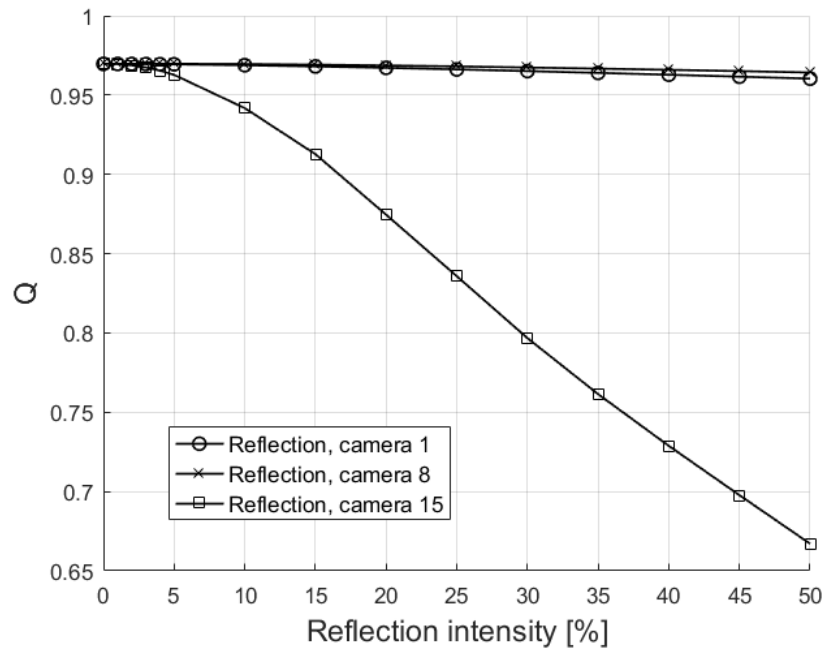
Figure 3.5: The reconstruction quality, *Q*, plotted against intensity percentage of the added reflection artifact.

is performed due to it being last in the iteration sequence of the MART reconstruction. It was expected that a problematic last view would degrade the reconstruction quality in a large degree. However, it was not expected that the other two cases would have close to no degradation of quality, even for artifacts with higher intensity. This indicates that reflection artifacts may be tolerable if only a few of the views have them, and that the views containing them are not processed last in the MART algorithm.

To map how the reflection artifact problem develops with respect to which view is affected, the test was redone where the 8th to 15th view were given artifacts, one view at the time. Like before the artifact's intensity percentage was varied. The results from the new test are presented by figure 3.6. It can be observed that reflections artifacts added to camera number 10 and lower numbers influence the reconstructions in a small degree based on *Q*. For the other views, *Q* consistently decrease with both the reflection intensity, and with camera number where reflection artifacts where added. Intuitively, this is as expected, due to gain in reflection intensity deteriorate the data from the affected view more. It is also expected that if the data where errors are introduced is processed later in the MART iteration sequence, the errors in the final

reconstructed object will be larger.

Other parameters of the setup may play important roles in reflection degeneration. It could be interesting to investigate what the important parameters to achieve good reconstructions, despite reflections appearing in views processed early in the iteration sequence are. Further testing could investigate if it is the number of camera views processed after the view with introduced errors that matters, or if it is the angle between the erroneous, and last iterated view. However, due to time limitations this was not done.
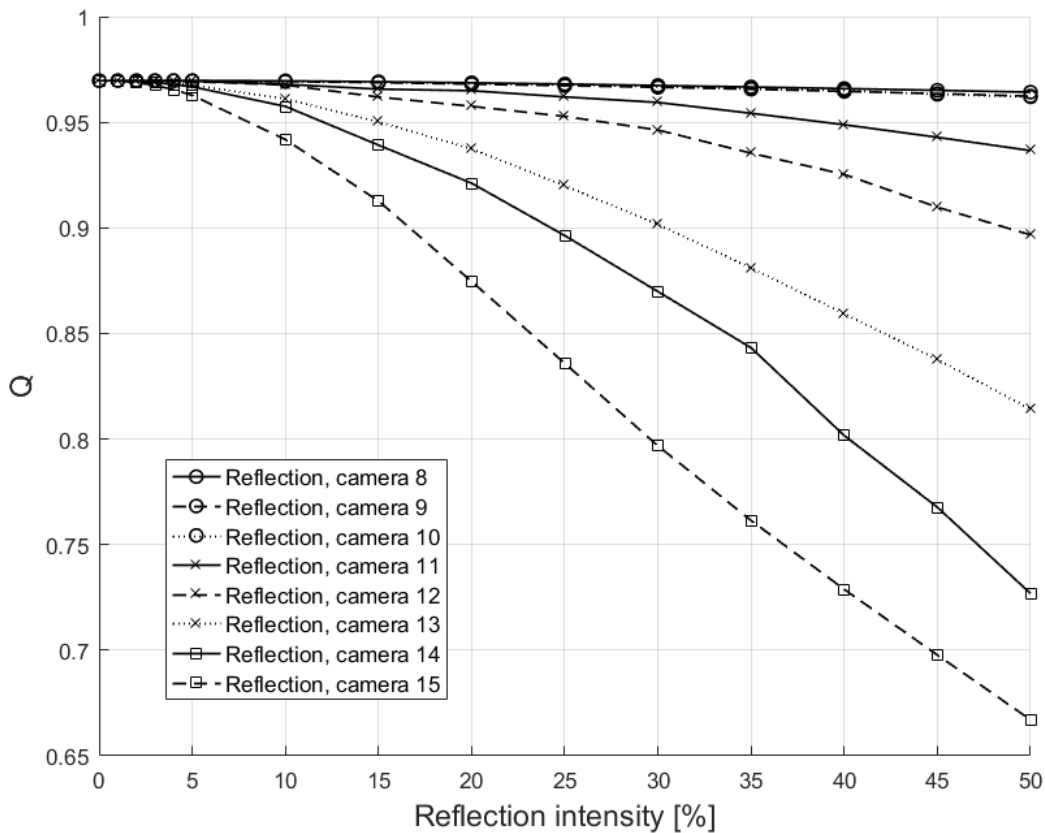
Figure 3.6: Results for the new reflection test. Artifacts where added to the 8th to 15th image.

3.1.4 Calibration error

Another possible problem that may harm the reconstruction quality are calibration errors. A setup with $\beta = 140°$ and $N_c = 5$ was also used for this test. To test how calibration errors affect the reconstructions a similar approach like the reflection test will be taken. Errors will first be

introduced to a single camera, and reconstructions with different error values will be tested. There was applied an error to the 1st, 4th, 8th, 13th, 14th and 15th view one at the time. The errors were applied by shifting the image from the camera with calibration errors different number of pixels in a direction, implicating a uniform global calibration error. Results from the test are illustrated in figure 3.7.
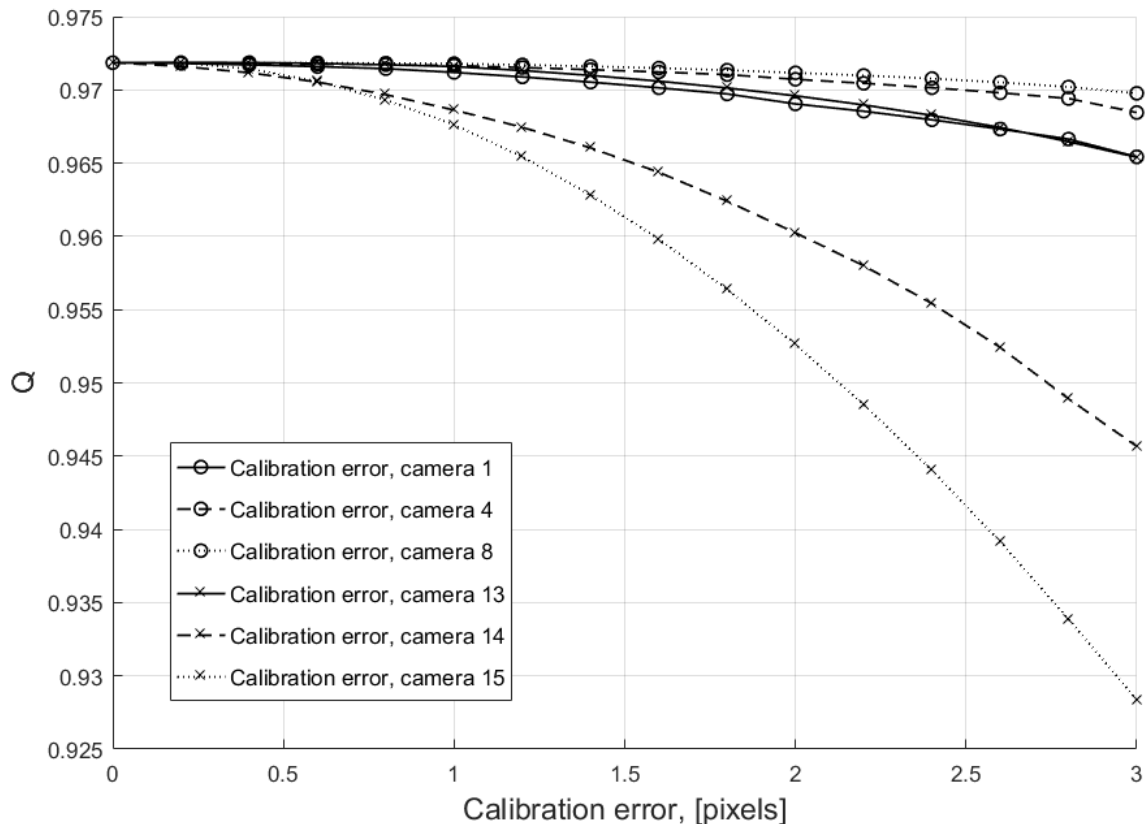
Figure 3.7: Reconstruction performance when a varied calibration error is applied to different cameras.

As for the reflection test, it is observed Q depends on which of the cameras the error is applied to. Applying an error to the 14th and 15th camera deteriorates the reconstruction quality most, which is what one would expect based on the reflection test results. However, the degradation of reconstruction quality is not consistent with the camera number like the reflection test. The least degraded reconstructions are seen when the error is present in the 8th camera view. It is suspected that the reason for this is that also the position of the erroneous camera with regard to discretization directions of the voxel volume may affect the reconstructions. The

8th view's LOSs are almost parallel to the Z-axis, and this may be the reason for this.

To check this dependency, another test was performed, where the iteration sequence was altered. Camera numbering follows the convention illustrated in figure 2.2, and the processing sequence of the views follow the same numbering. The position of the 8th and 15th view in the iteration sequence was switched, and an error was applied to the two views, one at the time. The results was then compared to the results from the reconstructions where the iteration sequence was unaltered. Reconstruction performances are presented in figure 3.8.
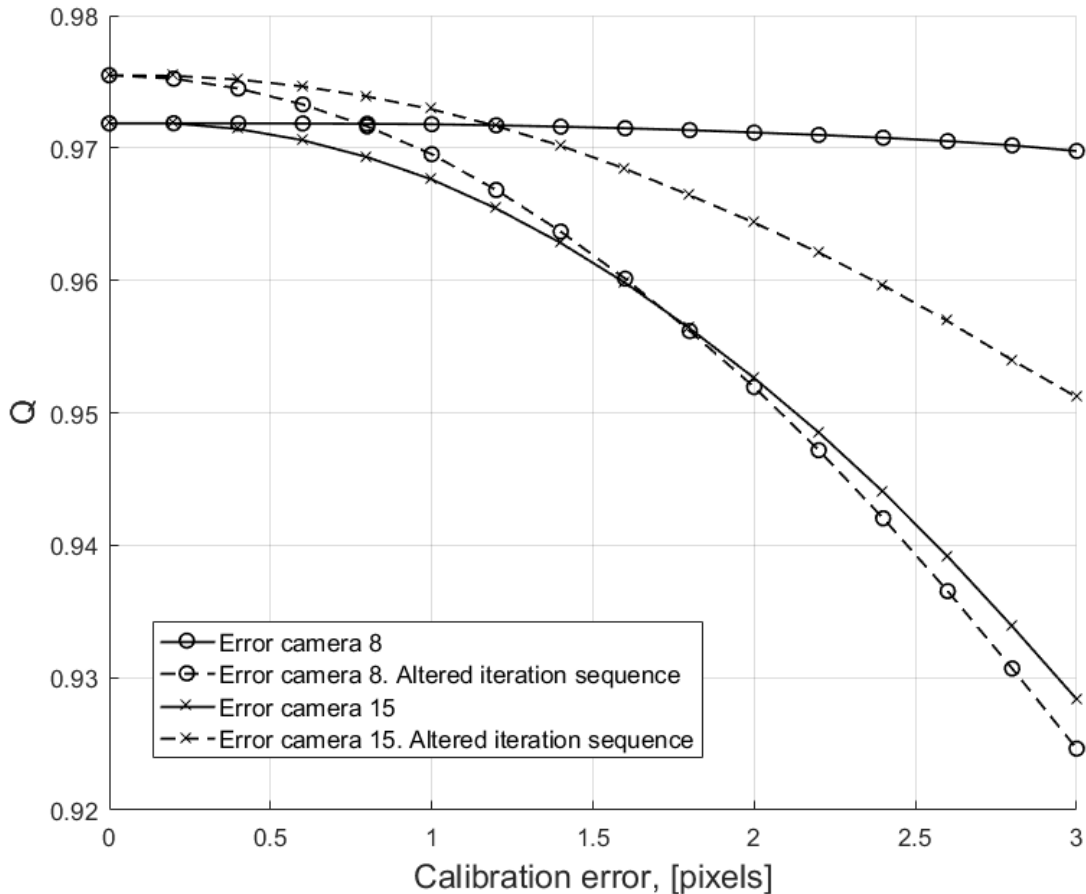
Figure 3.8: Reconstruction performance when a varied calibration error is applied to two different cameras, and the iteration sequence is altered

Some interesting features of the reconstructions appear in the results. It is observed that changing the iteration sequence gives a slight increase in Q for the reconstructions with low calibration errors, indicating that iteration sequence in general may have an influence on the overall reconstruction quality. Although tests investigating this could be interesting, but they were not performed due to time limitations.

As for the dependency of the iteration sequence for the view where calibration errors were introduced, we see that when the 8th view is erroneous, and processed last, it has a similar behaviour as the reconstruction performances were the 15th is erroneous and processed last. This result indicate a clear coherence between when an erroneous view is processed and the final reconstruction quality, something which was also observed in the reflection test.

At last, some indication of the suspected coherence between viewing direction of the erroneous view with regard to discretization direction, and reconstruction quality is observed. When the calibration error is introduced to the 15th view, but processed 8th in the processing sequence, the reconstruction quality drops faster then when the processing sequence is unaltered and the 8th view is erroneous. This could be investigated further to see if there are certain angles where this error is maximized, but it was not done due to time limitations.

3.2 Experimental recommendations

Based on the parametric study, some recommendations about the experimental methods were given. First, for the setup it was recommended to try to maximize the viewing width β. Also, it was indications of that when the number of camera views were sufficient, adding more views would not result in better reconstructions, but only increase processing time. Thus, for the experimental setup, a view width $\beta = 140°$ and view number, $N_c = 15$ was recommended.

From the parametric tests it is also indicated that if some of the views are suspected to be prone to reflections, it may be advantageous to alter the iteration sequence such that the views that are suspected to be prone to error are not processed last. The same recommendations about altering the processing sequence of the views holds for calibration errors.

All the parametric test performed are under significant idealizations as described in chapter 2. The phantom object used in the parametric investigation was axisymmetric. Further testing should investigate quality of reconstructions of asymmetric phantoms in order to check how well the tomographic methods implemented are able to capture asymmetries.

Other problems that may appear in the experimental setup, but was not suitable to test in the phantom study were investigated using a mock experiment. The setup of this experiment and results from it are presented in section 4.1 and 5.1-5.2, respectively.

Chapter 4

Experimental Methods

In this chapter, the experimental methods used will be presented. To investigate possible problems with the experimental setup of the annular combustion chamber, a mock setup was used. The setup itself, and problems investigated will be discussed first in this chapter.

Later, the experimental method of the final experiment were CTC is applied to a flame confined in an annular combustion chamber will be presented.

4.1   Mock experiments

Some problems that may appear in the experimental setup are not suited to test for in the parametric phantom study. Problems like re-positioning of the calibration plate and refraction from the curved glass were investigated utilizing a mock setup.

4.1.1   Experimental setup

The mock setup used for this investigation consisted of one of the base plates from the annular combustion chamber and the same curved quartz glass that was used to enclose the combustion chamber. To investigate potential problems, an imaging system consisting of a Imager LX 16M camera from LaVision with a Sigma 105mm f/2.8 EX DG Macro Lens was used. The software Bobcat GEV is used to control the camera and acquire images. The camera was placed approximately 800 mm away from the center of the investigated burner of the plate. Resolution of the camera was 4864 × 3280 pixels, but only parts of the captured images was used. Spatial

resolution of the images was approximately 24 pixels/mm. When capturing images from wide angles, the camera was stationary, but the base plate was rotated around the center of the investigated burner. The setup is illustrated in figure 4.1.
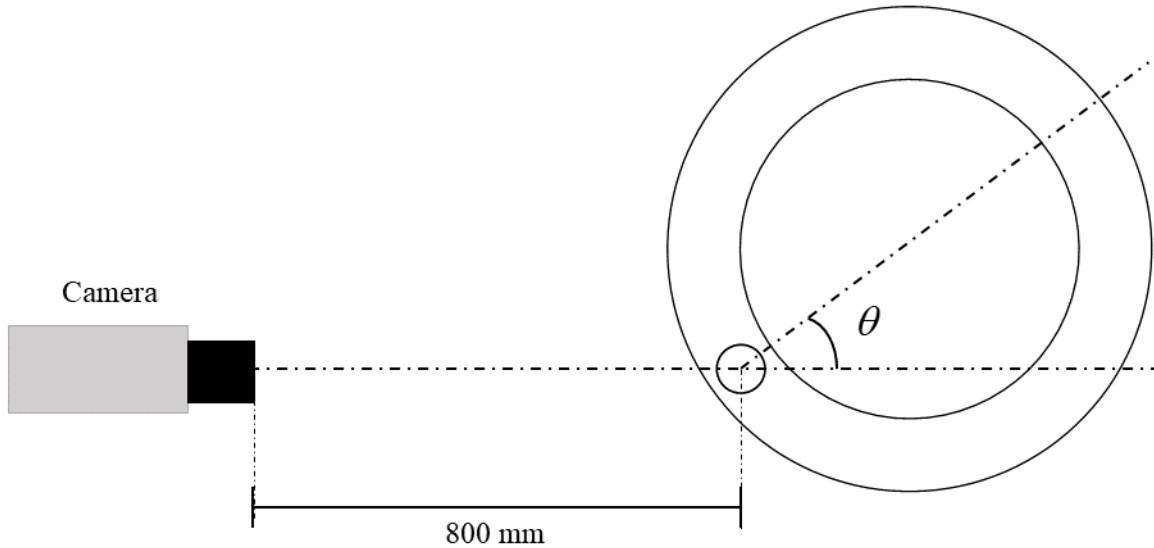
Figure 4.1: The mock setup from above. The camera was placed approximately $800mm$ away from the investigated burner position. θ is the angle of rotation of the base plate.

4.1.2 Re-positioning

To be able to re-position the calibration plate at the same place in the combustion chamber for each view, a device was design and produced. The device consists of a base plate where the calibration plate was mounted. Two positioning tubes was also mounted to the plate. The device is illustrated in figure 4.2. Outer and inner radius of the base plate were set such that the plate was easily placed between the outer and inner enclosure of the annular combustion chamber. The holes in the base plate were placed in the same pattern as the burners in chamber, and the dimension set to give good clearance for the tubes. A groove and a hole for fastening the calibration plate in the investigated burner position was also machined. The plate was originally designed to fit a $58mm \times 58mm \times 6mm$ dual plane calibration plate, but it is also possible to mount a larger plate to the device as seen in figure 4.2b.

(a) Concept of the repositioning device

(b) Device with a large calibration plate mounted

(c) Positioning tubes
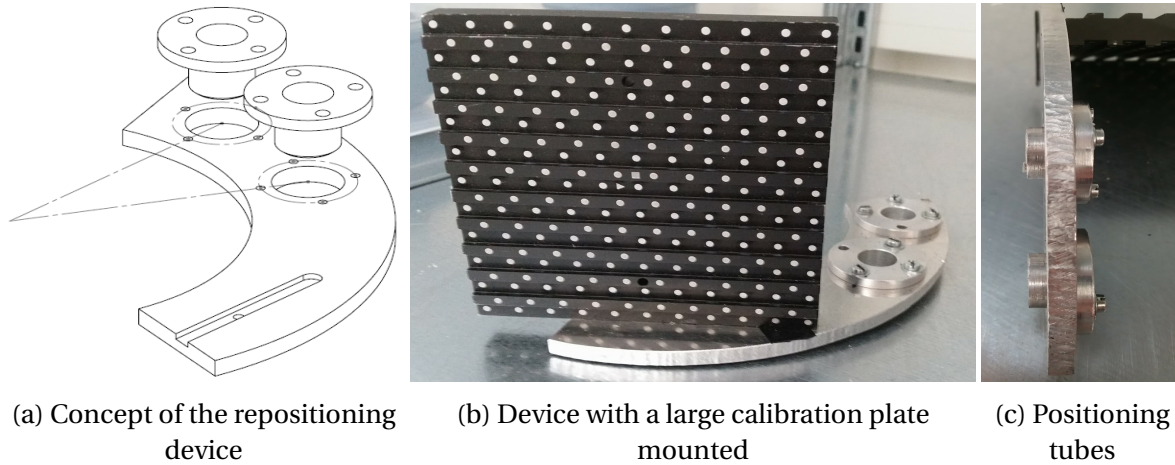
Figure 4.2: Different images showing the repositioning device

The base plate was positioned at the desired place, and the positioning tubes were slipped through the plate and fitted into the burners underneath. M3-bolts were used to fasten the flange of the tubes to the base plate, and the tubes would ensure that the base plate was positioned in the same place.

To test how accurate the re-positioning was, the plate was positioned in the mock setup 50 times and imaged each time. θ was set to 0, meaning the camera was positioned normal to the plate. For this test, the quartz glass was removed in order remove the influences from refraction, and only test the re-positioning. A dual plane calibration plate with 12×12 and 11×11 dot pattern was used for this test. The spacing of the dots are 5 mm in both directions. Results from this test are presented in section 5.1.

4.1.3 Refraction

Refractive effects can influence the experiments in several possible ways, and some of the problems will be discussed here.

The first apparent problem that may arise due to refraction is caused by the curved quartz enclosure. Because of the difference in refractive indexes of air and quartz, pixel's LOS that encounter the quartz enclosure from an angle not normal to the enclosure surfaces will refract, meaning the path of light is bent. For the enclosure, this will happen two times, both when light enters and exits the enclosure. A common way of dealing with this problem in other optical

methods like PIV is to match the refractive index of the enclosure and the working fluid, so-called refractive index matching (Im et al. (2014), Häfeli et al. (2014)). However, this was not a possibility for the planned experiments performed in this thesis.

To deal with this, it was assumed that the path of a pixel's LOS will not bend, once it was inside of the enclosure. By placing the calibration plate inside the quartz enclosure, the calibration procedure will determine the pixel's LOS inside of the enclosure, which was the volume of interest. Assuming straight LOSs inside the combustion chamber was considered an accurate assumption during acquisition of calibration images. However, during operation of the combustion chamber, varying density of gases inside of the chamber can cause optical inhomogeneities that could affect the path of light through the chamber. This phenomena is well known, and is the basis for Schlieren photography methods. Even though it is a well known phenomena, it is seldom mentioned in CTC-studies, and the effects of Schlieren will be assumed negligible, and not investigated further.

Another problem addressed, but not further investigated is the fact that the refractive index is dependent on the light wavelength. This dependency is illustrated in figure 4.3. The calibration is performed by measuring the intensity of visible light, which approximately is of wavelength 390 to 700 nm, while the wavelength of the strongest OH* chemiluminescence emission band is found at 310 nm (Nau et al., 2012). This implicates that the refraction from the glass for the light spectra used for the calibration and the light spectra measured in the experiment were not the same, and was a possible source for errors. However, it was assumed that the error introduced by this was negligible compared to other problems.

As stated in the start of this section, light passing through the enclosure will refract. Due to the curvature of the glass and Snell's Law of refraction, non-uniform distortion will be introduced to the objects inside of the enclosure. The nature of this distortion is also expected to change for the different views, due to the changing entry angle of the LOSs unto the quartz glass. To investigated the nature of this distortion, and if it introduces calibration problems, images from the mock setups were used. The burner plate was positioned at different angles, θ, with the calibration plate mounted in. Images of the plate was captured with, and without the quartz enclosure, calibrations performed, and errors compared. Results from this test are found in section 5.2.
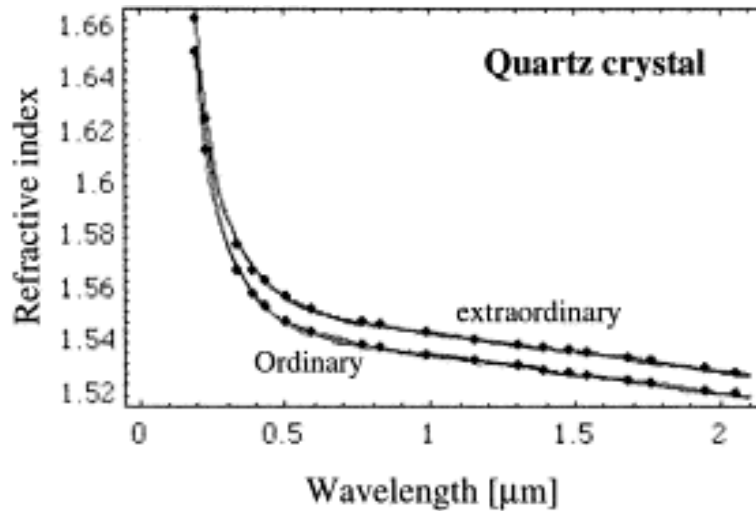
Figure 4.3: How refractive index changes for different wavelengths of light for quartz crystal. Ordinary and extraordinary refers to the polarization of the light. (Reproduced from Ghosh (1999)).

4.2   Overview - CTC of a confined flame

Procedures of the experimental methods used for the CTC of the confined flame are presented in figure 4.4, and some are similar to the ones performed in the phantom study. The main differences were that all images were acquired from an experimental setup, and these images need some pre-processing before they were used to perform a camera calibration and tomographic reconstruction.
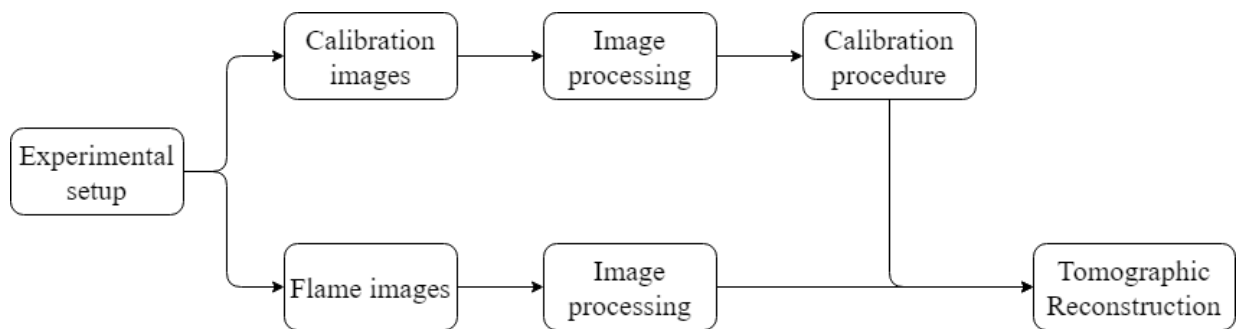
Figure 4.4: The steps of performing CTC

The next sections will describe the experimental setup used, and the pre-processing of the captured data. The polynomial calibration model described in section 2.1.6 was used to relate the experimental images to 3D space, and the tomographic methods used in the phantom study

were utilized. The methodology of these procedures are the same as described in chapter 2 and will not be repeated here, but important parameters of the methods used will be clarified.

4.3 Experimental setup

4.3.1 Burner setup

The annular combustion chamber used in the experiments is similar to the one used by Worth et al. (2017), but with some differences and modifications. The setup for the investigation of the unforced flame is presented in figure 4.5a. The modular design of the combustor allows the user to block of individual flames by switching out the tubes leading gas to the individual flames with solid bars. In this setup, all except inlets of three flames were blocked. Three premixed C_2H_4-air flames were placed on a pitch circle with diameter of $D_a = 170$ mm, where the distance between each flame was equal. A common plenum with length, $L_p = 200$ mm, and diameter, $D_p = 212$ mm, supplied the flames. A honeycomb flow straightener, hemispherical flow divider ($D_h = 140$ mm), a layer of wire wool and a series of grids were placed inside the plenum for flow conditioning and acoustic damping. The outer enclosure of the annular chamber has the diameter, $D_o = 210$ mm, and consists of a cylindrical quartz glass, providing a 50 mm high optical accessibility, a steel ring kept the glass in place. The outer enclosure was extended at the top by a steel tube, resulting in an outer enclosure height of $L_o = 120$ mm. The diameter of the inner tube was, $D_i = 130$ mm, and the length, $L_i = 200$ mm. The burners consisted of circular tubes with the length, $L_t = 150$ mm, and the diameter, $D_t = 18.0$ mm. The flames were stabilized by a conical bluff-body with the diameter, $d_{bb} = 13.0$ mm, centered in each of the burners.

Two Alicat mass flow controllers were used to regulate the airflow, and one for C_2H_4. The burners were operated at a bulk velocity of $\overline{U} = 18 m/s$ and an equivalence ratio of $\phi = 0.95$, for both the forced and unforced flames.

4.3.2 Acoustic forcing setup

The same burner setup used for unforced flames were also used for the forced flames, but equipment to perform the acoustic forcing was added to experimental rig. The setup is shown in figure

(a) Combustion chamber setup

(b) Schematic of annular burner
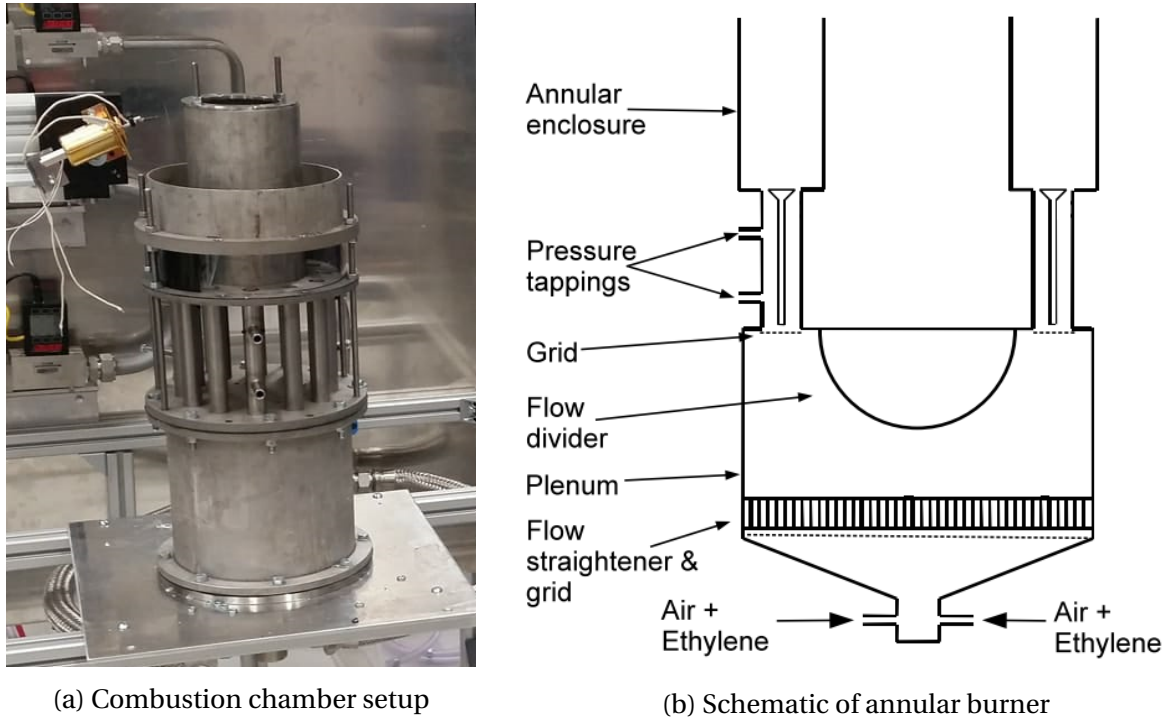
Figure 4.5: General setup of the annular combustion chamber ((b) reproduced and modified from Worth and Dawson (2017))

4.6a (Note that the pressure transducers are not mounted, nor the loudspeakers connected to the signal generator in the figure.). On top of the outer enclosing of the other setup, another steel ring was mounted. On top of that, a forcing array with four 120 mm long tubes, placed equidistant around the chamber was mounted. Each tube had an Adastra 60 W horn driver mounted in the end. Drivers opposing each other diametrically were forced in anti-phase, creating a speaker pair. The acoustic drivers were placed sufficiently high so they did not interfere with the optical accessibility. To create the forcing outputs, a multichannel waveform generator Aim-TTI TGA1244 was used together with a QTX PRO 1000 amplifier.

For a perfect geometry of the acoustic array and ideal speaker response, a standing wave could be created by setting all forcing amplitudes equal and zero phase delay between them. Introducing a phase delay of $\pm90°$ would create a spinning mode. For the experimental setup, amplitudes and phase delays are adjusted based on pressure measurements to achieve the desired response (Nygård et al., 2018). The acoustic forcing was tuned to create a spinning mode with $SR = 1$, in the cold combustion chamber.

As discussed in section 1.2.3, the flame separation distance, S, is an important parameter
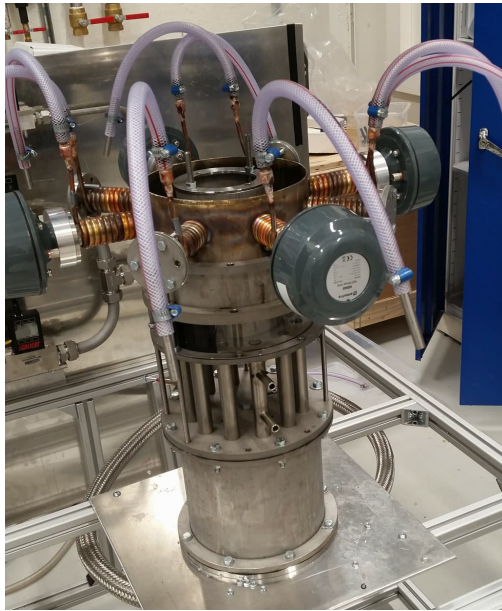
(a) The experimental setup with acoustic drivers mounted on top.
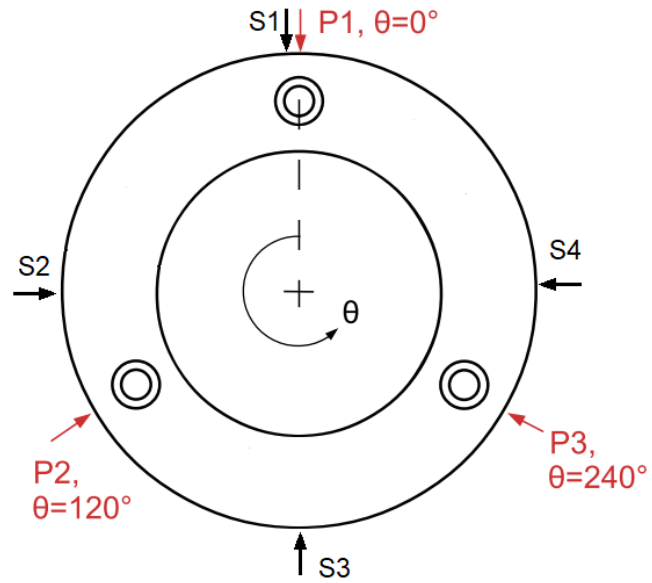
(b) Positions of the drivers (S) and pressure sensors (P)

Figure 4.6: Setup of the annular combustion chamber with acoustic forcing ((b) reproduced and modified from Worth and Dawson (2017))

when investigating azimuthal stability. However, in this current setup the flames are assumed not to affect each other, meaning the separation distance is not of interest. The reason for keeping three burners open even though only one flame is to be reconstructed is to be able to measure the pressure oscillations in the chamber during the forcing of the flame, thus characterize the forced azimuthal mode. To identify the response of the acoustic forcing, pressure was measured at all the three annular locations, P1, P2 and P3, as seen in figure 4.6b. Pressure was measured using Kulite XCS-093-05D pressure sensors, with a measurement sensitivity of 4.2857×10^{-3} mV/Pa, mounted flush with the inner wall of the tubes, 45 mm below the dump plane. A Fylde FE-579-TA bridge amplifier was used to amplify the signal before logging them at a sampling frequency of 51.2 kHz.

4.3.3 Imaging system

To capture the heat release distribution, high-speed OH* chemiluminescence images were obtained through the outer enclosure made out of quartz glass with a single Photron SA1.1 high-speed CMOS camera coupled with a LaVision IRO high-speed two-stage intensifier. This was

fitted with Cerco2178 UV lens equipped with a D20-VG0035942 optical filter with a bandwidth of $305 - 315$ nm. The aperture setting was $f = 1/2.8$. The imaging system was mounted on a stand made out of aluminum profiles at the same height as the annular combustion chamber burners, and at a distance of approximately 600 mm away from center of the investigated flame. To keep the same distance between the burner and the cameras for the different views, the camera stand was mounted to a hinge which was centered under the flame being investigated. Image resolution was 640×656, giving an approximate resolution of 7 pixel/mm. To reduce the possibility of reflections affecting the camera views, $\frac{2}{3}$ of the inside of the quartz enclosure was coated with a mat black, heat-resistant paint. The section not painted provided the required optical accessibility.
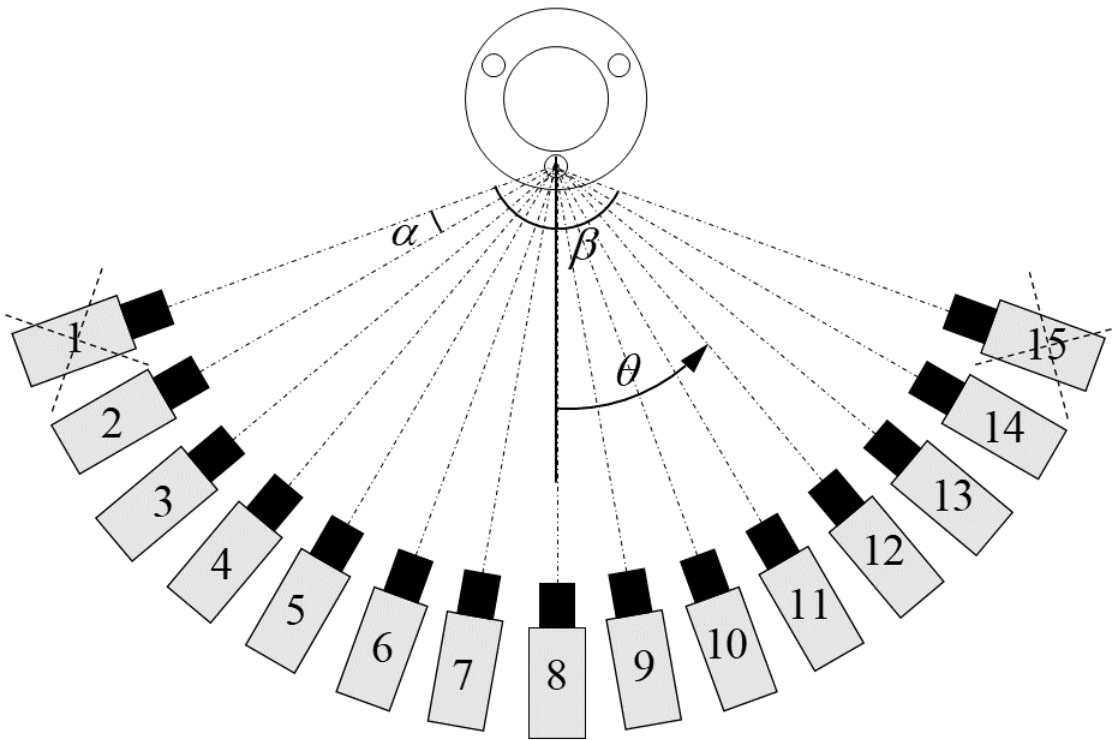
Figure 4.7: Camera positions where experimental data was acquired. $\beta = 140°$, while $N_c = 15$, with equal camera spacing, $\alpha = 10°$. Angle θ is used to refer to the different views. The crosses indicates which views that were not used in the final data processing.

For both the unforced and forced flame, images were acquired from the positions illustrated in figure 4.7 by re-positioning the camera described, making the experimental setup cost-effective due to only requiring a single camera. Data from 15 camera views was recorded, with a total view width, $\beta = 140°$, making the angular spacing between neighbouring views $10°$. For
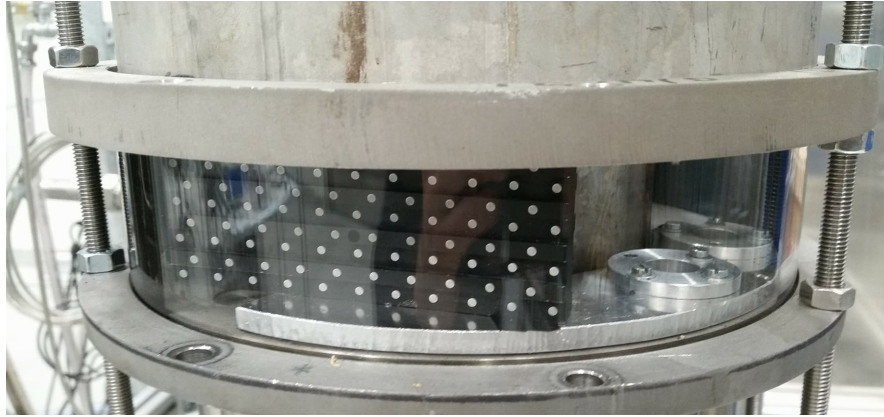
Figure 4.8: The calibration plate placed inside the annular burner.

the unforced flame, 1000 images was captured at each position at frame rate of $f_{cam} = 0.1kHz$. For the forced flames, a frame rate of $f_{cam} = 10kHz$ was used, and 20000 images captured.

Also, 50 calibration images for each position was acquired. A dual-plane calibration plate with 11×11 and 10×10 dot patterns was placed inside the burner using the device described in section 4.1.2. Dot spacing of the plate was 10 mm in both directions, and the distance between the two planes were 2 mm. An illustration of the calibration plate placed in the burner is shown in figure 4.8. Due to the width of the image covered by the calibration plate for wide camera positions is reduced, a larger calibration plate than what was originally intended was used to make sure the relevant area of the image was covered by the plate.

4.4 Data pre-processing and mode characterization

Before performing the calibration procedure and tomographic reconstructions, the images acquired had to be pre-processed. Image resolution of the recorded images was 640×656 pixels. Parts of the images were not of interest, as they only displayed areas outside of the burner. These parts were cropped away for both flame- and calibration images. The final resolution of the processed images were 640×400 pixels.

For the unforced flame, mean images were calculated using the 1000 images captured for each position. The intensity of the images were added together, and divided by the number of images. The images was then scaled such that the largest pixel intensity count in the image set was 100, which sets the dynamic range. An example of a single image of the flame, and the mean

image from the same position is illustrated in figure 4.9

(a) Single image of the mean data

(b) Mean image of the data
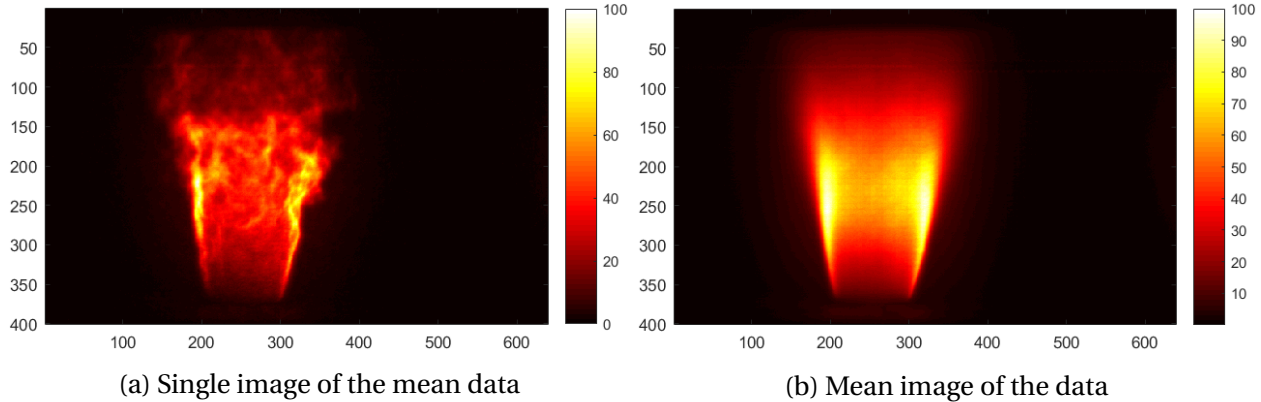
Figure 4.9: Example of a single image, and a mean image from the mean data. Images displayed are from the 8th view.

(a) Phase angle: 0°

(b) Phase angle: 180°
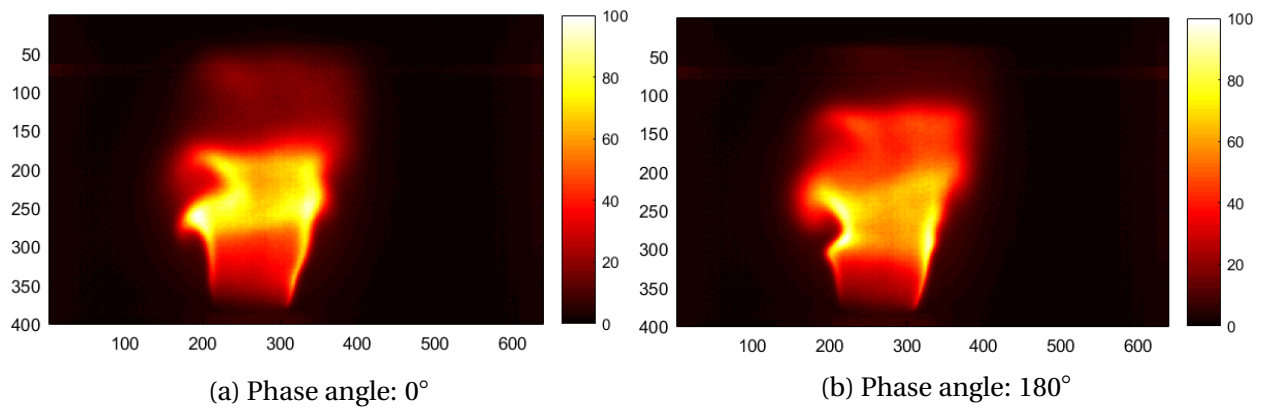
Figure 4.10: Examples of phase averaged images from the 8th view.

The images of the forced flame required more advanced processing. Based on the pressure measurements of the microphone at position P1, the images of the forced flame were binned into 12 phase-angles of the oscillation cycle with help from Postdoctoral Fellow, Marek Mazur. Between 1000 to 1200 images for each phase-angle for each view were binned together. These images were used to create 12 phase-averaged images for each camera position. This was done by adding them together, and divide them by the number of images. The phase-averaged images were scaled in the same way as the mean images such that the highest pixel intensity count in the image set was 100. An example of phase-averaged images from the same view for two different phase angles is found in figure 4.10. The mean images of the forced flames were also analyzed, and these were created by adding all the images for the different phases together and scale them

in the same way as all the other image sets.

To characterize the forced mode, the pressure measurements were used. By consider the forced azimuthal modes to be a pair 1D acoustic waves travelling around the annulus in opposite direction, the pressure fluctuations can be described by the real part, $\mathbb{R}(p_k)$, where p_k is defined by equation 1.2. The equation is solved for A_+, A_- and $v_\theta t / R$ by summing the pressure time-series into one series, $C(t)$, which is defined as:

$$C(t) = \frac{1}{N} \sum_{k=1}^{N} p_k(\theta_k, t) e^{i\theta_k} \tag{4.1}$$

Method of least squares is applied to intervals of $C(t)$ to approximate A_+, A_- and $v_\theta t / R$ (Wolf et al., 2012). These results can then be used to determine the spin ratio SR, that is defined by equation 1.3. The pressure fluctuation of any azimuthal mode is given by $\sqrt{A_+^2 + A_-^2}$, and the behavior of the nodal line was investigated by analyzing the term, $v_\theta t / R$.

4.5 Calibration

For calibration, 50 images were captured of the calibration plate placed inside the combustion chamber for each camera position, and mean images was created. The polynomial calibration method described section 2.1.6 was used, and relates all the images from each view to the global coordinate system defined in figure 4.11. Polynomials of order 3 were used for all the calibrations.
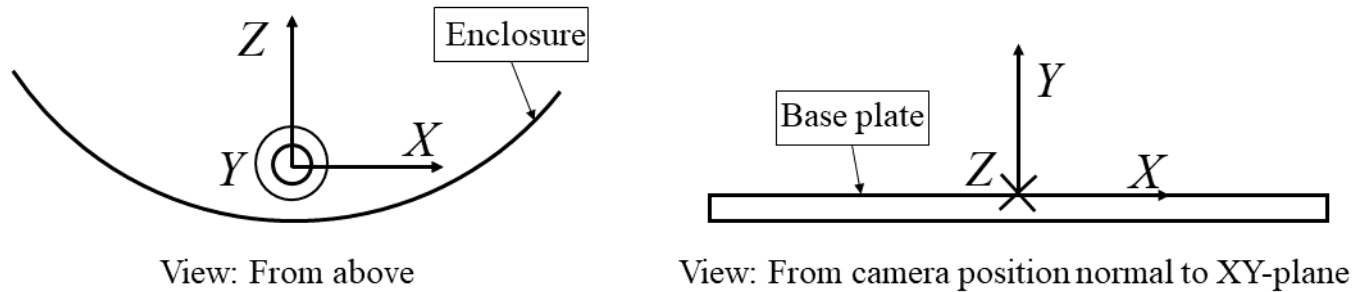
Figure 4.11: Global coordinate system defined.

As stated earlier, data was captured for a setup with $N_c = 15$, camera views and a setup width of $\beta = 140°$, but due to calibration problems for the outer views positioned at $\theta = -70°$ and

$\theta = 70°$, or camera 1 and 15 as seen in figure 4.7, data for these views were not used in the reconstructions. The problems originate from the fact that parts of the calibration plate were located far away from the plane of focus, leading to multiple of the calibration points being too unfocused to find in the calibration procedure. This is further discussed in section 6.2.3. The remaining data is the same that would be acquired from a $N_c = 13$ and $\beta = 120°$ setup, meaning this was the actual setup for the performed reconstructions. Mean errors of the calibration of all the utilized views are illustrated in figure 4.12. Results from the phantom study showed that changing the iteration sequence of views prone to calibration error could be beneficial for the reconstruction quality, however this was not done for the reconstructions performed here.
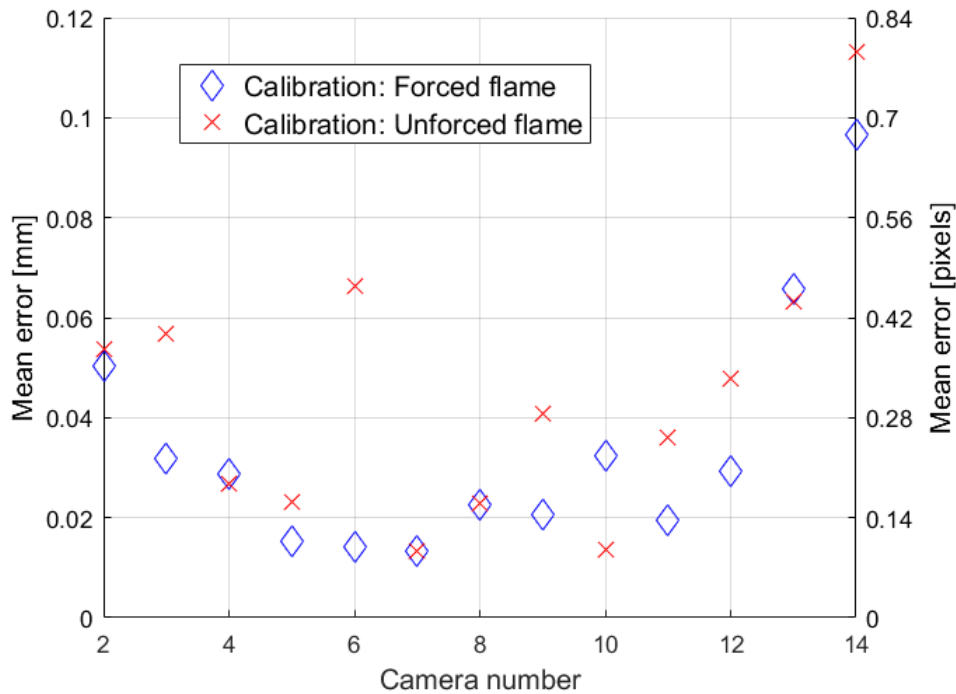
Figure 4.12: Mean calibration errors of the utilized camera views for both the forced and unforced flame experiment.

4.6 Tomographic reconstruction

When the calibration and pre-processing of the images were done, the same tomographic methods as described in section 2.1.7 were used to reconstruct the 3D OH* chemiluminescence distribution for both the unforced, and forced flame images. For the unforced flame, a single 3D

voxel volume was reconstructed for the mean OH* chemiluminescence distribution. While for the forced flame, a mean volume, as well as phase-averaged volumes were reconstructed for each of the 12 phase-angles. All the final volumes was Gaussian smoothed with a kernel of $\sigma = 2$ to reduce reconstruction noise. Finally, the volumes were scaled such that the highest voxel count in each volume was 6. Parameters of the reconstruction are presented in table 4.1. The discretization of the volume was set to 8 voxels/mm to get a pixel to voxel ratio close to 1. The image resolution determines the possible resolution of the volume, and refining the volume more is assumed to not give any more volumetric information.

Table 4.1: Experimental parameters

Domain	$40 \times 50 \times 40 mm^3$
Discretisation	8 voxels/mm
Camera distance	$600 mm$ from global origin
Initial guess	MFG
MART iterations	$n = 5$
Relaxation factor	$\mu = 1.0$

Chapter 5

Results and discussion

In this chapter will results from the mock experiment be presented and discussed first. Based on these results possible problems of with the final experiment were identified. Finally, the results from the computed tomography of OH* chemiluminescence of the confined flame, both unforced and acoustically forced, will be presented, analyzed and discussed.

5.1 Re-positioning test

50 images were acquired using the procedure described in section 4.1.2. The same dot location scheme as used when performing the polynomial calibration was utilized for each re-positioning image, finding the position of each dot in each image. Point positions found in all 50 images were compared to the calculated mean positions and the error distribution is illustrated in figure 5.1b. An example of the images acquired is found in figure 5.1a. The standard deviations of the position for each dot were calculated, under the assumption that the re-positioning error is normal distributed. Standard deviation in both x-, y- and a combined r-direction was calculated for each dot.

The results for the r-direction is illustrated as a contour plot in figure 5.2. It can be observed from the results that there are spots with elevated errors centered at some of the dot positions. One can assume that an inaccurate re-positioning will result in errors for all dot locations, meaning that the error contour should have an elevation spanning over a larger area than just a single dot if the problem was the re-positioning. This leads the author to believe that the
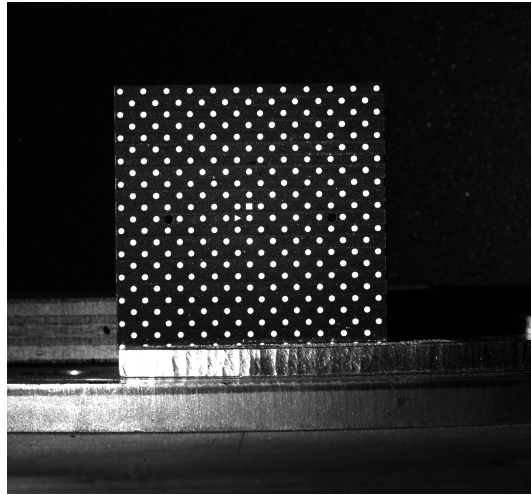
(a) An example of the images used for the re-positioning test
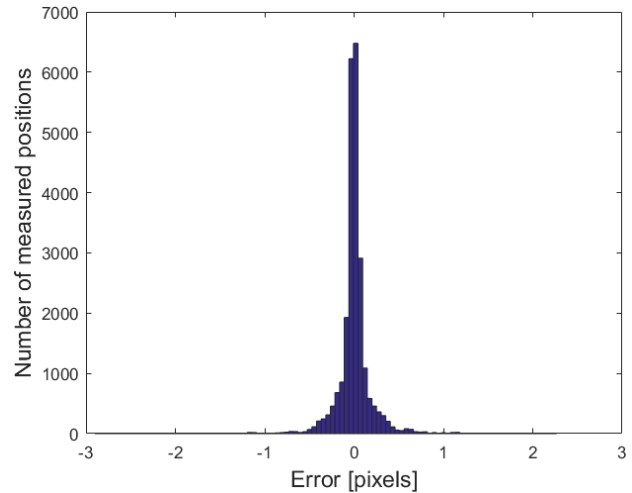
(b) Measured x- and y- positions for 50 images compared to the mean positions.

Figure 5.1

error of re-positioning was of an order equal to, or possibly lower than the accuracy of the dot searching scheme. This indicates that re-positioning of the calibration plate in the mock setup was possible with a satisfying degree of accuracy.

Possible reason for problems in the dot searching scheme are image noise and uneven lighting of the calibration plate for recorded images, indicating that these aspects of the experimental setup can be just as problematic as the re-positioning of the calibration plate.

5.2 Refraction test

Images from the mock experiment with different θ, and with, and without enclosure were analyzed. Polynomial calibrations of order 3 of the different images were performed, and the mean errors for the different calibrations were calculated. Mean errors with regard to viewing angle are visualized in figure 5.3. It can be observed that for all calibrations performed, the quartz enclosure consistently degrade the accuracy of the calibration polynomial for all view angles θ. Calibrations performed at large angles with the quartz enclosure present were clearly the most problematic ones based on the presented results. This was also limiting for the final annular combustion chamber experiment as described in section 4.5, where calibrations at $\theta = \pm 70°$ were unsuccessful.
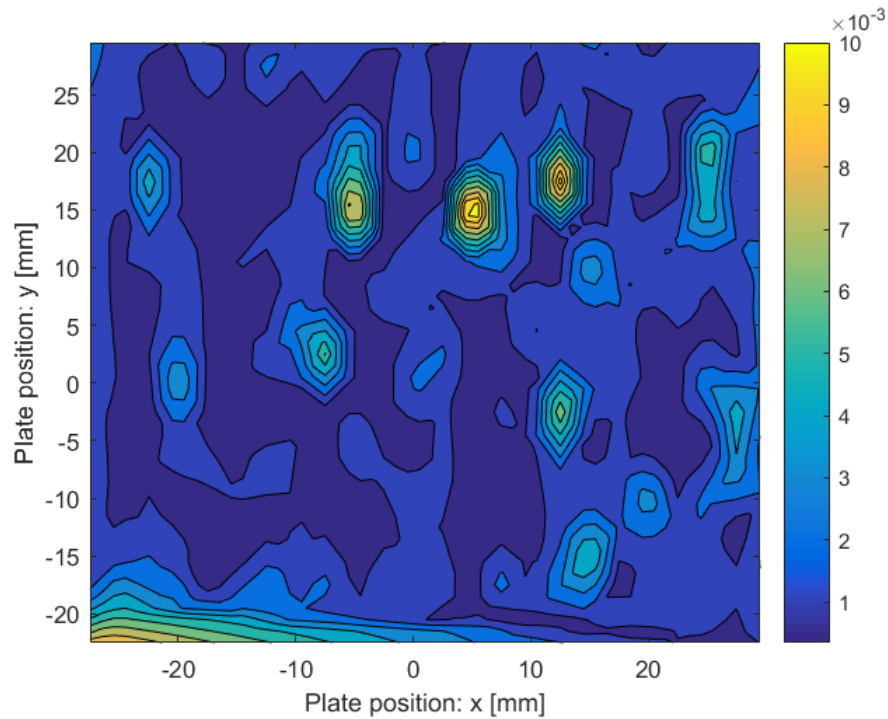
Figure 5.2: Contour plot of the calculated σ_r for the dot positions. The value of σ_r is indicated by the color bar and given in mm.

It is believed that there are two possible main reason for degraded calibration accuracy with the quartz enclosure. One is that the enclosure makes it harder to get a uniform lightning of the calibration plate, which will cause inaccuracy in the dot searching performed during the calibration. Error in the point locations would definitively degrade the calibration and thus the final result. But since the calibration procedure fits polynomials to the found points, and the error here was evaluated by comparing the polynomials to the points, erroneous point locations would not necessarily affect the error calculated in figure 5.3.

The other suspected reason is that the enclosure introduces a new non-linearity that the polynomial model have to fit. Such non-linearities would be expected to complicate to mapping between image- and global coordinates. One could try to model the refraction physically using Snell's Law of refraction, the geometry of the enclosure and the pixel LOSs, and include this in the camera model. However, this would require much work due to the complexity of the setup. The complexity of the refraction was one of the reasons a polynomial camera model was chosen over a pinhole model. Further investigation could test how polynomial calibration of other orders performs, but this was not done due to time limitations.
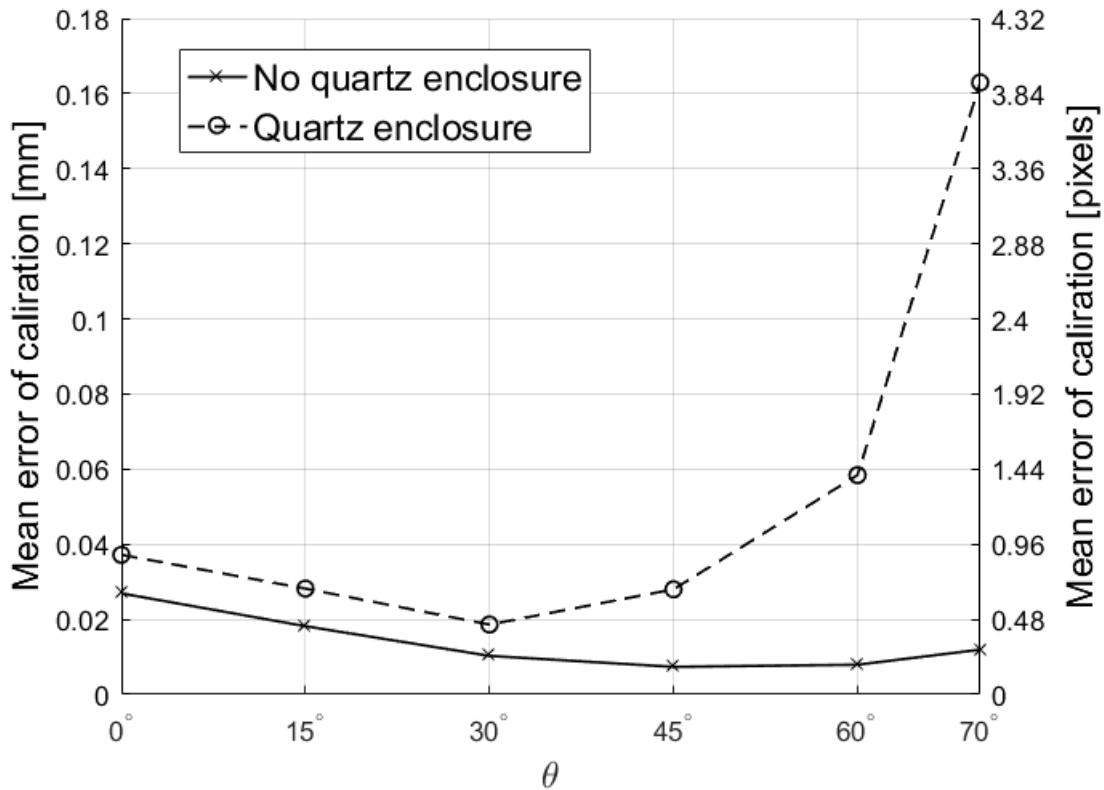
Figure 5.3: The mean error of the polynomial calibration model compared to the points they are based on plotted against view angle θ.

To get a better understanding of the nature of the refraction, images taken from different θ, with and without the enclosure were compared to each other. The resulting images are presented in figure 5.4. For the case where $\theta = 0°$, the dots moves outwards in each direction at each u-side of the image, as would be expected due to the symmetry of the enclosure for this view.

At $\theta = 30°$, it is observed that the "movement" of the dots is consistently to the positive u-direction, and increasing for dots at higher u-positions. The consistency of direction for the distortion pattern may be why the calibration polynomial for $\theta = 30°$, is the one that bests fit the calibration points as observed in figure 5.3.

(a) $\theta = 0°$

(b) $\theta = 30°$

(c) $\theta = 70°$
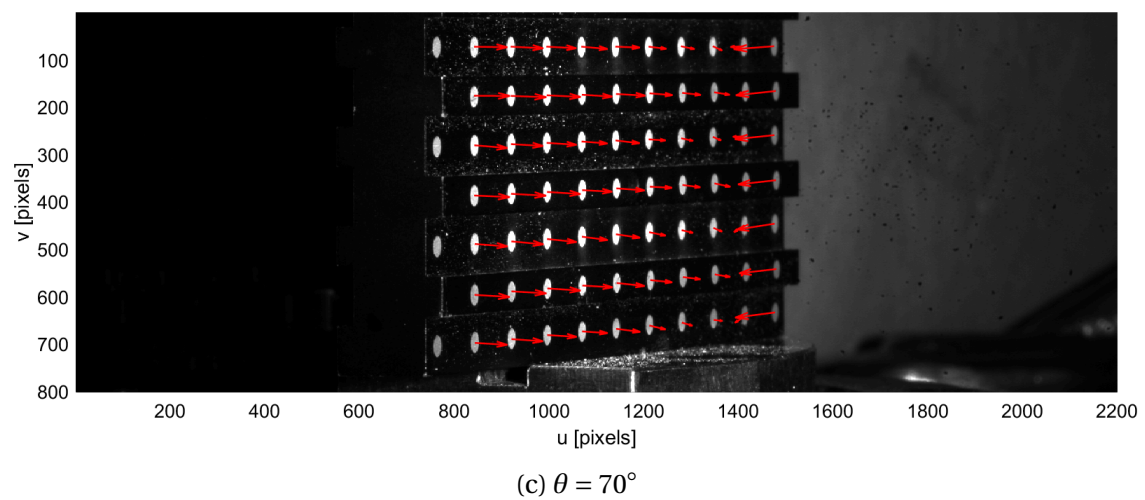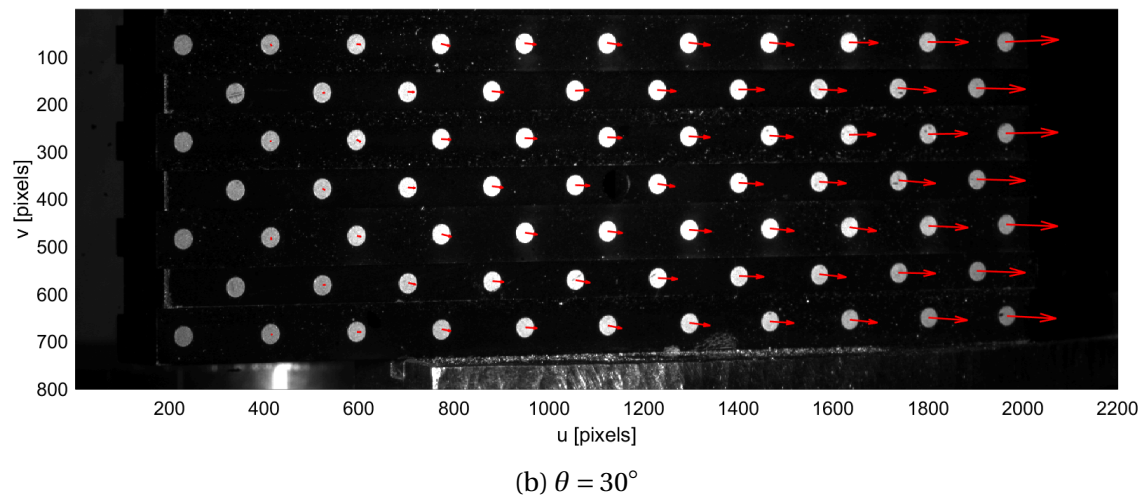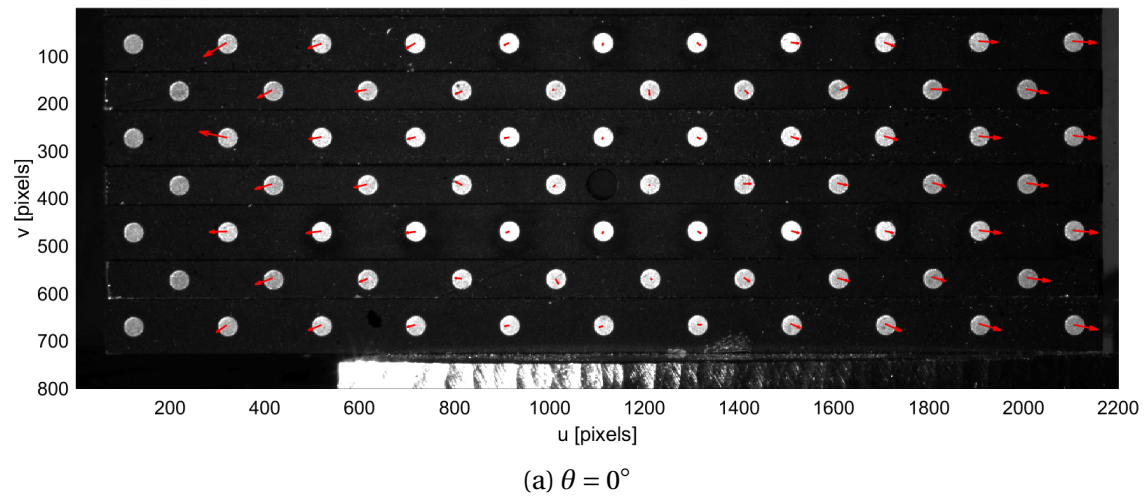
Figure 5.4: Calibration images from different angles with no enclosure. The red arrows indicate how the dots move when the enclosure is present. Length of arrows are scaled up by 4 to clarify the movement pattern.

The most interesting results are observed for $\theta = 70°$ where the same consistency as for $\theta = 30°$ seems to be present, only with decreasing movement in positive u-direction. However, for the last calibration points, the pattern rapidly changes nature, and points are moving in negative u-direction with large magnitudes. This rapid change in the distortion pattern may be the reason why the polynomial calibration have the highest mean error for this setup angle. These result also shows that for investigations with complex distortion patterns like the ones present here, extrapolating calibration models outside of the image area covered by the calibration plate is unadvised.

Based on the refractive test, using a large calibration plate that covers the relevant parts of the image is advised in order to not have to extrapolate the polynomial camera models. Alas, some extrapolating have to be done in order to cover the parts of the image close to the base plate of the annular combustion chamber. Future experiments should try to avoid this, but based on the test performed here, the current setup is accepted due to the less complicated distortion changes observed in the vertical v-direction than in horizontal u-direction.

If one compares the results from figure 5.3 to the calibration errors seen in figure 4.12 from the CTC experiment there is some coherence. The calibrations performed for the unforced flame have a more chaotic trend then the one for the forced flames, where some of the calibration error for the views close to normal to the calibration plate have sudden elevated errors. But the calibrations for the forced flames seems to have a more consistent trend where wide views have a generally higher mean calibration error. This trend seem somewhat shifted towards the cameras placed at the widest positive θ-directions. This may be due to the reference angle $\theta = 0°$ is not completely normal to the circumferential direction of the enclosure, but positively shifted. Such a shift would result in the widest positive θ angles to be wider than intended, while the widest negative angles would be narrower than intended. Another possibility is simply that the lightning of the calibration plate was more even and appropriate from one side over the other.

5.3   Mean unforced flames

The mean OH* chemiluminescence of a single unforced flame confined by the annular enclosure was reconstructed. Slices of the reconstructed volume are illustrated in figure 5.5. From figure 5.5a it is observed that the reconstructed OH* chemiluminescence distribution for the mean flow is somewhat circular, but the intensity varies around the circumferential. This is also clear from the volume slices presented in figure 5.5b and 5.5c, where the intensity at each side of the bluff body is not symmetrical.

It is already shown in the phantom study that a narrow view width β can cause asymmetries in the reconstruction of a symmetrical phantom object. The reduction of the view width from 140° to 120° of the utilized views may be one of the reasons for asymmetries. However, several other factors of the experimental setup may cause this as well. The position of the bluff body in the burner is positioned and adjusted by hand, and small inaccuracy in the centering of the bluff-body may change the flow pattern of the reactants and cause the observed asymmetries.

It is also observed that the zones of heat release at opposing side of the bluff body from figure 5.5b and 5.5c starts at different Y-heights. This may be due to the suspected asymmetric flow pattern caused by the inaccurate positioned bluff body. Another possibility is that the calibration plate was not positioned accurate enough inside the annular chamber with regard to the burner position. Ideally, the Y-axis should be normal to the base plate and centered in the bluff body, and this is dependent on the positioning of the calibration plate. Due to the fact that the re-positioning device was not originally designed for the calibration plate used in the experiment, and that the base plate of the annular combustion chamber was prone to some structural deformation when mounted, the author believe this to be a possible cause for the uneven height of the start of the heat release zones. In other words, the reconstructed heat release is equally inaccurate positioned, and possibly tilted in the voxel volume the same way the calibration plate was when positioned in the combustion chamber.

Another possible explanation is that the OH* signal strength close to the base plate is too weak to capture, due to the thin flame brush here. This was also observed by Worth and Dawson (2013c) where several gaps were observed in the volume sheets close to the base plate of their burner.

Based on the observations from the reconstructed mean heat release of the unforced flame, it is obvious that there are already some asymmetries of the heat release of the flame before forcing an azimuthal mode. Due to this, it is recommended to perform mean unforced reconstructions in conjunction with forced reconstruction in order not to attribute features of the forced results incorrectly.

(a) XZ-slice at $Y = 20$ mm

(b) XY-slice at $Z = 0$ mm

(c) YZ-slice at $X = 0$ mm
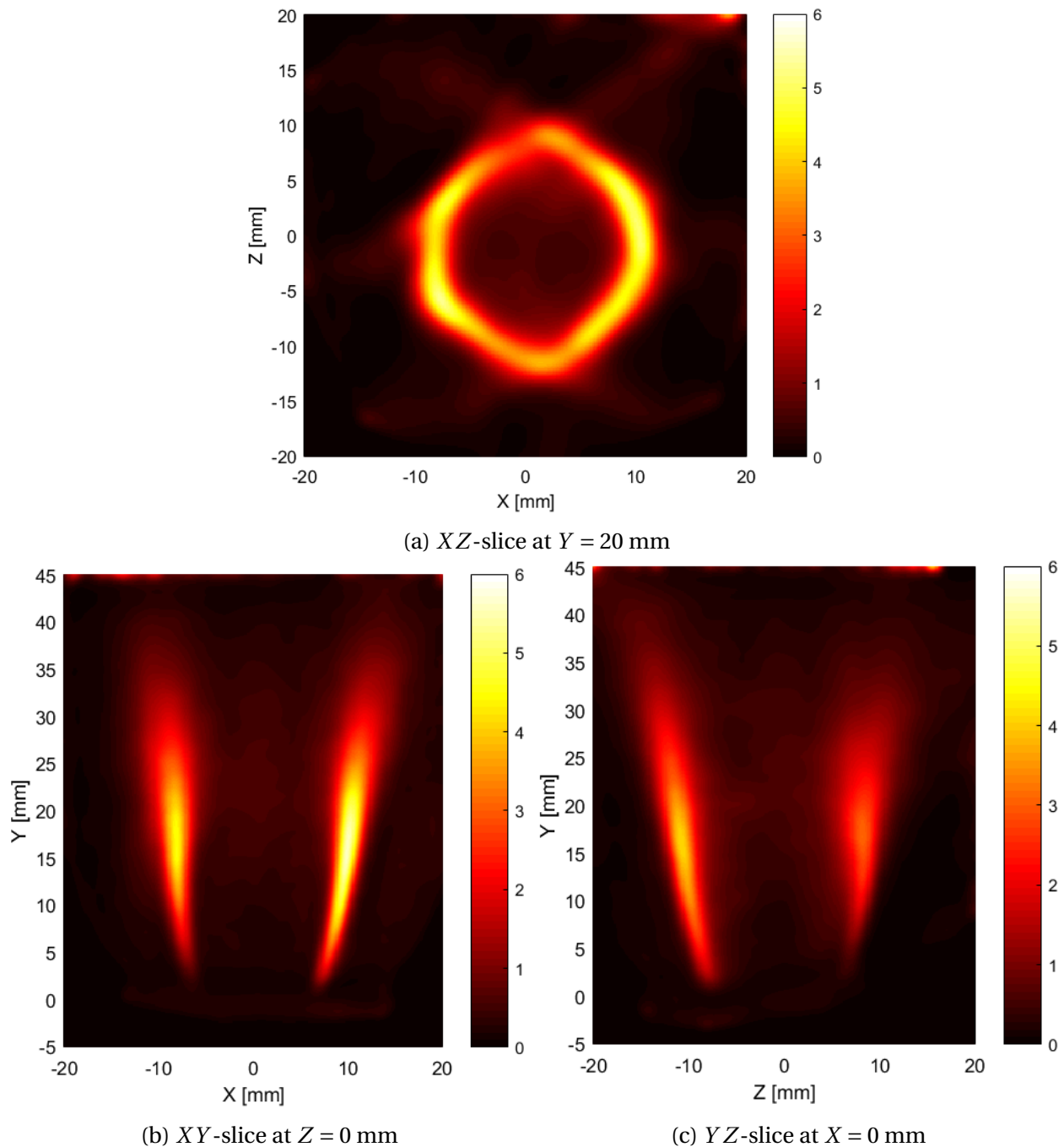
Figure 5.5: Slices of the unforced, mean heat release.

5.4 Forced flames

5.4.1 Mode analysis

In order to characterize the azimuthal mode related to the reconstructed heat release of the acoustically forced flames, the pressure readings were analyzed. Calculating the spin ratio proved to be more problematic than expected, due to one of the pressure sensors being incorrectly calibrated. But a mean spin ratio of $SR = 0.26$ was estimated by re-calibrating the pressure transducers and correct the pressure readings in terms of amplitude and phase. A sample of the re-calibrated pressure series over 6 periods of oscillation cycles is illustrated in figure 5.6. The frequency of the forced oscillation cycles was 955 Hz, while the mean amplitude of the pressure fluctuations of the mode was, $\sqrt{A_+^2 + A_-^2} = 397.7$ Pa. For a pure spinning mode, the amplitude of all pressure measurements would be equal and phase shifted 120° from each other. This is clearly not the case from the sample from figure 5.6.

Based on the spin ratio, the azimuthal mode was mixed between ACW spinning and standing, and makes the current case one of the most challenging to analyze qualitatively. Optimally pure standing and spinning modes should be investigated separately first, before mixed modes.
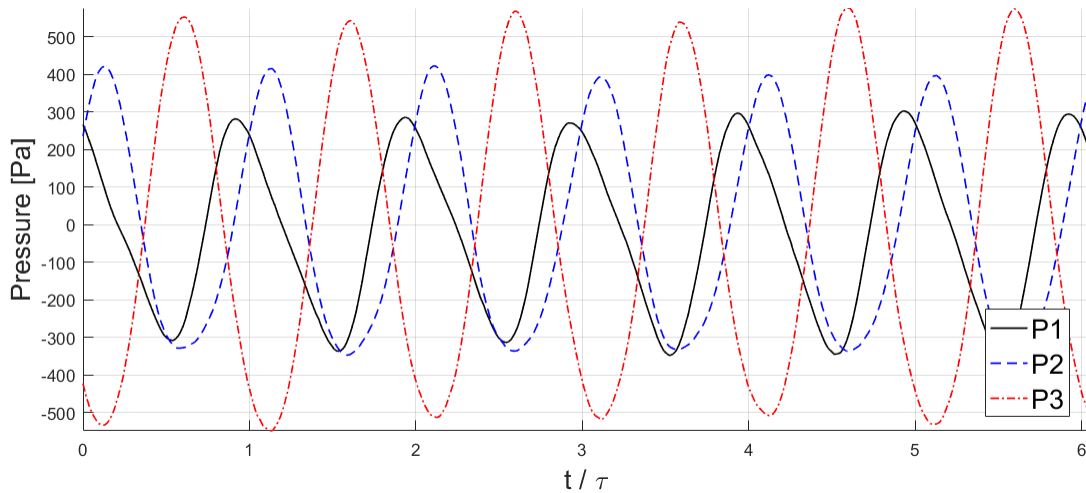
Figure 5.6: Pressure series.

Although the acoustic forcing was tuned to force a azimuthal mode close to $SR = 1$ in the annular chamber, the same mode was not estimated based on the pressure readings. One reason could be that the re-calibrated pressure series were incorrect, and thus the estimated spin ratio.

Another possibility was that while the tuning of the mode was performed in a cold chamber, the acoustic properties changes significantly during operation of the combustion chamber and therefore also the forced spin ratio. The author have too little experience with the experimental setup to qualitatively determine which of the suspected reasons are the main problem.

However, under the assumption that the pressure series was properly corrected, the standing part of the forced mode can be characterized by identifying the orientation of the nodal line. From the pressure series analysis, v_θ was found to vary from $2.5 - 2.8$ m/s over the measured series, meaning the nodal line was found to continuously rotate with an angular velocity of $v_\theta / R = 29.4 - 32.9$ rad/s. For an image acquisition period of 2 seconds, this means that the nodal line rotated approximately 10 times during this period.

For a standing azimuthal mode, Worth et al. (2017) observed that close to the pressure nodes, asymmetric heat release were found, indicating large transverse velocity fluctuations. At anti-nodes, a high degree of symmetry for the heat release were observed. Large axial, and low transverse velocity fluctuations are associated with this behavior. Since the nodal orientation is constantly spinning, and the oscillation cycles have a much larger frequency than the rotation of the nodal line, it is assumed that the phase-averaged images of the forced run will consist of images captured for all orientations of the nodal line. This implies that the flame dynamics caused by the standing part of the forced azimuthal mode will be averaged with regard to nodal orientation for the phase-averaged images, and the averaged dynamics will also be found in the reconstructed objects. For a more thorough investigation of such a mixed azimuthal mode, it would be necessary to sort the experimental images by the orientation of the nodal line as well.

Images were captured during 10 rotations of the nodal line, a longer acquisition period would be preferred to get better statistical mean images, with regard to nodal orientation.

5.4.2 Mean forced flame

3D mean heat release of the acoustically forced flame was reconstructed. The same slices as displayed in figure 5.5 for the unforced flame are illustrated in figure 5.7 for the forced flame. From figure 5.7a it is clear that there are some reconstruction artifacts in the volume. A line in the periphery of the flame, as well as intensity accumulations located close to the volume limits are observed. Compared to the mean, unforced volume heat release, the forced flame is more

scattered, indicating a transient flame dynamic over the pressure oscillation cycles.

(a) XZ-slice at $Y = 20$ mm

(b) XY-slice at $Z = 0$ mm

(c) YZ-slice at $X = 0$ mm
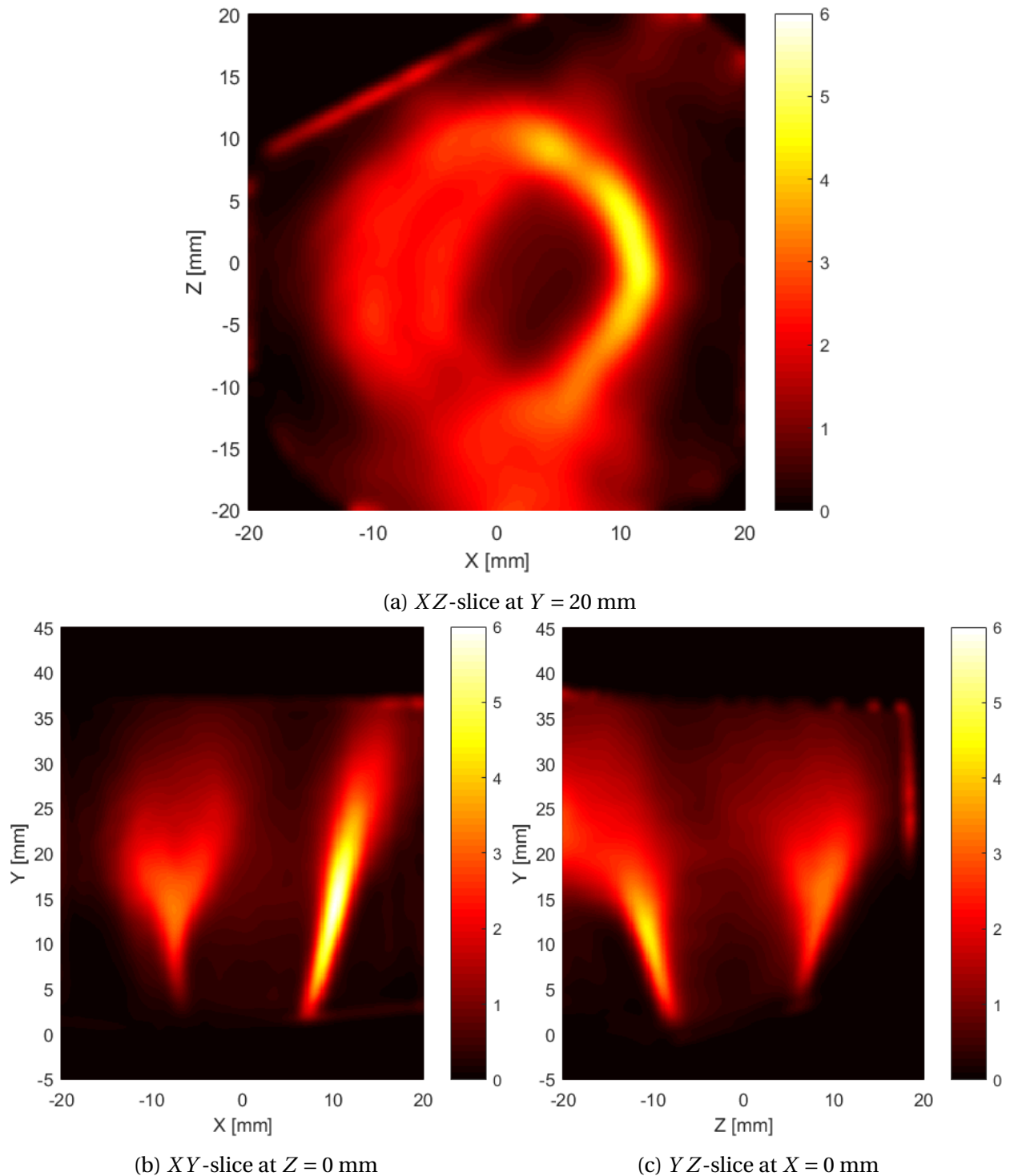
Figure 5.7: Slices of the forced, mean heat release.

By comparing figure 5.5b and 5.7b it is also indications of a more steady behavior of the

flame located at the positive X side, meaning that the acoustic forcing most likely introduces new asymmetries in the heat release of the investigated flame.

5.4.3   Phase-averaged forced flame

3D heat release was reconstructed for 12 phase angles, using phase-averaged images. The XY-slices of the reconstructions are illustrated in figure 5.9. As mentioned, the phase-averaging is based upon the pressure measurements at position P1, and how the phase angles are related to the pressure series are illustrated in figure 5.8. There is a delay between when the pressure wave reaches the flame and when it is measured due to the distance between the base plate of the burner and the position of the pressure transducer. This delay is crudely estimated based upon the time an acoustic wave uses to travel this distance in air at $T = 300$ K. This phase-shift is illustrated in figure 5.8
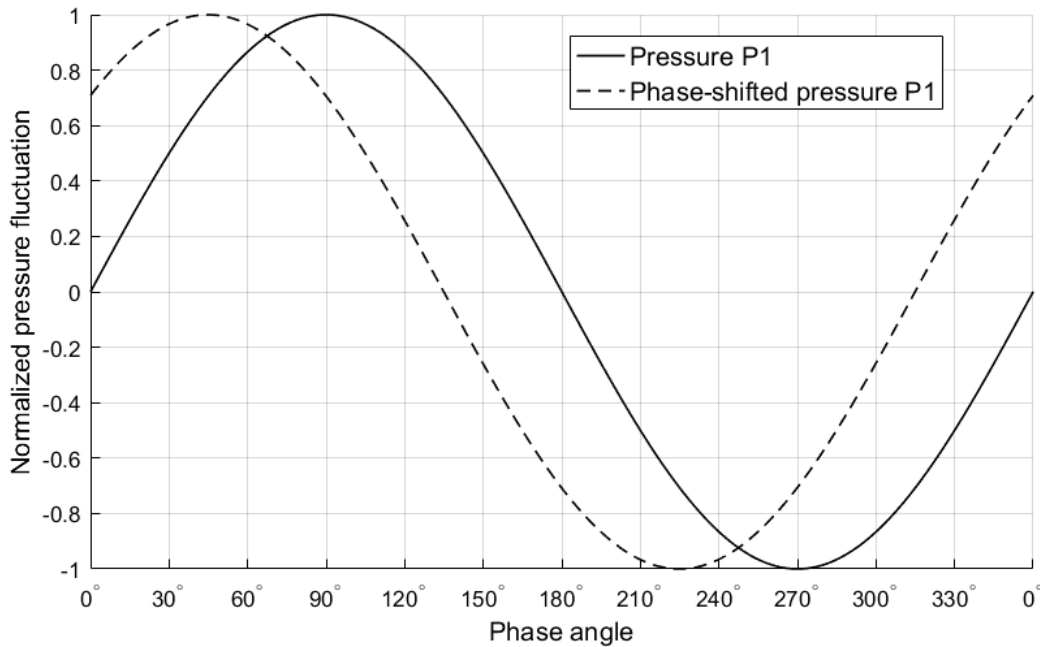
Figure 5.8: Pressure - phase-angle relation.

It is assumed that the maximum pressure is related to when the ACW spinning component of the mixed azimuthal mode reaches the investigated flame. Based upon the estimated phase-shifted pressure-phase-angle relation, this happens between phase-angle 30° and 60° for the investigated flame. An ACW spinning mode component will hit the investigated flame from the

negative X side, and it is observed that the flame dynamics of this side is far more complicated than for the opposite side in the volume slices from figure 5.9. This behavior indicates that the pressure wave is damped when hitting the flame brush at negative X-side. Although the dynamics are complicated, there seems to be a continuity between the phase-angles, indicating that the phase-averaging of the images was performed properly. These results also indicates that the reconstructed OH* distributions are sufficiently resolved to capture this flame brush motion.

At phase angles 300°, 330° and 0° the structure of the flame located at negative X-side located close to the base plate of the burner seems to be less disturbed compared to the rest of the phase-angles. But at phase-angle 30°, the lower flame brush at the negative X-side moves towards the center of the flame and develops a complicated vortex structure over the next phase-angles. This flame dynamic indicates a disturbance hitting the flame at approximately phase-angle 30°, which do support the assumption that the pressure wave of the ACW spinning azimuthal mode part reaches the flame at around phase-angle 30° and 60°.

Based on the flame brush on the positive X-side there appears to be a variation of heat release over the oscillation cycle. The intensity fields of OH* chemiluminescence seems to be lowest for the phase-angles 90° − 240°. This is further analyzed by investigating images of the summation of OH* chemiluminescence over the Y-direction, which would correspond to overhead planar OH* images of the flame.

These images are illustrated in figure 5.10, and all images contains a reconstruction artifact similar to the one observed in figure 5.7a. The intensity of the artifact line is varying with phase-angle, and the intensity seems to be related to the overall intensity of the volume, indicating that the artifact may originate from a self-reflection of the investigated flame.

The same intensity oscillation behavior from the XY-slices is observed in the overhead images as well, and may indicate that the high pressure wave passing over the burner at phase angle 30° − 60° halts the exit velocity of the flow, resulting in less reactants reaching the flame, thus less OH* chemiluminescence in the subsequent phase-angles. From the pressure-phase-angle relation, the lowest pressure is located at the phase-angles 210° − 240°, and is assumed to lead to increased exit velocity of reactants for these phase-angles. From the images 5.10i-5.10l, it is observed that the subsequent phase-angles of the pressure minimum are associated with

larger overall OH* chemiluminescence intensity. The velocity fluctuations of the exit velocity of the burner could have been calculated using the two-microphone technique (Seybert and Ross, 1977), but was not done due to time limitations.

To further analyze the asymmetry of the forced flames, reconstructed heat release for the XY-slices was divided into two sectors by the line $X = 0$. Intensity of each sector was then summed for each phase-angle, and the values were then normalized by the total heat release of each slice. This was also done for the XY-slices of the mean forced flame. The reason for using the slices and not the full volume is that if the position of the reconstructed object is inaccurate due to plate position errors, this may affect the asymmetry of the summed sectors. For the slices, the flame brushes at each side are clearly divided by the bluff body, and the positioning inaccuracy will therefore not influence the slices in the same degree. The values plotted against the phase-angles are illustrated in figure 5.11.

From the results we see that the highest degree of heat release symmetry is observed for phase-angles 300° and 330°, which is shortly before the pressure wave reaches the investigated burner. From angle 0° to 120° heat release asymmetry increases until reaching a maximum at 120° − 150°. This indicates that the ACW azimuthal mode component leads to growing asymmetries in the heat release for phase-angles closest succeeding to the phase-angle where the pressure wave hits the flame.
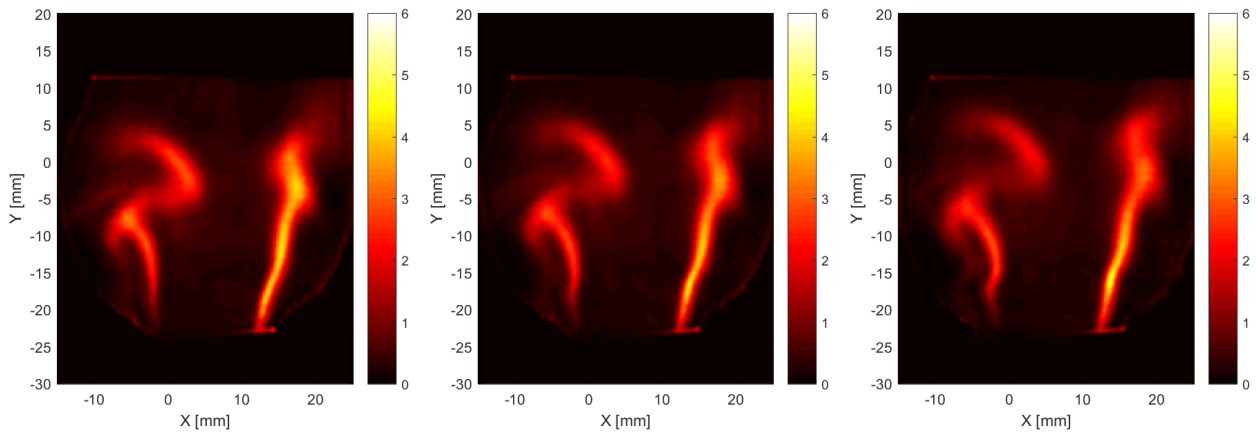
(a) XY-slice, Phase-angle: $0°$

(b) XY-slice, Phase-angle: $30°$

(c) XY-slice, Phase-angle: $60°$
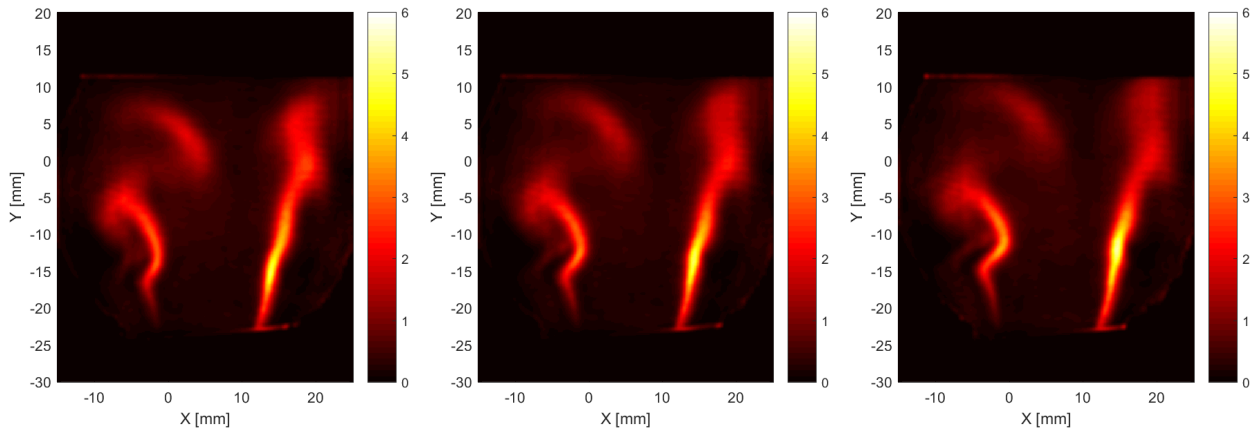
(d) XY-slice, Phase-angle: $90°$

(e) XY-slice, Phase-angle: $120°$

(f) XY-slice, Phase-angle: $150°$
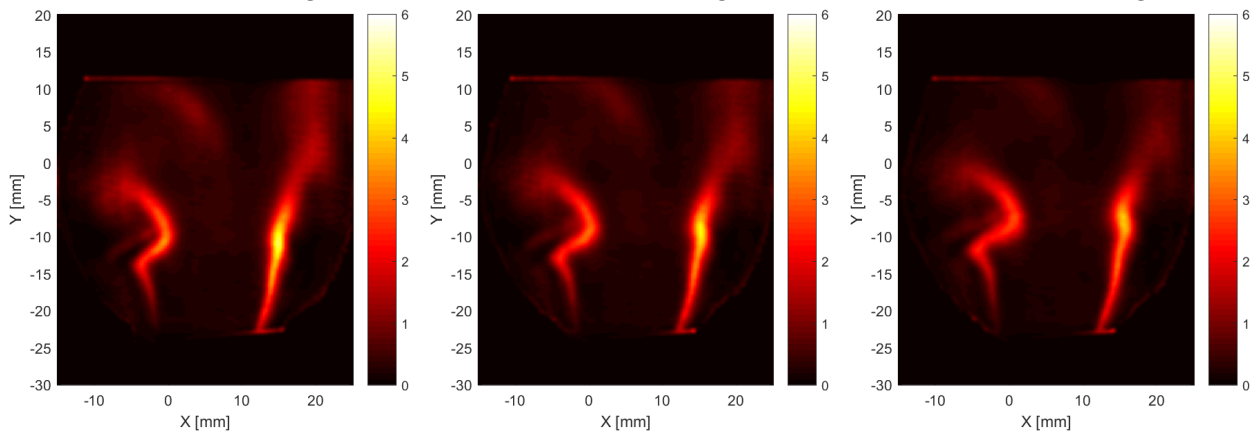
(g) XY-slice, Phase-angle: $180°$

(h) XY-slice, Phase-angle: $210°$

(i) XY-slice, Phase-angle: $240°$

(j) XY-slice, Phase-angle: 270° (k) XY-slice, Phase-angle: 300° (l) XY-slice, Phase-angle: 330°
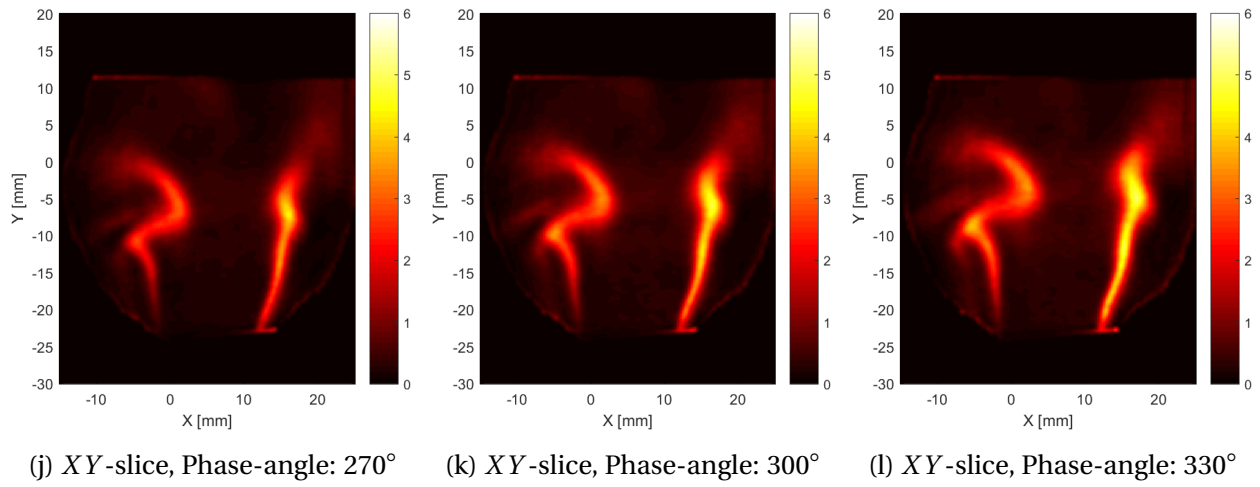
Figure 5.9: XY-slices of the volume at $Z = 0$ over a phase-averaged oscillation cycle

.

(a) Summed intensity,
Phase-angle: 0°

(b) Summed intensity,
Phase-angle: 30°

(c) Summed intensity,
Phase-angle: 60°

(d) Summed intensity,
Phase-angle: 90°

(e) Summed intensity,
Phase-angle: 120°

(f) Summed intensity,
Phase-angle: 150°

(g) Summed intensity,
Phase-angle: 180°

(h) Summed intensity,
Phase-angle: 210°

(i) Summed intensity,
Phase-angle: 240°

(j) Summed intensity,
Phase-angle: 270°

(k) Summed intensity,
Phase-angle: 300°

(l) Summed intensity,
Phase-angle: 330°

Figure 5.10: Images of the summed intensity over the Y-direction over the phase angles.

.
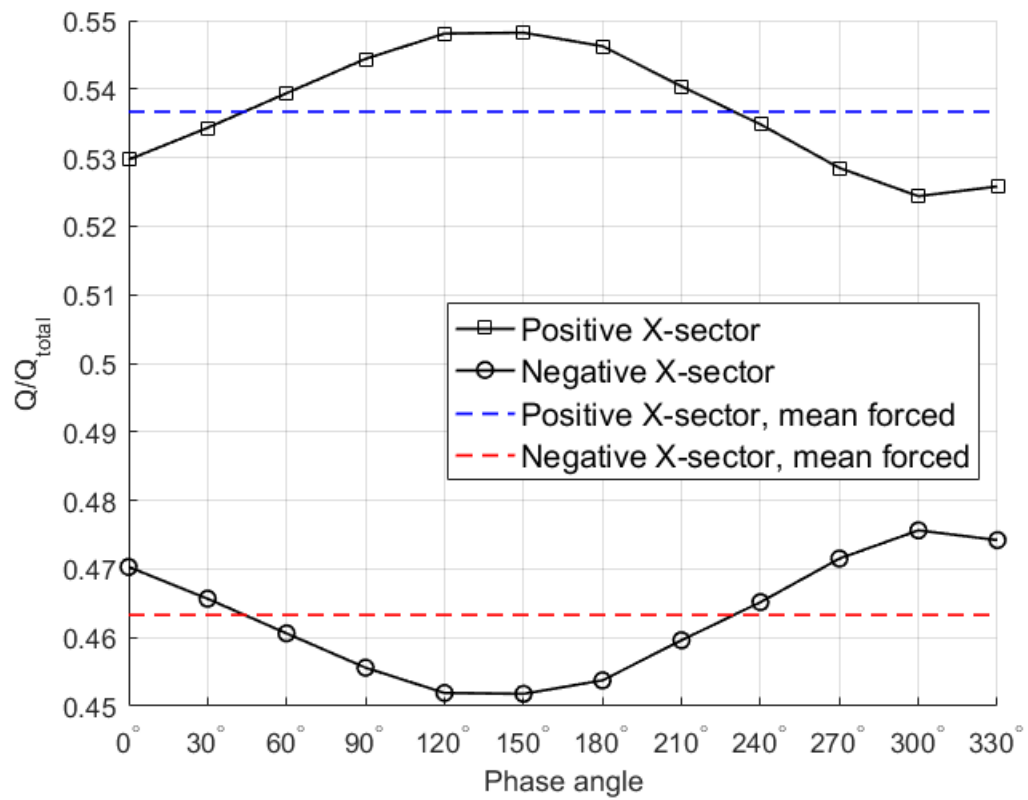
Figure 5.11: Heat release symmetry in XY-plane.

Chapter 6

Conclusion

6.1   Conclusion

Computed Tomography of OH* Chemiluminescence of a single flame confined by an annular combustion chamber have been performed. Azimuthal forcing was used to investigated the 3D modal dynamics of heat release for a mixed azimuthal mode with mean spin ratio, $SR = 0.26$.

An introduction to thermo-acoustic azimuthal instabilities and CTC were given in chapter 1, and recent research within both fields were presented and discussed. Further, a phantom study was performed. The methodology of the study was clarified in chapter 2. The framework producing the synthetic data, as well as camera calibrations procedures and the implementation of the tomographic reconstruction methods were explained.

A parametric phantom study was performed, and the results were presented and discussed in chapter 3. Investigations of an arc camera configurations used in the experimental setup showed that one of the most important parameters with regard to reconstruction quality was trying to maximize the viewing width β. With a sufficient number of camera views, N_c, increasing the views seemed to have little effect on the overall reconstruction quality. Also how calibration errors and reflections influenced reconstructions was examined, and the results showed as expected that the quality of reconstructions was prone to these types of error. However, there were indications of possibilities to minimize such errors by altering the iterations sequence of the camera views where errors were present.

Experimental methods were presented in chapter 4. A mock experiment investigating prob-

lems regarding re-positioning of calibration objects and refraction was used. For the Computed Tomography of OH* Chemiluminescence, an annular burner with acoustic forcing was utilized together with a high speed imaging system in order to capture experimental data used for the tomographic reconstructions. Both data for an unforced, and acoustically forced flame was acquired.

In chapter 5, the experimental results was presented, analyzed and discussed. Results from the mock experiment revealed strong influences on calibration accuracy due to refractive effects, and had to be considered in further experiments. Reconstructions of the mean heat release for the unforced flame revealed asymmetries believed to originate from inaccurate positioning of the bluff-body of the burner and limited view width. Analysis of the pressure series indicated a mean spin ratio of $SR = 0.26$, implicating that the forced azimuthal mode was a mixed mode, partly standing and partly ACW spinning. Reconstructions of the phase-averaged 3D heat release indicated large asymmetries believed to be caused by the ACW spinning component of the azimuthal mode. A complicated 3D flame dynamics for the acoustically forced flame was observed. Based on the azimuthal mode characterization, the complex flame dynamics is likely caused by the ACW spinning component of the azimuthal mode hitting the flame brush from the side. Also variations of the total heat release was observed to vary over the different phase-angles. The results demonstrates the possibility to investigate complex 3D unsteady periodic flows, utilizing only a single camera with an intensifier.

From the work presented here, the objectives presented in section 1.4 can be considered fulfilled. However, more work is required before CTC can be considered a viable option for investigation of azimuthal modes in annular combustion chambers. Suggestion for further work is presented in the next section.

6.2 Further Work

6.2.1 Validation

The first thing to consider regarding the results presented in this thesis is to validate them. It is suggested to validate the tomographic OH* chemiluminescence reconstructions by redoing

them together with a more well-established experimental methods used in combustion investigations and compare the results. A similar approach as used by Worth and Dawson (2013c) where volume slices of the tomographic reconstructed OH* chemiluminescence distribution were compared to OH-PLIF measurements is recommended.

If this was to be done, mistakes performed during the presented experiment should be avoided. During the initial run, the aperture setting of the camera lens was set to $f = 1/2.8$, which is the setting providing the least depth of field (DOF) for the images. For measurements like the CTC, it is desired to maximize the DOF in order to get the whole object of interest imaged as sharp as possible. The aperture setting should be set to a lower setting, and the intensifier gain could be increased in order to still get a strong signal. The pixel response of the intensifier should also be calibrated in order improve the accuracy of the experimental images captured (Weber et al., 2011).

At last, the unforced and forced experiments were performed separately, leading to the camera positions and calibrations not being identical for the two cases. Ideally should they be performed at the same time, meaning capturing both calibration images, forced and unforced flame data for each position. The comparison between the two results will be more credible doing the experiment this way.

6.2.2 Improve calibration method

To further improve the capabilities of the CTC applied to flames confined in an annular combustion chamber, better camera calibration procedures than the one used here must be developed. As explained earlier, the widest views of the flame had to be dropped due to high calibration errors. Wang et al. (2016) used 3D calibration objects and a modified camera calibration method to calibrate a pinhole model for an arc camera configuration with a view width close to 170°. Similar 3D calibration objects could be used in order to get more appropriate calibration points for the wide views of the current experimental setup. However, using a pinhole model for the camera models is not recommended due to the strong refraction introduced by the quartz enclosure.

Another possible solution to improve the camera calibrations is to use two calibration plate orientations. The suggested procedure for a similar setup as used in the experiment is illus-

trated in figure 6.1, and is performed by starting to acquiring data and calibration images for the red plate and views in the numbered sequence. For the 8th view, calibration images of the red orientation is first captured, then the plate is re-oriented as the blue plate rectangle indicates, and calibration images of the plate at this position are captured as well. The two set of calibration images captured for the 8th view are used to relate the orientation of the red and blue plate orientation. The blue plate orientation is then used for the rest of the views. This procedure will ensure that no views will have the problematic sharp angles that view 1 and 15 had for the original procedure. The re-orientation of the plate could be performed several more times if necessary.
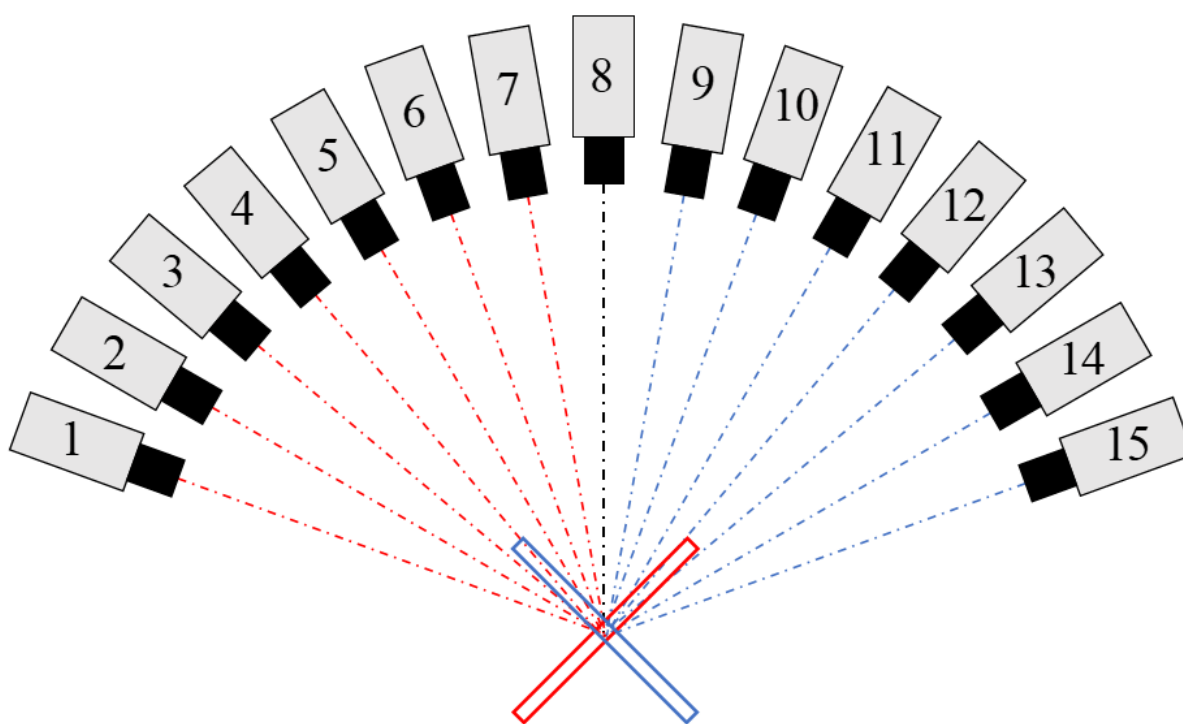
Figure 6.1: Illustration of new calibration procedure.

Another way to improve the calibration procedure is to relocate the calibration plate at the burner and capture a second set of calibration images for the current view before moving the camera to the next position. The two sets of calibration images captured for the single view can then be compared to evaluate how accurate the calibration plate was re-positioned between the two views.

6.2.3 Test the depth of field

As mentioned earlier, the depth of field of the imaging system is important when capturing images of a 3D object like the flame performed in this thesis. In order to further evaluate the quality of the experimental images, a method of estimating the depth of field could be used. Methods of estimating blurriness of an image can be used to evaluate the blurriness of images of a calibration plate moved through the volume of interest, where the focus of the camera lens is kept constant. The blurriness of the plate can then be mapped across the volume and used as an estimate of the depth of field. For this to be possible, a method of linearly move a calibration plate across the relevant volume of the burner is needed. Also, a suited blurriness estimation scheme must be found. Initial testing in the mock setup with the method presented by De and Masilamani (2013) showed promise, but was not included in the thesis due to lack of testing in the combustion experiment.

6.2.4 Alternative tomographic algorithms

Implementation of another tomographic reconstruction algorithm could be considered. The author suggests to implement and test the simultaneous multiplicative algebraic reconstruction technique (SMART) (Debasish Mishra, 1999) and simultaneous algebraic reconstruction technique (SART) (Andersen and Kak, 1984) in the phantom study. If they prove capable of providing accurate reconstructions, these algorithms are more fitted for parallelization in order to accelerate reconstruction times than the current utilized MART algorithm.

For these simultaneous algorithms, the sequence of the views would have no influence on the reconstruction quality since the voxel volume is updated only once in the end of the each iteration, based on all the views.

6.2.5 Parametric study of asymmetric phantom

The parametric study was performed using an axisymmetric phantom object. The acoustically forced flames showed a high degree of asymmetry, and in order to further determine the capabilities of the reconstruction program a parametric study using an asymmetric phantom object should be performed.

References

Andersen, A. and Kak, A. (1984). Simultaneous Algebraic Reconstruction Technique (SART): A superior implementation of the ART algorithm. *Ultrasonic Imaging*, 6(1):81–94.

Anikin, N., Suntz, R., and Bockhorn, H. (2010). Tomographic reconstruction of the OH*-chemiluminescence distribution in premixed and diffusion flames. *Applied Physics B*, 100(3):675–694.

Arthur H. Lefebvre, D. R. B. (2010). *Gas Turbine Combustion: Alternative Fuels and Emissions, Third Edition*. CRC, 3 edition.

Atkinson, C. and Soria, J. (2009). An efficient simultaneous reconstruction technique for tomographic particle image velocimetry. *Experiments in Fluids*, 47(4):553.

Balachandran, R., Ayoola, B., Kaminski, C., Dowling, A., and Mastorakos, E. (2005). Experimental investigation of the nonlinear response of turbulent premixed flames to imposed inlet velocity oscillations. *Combustion and Flame*, 143(1-2):37–55.

Best, P., Chien, P., Carangelo, R., Solomon, P., Danchak, M., and Ilovici, I. (1991). Tomographic reconstruction of FT-IR emission and transmission spectra in a sooting laminar diffusion flame: Species concentrations and temperatures. *Combustion and Flame*, 85(3-4):309–318.

Bourgouin, J.-F., Durox, D., Moeck, J. P., Schuller, T., and Candel, S. (2013). Self-Sustained Instabilities in an Annular Combustor Coupled by Azimuthal and Longitudinal Acoustic Modes. In *Volume 1B: Combustion, Fuels and Emissions*, page V01BT04A007. ASME.

Commons, W. (2005). Turbojet operation - axial flow.

Crocco, L. (1951). Aspects of Combustion Stability in Liquid Propellant Rocket Motors Part I: Fundamentals. Low Frequency Instability With Monopropellants. *Journal of the American Rocket Society*, 21(6):163–178.

Dawson, J. R. and Worth, N. A. (2014). Flame dynamics and unsteady heat release rate of self-excited azimuthal modes in an annular combustor. *Combustion and Flame*, 161(10):2565–2578.

Dawson, J. R. and Worth, N. A. (2015). The effect of baffles on self-excited azimuthal modes in an annular combustor. *Proceedings of the Combustion Institute*, 35(3):3283–3290.

De, K. and Masilamani, V. (2013). Image Sharpness Measure for Blurred Images in Frequency Domain. *Procedia Engineering*, 64:149–158.

Debasish Mishra, K. Muralidhar, P. M. (1999). A robust mart algorithm for tomographic applications. *Numerical Heat Transfer, Part B: Fundamentals*, 35(4):485–506.

Elsinga, G. E., Scarano, F., Wieneke, B., and van Oudheusden, B. W. (2006). Tomographic particle image velocimetry. *Experiments in Fluids*, 41(6):933–947.

Falkhytten, T. (2017). A Parametric Study of Tomographic Reconstruction Utilizing an Accelerated MART program.

Floyd, J., Geipel, P., and Kempf, A. (2011). Computed tomography of chemiluminescence (ctc): Instantaneous 3d measurements and phantom studies of a turbulent opposed jet flame. *Combustion and Flame*, 158(2):376 – 391.

Floyd, J. and Kempf, A. (2011). Computed Tomography of Chemiluminescence (CTC): High resolution and instantaneous 3-D measurements of a Matrix burner. *Proceedings of the Combustion Institute*, 33(1):751–758.

Ghirardo, G. and Juniper, M. P. (2013). Azimuthal instabilities in annular combustors: standing and spinning modes. *Proceedings of the Royal Society A: Mathematical, Physical and Engineering Sciences*, 469(2157):20130232–20130232.

Ghosh, G. (1999). Dispersion-equation coefficients for the refractive index and birefringence of calcite and quartz crystals. *Optics Communications*, 163(1-3):95–102.

Gordon, R., Bender, R., and Herman, G. T. (1970). Algebraic reconstruction techniques (art) for three-dimensional electron microscopy and x-ray photography. *Journal of Theoretical Biology*, 29(3):471 – 481.

Häfeli, R., Altheimer, M., Butscher, D., and Rudolf von Rohr, P. (2014). PIV study of flow through porous structure using refractive index matching. *Experiments in Fluids*, 55(5):1717.

Herman, G. T. and Lent, A. (1976). Iterative reconstruction algorithms. *Computers in Biology and Medicine*, 6(4):273 – 294. Advances in Picture Reconstruction;Theory and Applications.

Im, S., Heo, G. E., Jeon, Y. J., Sung, H. J., and Kim, S. K. (2014). Tomographic PIV measurements of flow patterns in a nasal cavity with geometry acquisition. *Experiments in Fluids*, 55(1):1644.

Ishino, Y., Hayashi, N., Bt Abd Razak, I. F., Kato, T., Kurimoto, Y., and Saiki, Y. (2016). 3D-CT(Computer Tomography) Measurement of an Instantaneous Density Distribution of Turbulent Flames with a Multi-Directional Quantitative Schlieren Camera (Reconstructions of High-Speed Premixed Burner Flames with Different Flow Velocities). *Flow, Turbulence and Combustion*, 96(3):819–835.

Ishino, Y. and Ohiwa, N. (2005). Three-Dimensional Computerized Tomographic Reconstruction of Instantaneous Distribution of Chemiluminescence of a Turbulent Premixed Flame. *JSME International Journal Series B*, 48(1):34–40.

Ishino, Y., Takeuchi, K., Shiga, S., and Ohiwa, N. (2009). Measurement of Instantaneous 3D-Distribution of Local Burning Velocity on a Turbulent Flame By Non-Scanning 3D-Ct Reconstruction With Flame-Tracking 40-Lens Camera. *Image (Rochester, N.Y.)*, page 40.

Kasim, M. F., Holloway, J., Ceurvorst, L., Levy, M. C., Ratan, N., Sadler, J., Bingham, R., Burrows, P. N., Trines, R., Wing, M., and Norreys, P. (2015). Quantitative single shot and spatially resolved plasma wakefield diagnostics. *Physical Review Special Topics - Accelerators and Beams*, 18(8):081302.

Krebs, W., Flohr, P., Prade, B., and Hoffmann, S. (2002). Combustion Science and Technology THERMOACOUSTIC STABILITY CHART FOR HIGH- INTENSITY GAS TURBINE COMBUS-TION SYSTEMS THERMOACOUSTIC STABILITY CHART FOR HIGH-INTENSITY GAS TUR-BINE COMBUSTION SYSTEMS. *Combust. Sci. andTech*, 174(7):9–128.

MathWorks. robustfit. https://se.mathworks.com/help/stats/robustfit.html. accessed April 5, 2018.

Mazur, M., Nygård, H. T., Dawson, J. R., and Worth, N. A. (2018). Characteristics of self-excited spinning azimuthal modes in an annular combustor with turbulent premixed blu ff -body flames. *Submitted.*

McNesby, K. L., Daniel, R. G., Morris, J. B., and Miziolek, A. W. (1995). Tomographic analysis of CO absorption in a low-pressure flame. *Applied Optics*, 34(18):3318.

Nau, P., Krüger, J., Lackner, A., Letzgus, M., and Brockhinke, A. (2012). On the quantification of OH*, CH*, and C2* chemiluminescence in flames. *Applied Physics B*, 107(3):551–559.

Nygård, H. T., Mazur, M., Dawson, J. R., and Worth, N. A. (2018). Flame dynamics of azimuthal forced spinning and standing modes in an annular combustor. *In press.*

Oefelein, J. C. and Yang, V. (1993). Comprehensive Review of Liquid-Propellant Combustion Instabilities in F-l Engines. *JOURNAL OF PROPULSION AND POWER*, 9(5).

Palies, P., Durox, D., Schuller, T., and Candel, S. (2010). The combined dynamics of swirler and turbulent premixed swirling flames. *Combustion and Flame*, 157(9):1698–1717.

Poinsot, T. (2017). Prediction and control of combustion instabilities in real engines. *Proceedings of the Combustion Institute*, 36(1):1–28.

Prasad, A. K. (2000). Stereoscopic particle image velocimetry. *Experiments in Fluids*, 29(2):103–116.

Putnam, A. A. A. A. (1971). *Combustion-driven oscillations in industry*. American Elsevier Pub. Co.

Rayleigh (1878). The explanation of certain acoustical phenomena. *Nature*, 18:319–321.

Samarasinghe, J., Peluso, S., Szedlmayer, M., De Rosa, A., Quay, B., and Santavicca, D. (2013). Three-Dimensional Chemiluminescence Imaging of Unforced and Forced Swirl-Stabilized Flames in a Lean Premixed Multi-Nozzle Can Combustor. *Journal of Engineering for Gas Turbines and Power*, 135(10):101503.

Samarasinghe, J., Peluso, S. J., Quay, B. D., and Santavicca, D. A. (2015). The Three-Dimensional Structure of Swirl-Stabilized Flames in a Lean Premixed Multinozzle Can Combustor. *Journal of Engineering for Gas Turbines and Power*, 138(3):031502.

Saravanamuttoo, H. I. H., Rogers, G. F. C., Cohen, H., and Straznicky, P. V. (2009). *Gas Turbine Theory*. Pearson Prentice Hall, Harlow, England; New York, 6 edition.

Scarano, F. (2013). Tomographic piv: principles and practice. *Measurement Science and Technology*, 24(1):012001.

Seybert, A. F. and Ross, D. F. (1977). Experimental determination of acoustic properties using a two-microphone random-excitation technique. *The Journal of the Acoustical Society of America*, 61(5):1362–1370.

Soloff, S. M., Adrian, R. J., and Liu, Z.-C. (1997). Distortion compensation for generalized stereoscopic particle image velocimetry. *Measurement Science and Technology*, 8(12):1441.

Staffelbach, G., Gicquel, L., Boudier, G., and Poinsot, T. (2009). Large Eddy Simulation of self excited azimuthal modes in annular combustors. *Proceedings of the Combustion Institute*, 32(2):2909–2916.

Sturm, P. (2014). *Pinhole Camera Model*, pages 610–613. Springer US, Boston, MA.

Upton, T. D., Verhoeven, D. D., and Hudgins, D. E. (2011). High-resolution computed tomography of a turbulent reacting flow. *Experiments in Fluids*, 50(1):125–134.

Wang, J., Zhang, W., Zhang, Y., and Yu, X. (2016). Camera calibration for multidirectional flame chemiluminescence tomography. *Optical Engineering*, 56(4):041307.

Weber, V., Brübach, J., Gordon, R. L., and Dreizler, A. (2011). Pixel-based characterisation of CMOS high-speed camera systems. *Applied Physics B*, 103(2):421–433.

Wiseman, S. M., Brear, M. J., Gordon, R. L., and Marusic, I. (2017). Measurements from flame chemiluminescence tomography of forced laminar premixed propane flames. *Combustion and Flame*, 183:1–14.

Wolf, P., Staffelbach, G., Gicquel, L. Y., Müller, J.-D., and Poinsot, T. (2012). Acoustic and Large Eddy Simulation studies of azimuthal modes in annular combustion chambers. *Combustion and Flame*, 159(11):3398–3413.

Worth, N. A. and Dawson, J. R. (2013a). Modal dynamics of self-excited azimuthal instabilities in an annular combustion chamber. *Combustion and Flame*, 160(11):2476–2489.

Worth, N. A. and Dawson, J. R. (2013b). Self-excited circumferential instabilities in a model annular gas turbine combustor: Global flame dynamics.

Worth, N. A. and Dawson, J. R. (2013c). Tomographic reconstruction of OH* chemiluminescence in two interacting turbulent flames. *Measurement Science and Technology*, 24(2).

Worth, N. A. and Dawson, J. R. (2017). Effect of equivalence ratio on the modal dynamics of azimuthal combustion instabilities. *Proceedings of the Combustion Institute*, 36(3):3743–3751.

Worth, N. A., Dawson, J. R., Sidey, J. A., and Mastorakos, E. (2017). Azimuthally forced flames in an annular combustor. *Proceedings of the Combustion Institute*, 36(3):3783–3790.

Worth, N. A. and Nickels, T. B. (2008). Acceleration of tomo-piv by estimating the initial volume intensity distribution. *Experiments in Fluids*, 45(5):847.

Y. Tsai, R. (1987). Tsai, r.y.: A versatile camera calibration technique for high-accuracy 3d machine vision metrology using off-the-shelf tv cameras and lenses. ieee journal of robotics and automation 3, 323-344. 3:323 – 344.

Young, M. (1971). Pinhole optics. *Appl. Opt.*, 10(12):2763–2767.

Yu, T., Liu, H., and Cai, W. (2017). On the quantification of spatial resolution for three-dimensional computed tomography of chemiluminescence. *Optics Express*, 25(20):24093.

NTNU

SINTEF

Risk Assessment Report

Annular Combustor

Prosjektnavn	Combustion Instabilities in Annular Combustors
Apparatur	Annular Combustor
Enhet	NTNU
Apparaturansvarlig	Nicholas Worth
Prosjektleder	Nicholas Worth
HMS-koordinator	Morten Grønli
HMS-ansvarlig (linjeleder)	Olav Bolland
Plassering	Combustion Laboratory
Romnummer	C084
Risikovurdering utført av	Håkon Tormodsen Nygård, Nicholas Worth

Approval:

Apparatur kort (UNIT CARD) valid for:	12 months
Forsøk pågår kort (EXPERIMENT IN PROGRESS) valid for:	12 months

Rolle	Navn	Dato	Signatur
Prosjektleder	Nicholas Worth		
HMS koordinator	Morten Grønli		
HMS ansvarlig (linjeleder)	Olav Bolland		

TABLE OF CONTENTS

1   INTRODUCTION

The aim of the project is to improve our fundamental understanding of the system response and the combustion dynamics of both self-excited instabilities and forced oscillations in annular combustors. The aim is to use the knowledge to understand and predict thermoacoustic instabilities in low emission aeroengines and power generating gas turbines.

The rig is located in the basement of Varmeteknisk Laboratorium (VATL).

2   ORGANISATION

Rolle	
Prosjektleder	Nicholas Worth
Apparaturansvarlig	Nicholas Worth
Romansvarlig	Martin Bustadmo
HMS koordinator	Morten Grønli
HMS ansvarlig (linjeleder):	Olav Bolland

3   RISK MANAGEMENT IN THE PROJECT

Main Activities Risk	Necessary measures, documentation	DATE
Project initiation	Project initiation template	
Guidance Meeting	Form for Guidance Meeting with pre - risk assessment	
Initial Assessment	Hazard identification – HAZID Form rough analysis	
Evaluation of technical security	Process HAZOP Technical documentations	
Evaluation of operational safety	Procedure - HAZOP Training plan for operators	
Final assessment, quality assurance	Independent control Issuance of apparatus card Issuance of trials taking short	

4   DESCRIPTIONS OF EXPERIMENTAL SETUP

This experimental setup is used to study both self-excited instabilities and forced oscillations in an annular combustor. The setup used is detailed below.
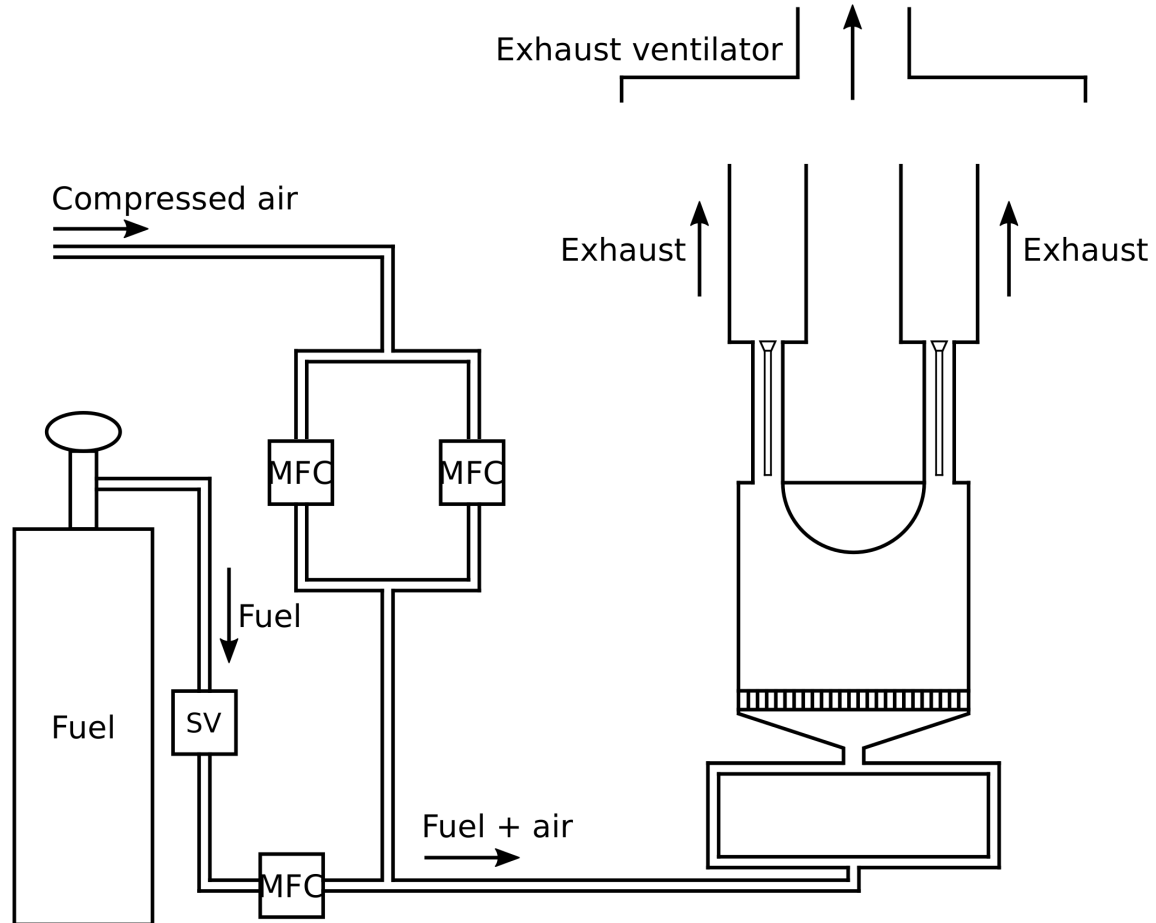
Figure 1: Schematic drawing of the experimental setup. In the figure the box marked SV is the solenoid valve and the boxes marked MFC is mass flow controllers. Only two burners are shown, but the rig has between 12 and 18 burners depending on the configuration.

Fuel is delivered from a gas cylinder with a solenoid shutoff valve fitted in the fuel delivery line. Alicat mass flow controllers are used to independently control the flow of fuel and air. The fuel-air feeds are premixed prior to entering the burners. The number of individual burners can be varied between 12 and 18. A gas torch or a low voltage glow plug is used to ignite the premixed fuel-air mixture. The burners are securely positioned below a ceiling extractor which vents the exhaust gases from the laboratory room. A CO alarm is also present in the room to ensure safe CO levels are maintained.

5   EVACUATION FROM THE EXPERIMENTAL AREA

Evacuate at signal from the alarm system or local gas alarms with its own local alert with sound and light outside the room in question, see 6.2

Evacuation from the rigging area takes place through the marked emergency exits to the assembly point, (corner of Old Chemistry Kjelhuset or parking 1a-b.)

Action on rig before evacuation:
Press the emergency shut-down push button. Leave the air supply on.

6   WARNING

6.1   Before experiments

Send an e-mail with information about the planned experiment to:
iept-experiments@ivt.ntnu.no

The e-mail must include the following information:
- Name of responsible person:
- Experimental setup/rig:
- Start Experiments: (date and time)
- Stop Experiments: (date and time)

You must get the approval back from the laboratory management before start up. All running experiments are notified in the activity calendar for the lab to be sure they are coordinated with other activity.

6.2   Abnormal situation

<u>FIRE</u>
If you are NOT able to extinguish the fire, activate the nearest fire alarm and evacuate area.
Be then available for fire brigade and building caretaker to detect fire place.
If possible, notify:

NTNU	SINTEF
Morten Grønli, Mob: 918 97 515	Linda Helander, Mob 406 48 621
Olav Bolland: Mob: 918 97 209	Petter Røkke, Mob: 901 20 221
NTNU – SINTEF Beredskapstelefon	800 80 388

<u>GAS ALARM</u>
If a gas alarm occurs, close gas bottles immediately and ventilate the area. If the level of the gas concentration does not decrease within a reasonable time, activate the fire alarm and evacuate the lab. Designated personnel or fire department checks the leak to determine whether it is possible to seal the leak and ventilate the area in a responsible manner.

Alert Order is in the above paragraph.

<u>PERSONAL INJURY</u>
- First aid kit in the fire / first aid stations
- Shout for help
- Start life-saving first aid
- **CALL 113** if there is any doubt whether there is a serious injury

OTHER ABNORMAL SITUATIONS

NTNU:
You will find the reporting form for non-conformance on:
https://innsida.ntnu.no/wiki/-/wiki/Norsk/Melde+avvik

SINTEF:
Synergi

7 ASSESSMENT OF TECHNICAL SAFETY

7.1 HAZOP

See Chapter 13 "Guide to the report template".
The experiment set up is divided into the following nodes:

Node 1	Annular Combustor (Main test rig)

Attachments, Form: Hazop_mal
Conclusion: (Safety taken care of)

7.2 Flammable, reactive and pressurized substances and gas

Are any flammable, reactive and pressurized substances and gases in use?

YES	Explosion document has to be made and/or documented pressure test, (See 8.3)

Attachments: Description of the ATEX diagram of the test rig
Conclusion:

7.3 Pressurized equipment

Is any pressurized equipment in use?

YES	The equipment has to undergo pressure testes in accordance with the norms and be documented

Attachments: Certificate for pressurized equipment (see Attachment to Risk Assessment)
Conclusion:

7.4 Effects on the environment (emissions, noise, temperature, vibration, smell)

Will the experiments generate emission of smoke, gas, odour or unusual waste?
Is there a need for a discharge permit, extraordinary measures?

YES	Experiments generate hot exhaust gases and smoke resulting from complete or incomplete combustion process. The smoke will be permanently ventilated through the exhaust ventilator. The operator is responsible for activating the exhaust ventilator before experiments (see the start-up procedure).

Attachments:

Conclusion: No need for special permits or extraordinary measures. The operator should always ensure the exhaust ventilator is on whenever the rig is run in hot conditions and follow the operating guidelines.

7.5 Radiation

See Chapter 13 "Guide to the report template".

NO	

Attachments:
Conclusion:

7.6 Chemicals

YES	Do a risk assessment of the use

Attachments: MSDS of Methane and Ethylene
Conclusion: When working with methane or ethylene the exhaust ventilator should be active and persons in the room has to wear the recommended protective equipment. The two most important risks connected with the use of methane and ethylene is the asphyxiation danger and fire hazard in case of an undetected leakage. The ventilator will minimize the risk of this happening. Further lowering the risk is the fact that the test rig will be checked for leaks on a regular basis. Neither methane nor ethylene is corrosive, and there is no danger related to contact with skin as long as it is not in liquid form, which it will not be in this case.

7.7 Electricity safety (deviations from the norms/standards)

YES	Electricity safety has to be assessed. A glow plug (24 V) will be used to ignite the combustible fuel-air mixture.

Attachments:
Conclusion: All AC equipment used when working on the rig will be installed by trained personnel, and should therefore follow the norm and standards required. The glow plug will use 24 V DC which does not pose any danger of electric shocks causing harm to the operator. The operator should however be aware that the glow plug gets hot when it is powered on, and will pose a scald hazard if touched.

8 ASSESSMENT OF OPERATIONAL SAFETY

Ensure that the procedures cover all identified risk factors that must be taken care of. Ensure that the operators and technical performance have sufficient expertise.

8.1 Procedure HAZOP

See Chapter 13 "Guide to the report template".
The method is a procedure to identify causes and sources of danger to operational problems.

Attachments:: HAZOP_MAL_Prosedyre

8.2 Operation procedure and emergency shutdown procedure

The operating procedure is a checklist that must be filled out for each experiment.
 Emergency procedure should attempt to set the experiment set up in a harmless state by unforeseen events.

Attachments: Procedure for running experiments
Emergency shutdown procedure:
Press the emergency shut-down push button. Leave air supply on.

8.3 Training of operators

A Document showing training plan for operators
* What are the requirements for the training of operators?
* What it takes to be an independent operator
* Job Description for operators

 Attachments*:* Training program for operators

8.4 Technical modifications

* Technical modifications made by the operator (e.g.Replacement of components, equal to equal)
* Technical modifications that must be made by Technical staff (for example, modification of pressure equipment).
* What technical modifications give a need for a new risk assessment (by changing the risk picture)?

Conclusion:

8.5 Personal protective equipment

* It is mandatory use of eye protection in the rig zone
* It is mandatory use of ear protection in the rig zone when the noise level is high
* Use gloves when there is opportunity for contact with hot/cold surfaces

Conclusion:

8.6 General Safety

* The area around the staging attempts shielded.
* Gas cylinders shall be placed in an approved carrier with shut-off valve within easy reach.
* Experiment cannot be run unattended

8.7 Safety equipment

* There are permanently installed gas detectors in the laboratory room
* Warning signs, see the Regulations on Safety signs and signalling in the workplace

8.8 Special predations

- *No further*

9 QUANTIFYING OF RISK - RISK MATRIX

See Chapter 13 "Guide to the report template".

The risk matrix will provide visualization and an overview of activity risks so that management and users get the most complete picture of risk factors.

IDnr	Aktivitet-hendelse	Frekv-Sans	Kons	RV
	Scald hazard	2	B2	B2
	Unwanted fire when igniting fuel-air mixture	2	B2	B2
	Flame flashback	2	B2	B2
	Shock by electrical equipment	1	A1	A1
	Pressurized air system	1	B1	B1
	Asphyxiation/oxygen deprivation	1	E1	E1
	Explosive atmosphere due to gas leakage	1	E1	E1

Conclusion: The risks linked to fire when igniting the combustible fuel-air mixture, flashback, shock by electrical equipment and risks connected to the pressurized air system represent an acceptable level of risk. Care should be taken to follow the operating procedures, and there should be no danger of serious injuries. The risks due to gas leakage, which is possible asphyxiation or explosive atmosphere, has to be given an assessment due to the major consequences. Both cases involve a considerable amount of gas in the laboratory room, either due to a major leakage or an undetected smaller leakage. The risk is minimized by using approved equipment and no leakage will occur under normal operating conditions. There will be regular leak checks of the rig, and the operator will ensure no spark sources are located close to the rig. These safety measures and procedures will ensure the risk is within acceptable levels.

CONSEQUENSES						
	Catastrophic	E1	E2	E3	E4	E5
	Major	D1	D2	D3	D4	D5
	Moderate	C1	C2	C3	C4	C5
	Minor	B1	B2	B3	B4	B5
	Insignificant	A1	A2	A3	A4	A5
		Rare	Unlikely	Possible	Likely	Almost
		PROBABILITY				

Table 8. Risk's Matrix

COLOUR	DESCRIPTION

Red		Unacceptable risk Action has to be taken to reduce risk
Yellow		Assessment area. Actions has to be considered
Green		Acceptable risk. Action can be taken based on other criteria

Table 9. The principle of the acceptance criterion. Explanation of the colors used in the matrix

10 REGULATIONS AND GUIDELINES

Se http://www.arbeidstilsynet.no/regelverk/index.html
- Lov om tilsyn med elektriske anlegg og elektrisk utstyr (1929)
- Arbeidsmiljøloven
- Forskrift om systematisk helse-, miljø- og sikkerhetsarbeid (HMS Internkontrollforskrift)
- Forskrift om sikkerhet ved arbeid og drift av elektriske anlegg (FSE 2006)
- Forskrift om elektriske forsyningsanlegg (FEF 2006)
- Forskrift om utstyr og sikkerhetssystem til bruk i eksplosjonsfarlig område NEK 420
- Forskrift om håndtering av brannfarlig, reaksjonsfarlig og trykksatt stoff samt utstyr og anlegg som benyttes ved håndteringen
- Forskrift om Håndtering av eksplosjonsfarlig stoff
- Forskrift om bruk av arbeidsutstyr.
- Forskrift om Arbeidsplasser og arbeidslokaler
- Forskrift om Bruk av personlig verneutstyr på arbeidsplassen
- Forskrift om Helse og sikkerhet i eksplosjonsfarlige atmosfærer
- Forskrift om Høytrykksspyling
- Forskrift om Maskiner
- Forskrift om Sikkerhetsskilting og signalgivning på arbeidsplassen
- Forskrift om Stillaser, stiger og arbeid på tak m.m.
- Forskrift om Sveising, termisk skjæring, termisk sprøyting, kullbuemeisling, lodding og sliping (varmt arbeid)
- Forskrift om Tekniske innretninger
- Forskrift om Tungt og ensformig arbeid
- Forskrift om Vern mot eksponering for kjemikalier på arbeidsplassen (Kjemikalieforskriften)
- Forskrift om Vern mot kunstig optisk stråling på arbeidsplassen
- Forskrift om Vern mot mekaniske vibrasjoner
- Forskrift om Vern mot støy på arbeidsplassen

Veiledninger fra arbeidstilsynet
se: http://www.arbeidstilsynet.no/regelverk/veiledninger.html

11 DOCUMENTATION

- Tegninger, foto, beskrivelser av forsøksoppsetningen
- Hazop_mal
- Sertifikat for trykkpåkjent utstyr
- Håndtering avfall i NTNU
- Sikker bruk av LASERE, retningslinje
- HAZOP_MAL_Prosedyre
- Forsøksprosedyre
- Opplæringsplan for operatører
- Skjema for sikker jobb analyse, (SJA)
- Apparaturkortet
- Forsøk pågår kort

12 GUIDANCE TO RISK ASSESSMENT TEMPLATE

Chapter 7 Assessment of technical safety.

Ensure that the design of the experiment set up is optimized in terms of technical safety.
Identifying risk factors related to the selected design, and possibly to initiate re-design to ensure that risk is eliminated as much as possible through technical security.

This should describe what the experimental setup actually are able to manage and acceptance for emission.

7.1 HAZOP

The experimental set up is divided into nodes (eg motor unit, pump unit, cooling unit.). By using guidewords to identify causes, consequences and safeguards, recommendations and conclusions are made according to if necessary safety is obtained. When actions are performed the HAZOP is completed.

(e.g. "No flow", cause: the pipe is deformed, consequence: pump runs hot, precaution: measurement of flow with a link to the emergency or if the consequence is not critical used manual monitoring and are written into the operational procedure.)

7.2 Flammable, reactive and pressurized substances and gas.

According to the Regulations for handling of flammable, reactive and pressurized substances and equipment and facilities used for this:

Flammable material: Solid, liquid or gaseous substance, preparation, and substance with occurrence or combination of these conditions, by its flash point, contact with other substances, pressure, temperature or other chemical properties represent a danger of fire.
Reactive substances: Solid, liquid, or gaseous substances, preparations and substances that occur in combinations of these conditions, which on contact with water, by its pressure, temperature or chemical conditions, represents a potentially dangerous reaction, explosion or release of hazardous gas, steam, dust or fog.
Pressurized : Other solid, liquid or gaseous substance or mixes having fire or hazardous material response, when under pressure, and thus may represent a risk of uncontrolled emissions

Further criteria for the classification of flammable, reactive and pressurized substances are set out in Annex 1 of the Guide to the Regulations "Flammable, reactive and pressurized substances"

http://www.dsb.no/Global/Publikasjoner/2009/Veiledning/Generell%20veiledning.pdf
http://www.dsb.no/Global/Publikasjoner/2010/Tema/Temaveiledning_bruk_av_farlig_stoff_Del_1.pdf

Experiment setup area should be reviewed with respect to the assessment of Ex zone
• Zone 0: Always explosive atmosphere, such as inside the tank with gas, flammable liquid.
• Zone 1: Primary zone, sometimes explosive atmosphere such as a complete drain point
• Zone 2: secondary discharge could cause an explosive atmosphere by accident, such as flanges, valves and connection points

7.4 Effects on the environment

With pollution means: bringing solids, liquid or gas to air, water or ground, noise and vibrations, influence of temperature that may cause damage or inconvenience effect to the environment.

Regulations: http://www.lovdata.no/all/hl-19810313-006.html#6

NTNU guidance to handling of waste:http://www.ntnu.no/hms/retningslinjer/HMSR18B.pdf

7.5 Radiation

Definition of radiation

Ionizing radiation: Electromagnetic radiation (in radiation issues with wawelength <100 nm) or rapid atomic particles (e.g. alpha and beta particles) with the ability to stream ionized atoms or molecules.
Non ionizing radiation: Electromagnetic radiation (wavelength >100 nm), og ultrasound$_1$ with small or no capability to ionize.
Radiation sources: All ionizing and powerful non-ionizing radiation sources.
Ionizing radiation sources: Sources giving ionizing radiation e.g. all types of radiation sources, x-ray, and electron microscopes.
Powerful non ionizing radiation sources: Sources giving powerful non ionizing radiation which can harm health and/or environment, e.g. class 3B and 4. MR$_2$ systems, UVC$_3$ sources, powerful IR sources$_4$.
$_1$Ultrasound is an acoustic radiation ("sound") over the audible frequency range (> 20 kHz). In radiation protection regulations are referred to ultrasound with electromagnetic non-ionizing radiation. $_2$MR (e.g. NMR) - nuclear magnetic resonance method that is used to "depict" inner structures of different materials. $_3$UVC is electromagnetic radiation in the wavelength range 100-280 nm. $_4$IR is electromagnetic radiation in the wavelength range 700 nm - 1 mm.

For each laser there should be an information binder (HMSRV3404B) which shall include:
- General information
- Name of the instrument manager, deputy, and local radiation protection coordinator
- Key data on the apparatus
- Instrument-specific documentation
- References to (or copies of) data sheets, radiation protection regulations, etc.
- Assessments of risk factors
- Instructions for users
- Instructions for practical use, startup, operation, shutdown, safety precautions, logging, locking, or use of radiation sensor, etc.
- Emergency procedures
- See NTNU for laser: http://www.ntnu.no/hms/retningslinjer/HMSR34B.pdf

7.6 The use and handling of chemicals.

In the meaning chemicals, a element that can pose a danger to employee safety and health

See: http://www.lovdata.no/cgi-wift/ldles?doc=/sf/sf/sf-20010430-0443.html

Safety datasheet is to be kept in the HSE binder for the experiment set up and registered in the database for chemicals.

Chapter 8 Assessment of operational procedures.

Ensures that established procedures meet all identified risk factors that must be taken care of through operational barriers and that the operators and technical performance have sufficient expertise.

8.1 Procedure Hazop
Procedural HAZOP is a systematic review of the current procedure, using the fixed HAZOP methodology and defined guidewords. The procedure is broken into individual operations (nodes) and analyzed using guidewords to identify possible nonconformity, confusion or sources of inadequate performance and failure.

8.2 Procedure for running experiments and emergency shutdown.
Have to be prepared for all experiment setups.
The operating procedure has to describe stepwise preparation, startup, during and ending conditions of an experiment. The procedure should describe the assumptions and conditions for starting, operating parameters with the deviation allowed before aborting the experiment and the condition of the rig to be abandoned.
Emergency procedure describes how an emergency shutdown have to be done, (conducted by the uninitiated),
what happens when emergency shutdown, is activated. (electricity / gas supply) and
which events will activate the emergency shutdown (fire, leakage).

Chapter 9 Quantifying of RISK
Quantifying of the residue hazards, Risk matrix
To illustrate the overall risk, compared to the risk assessment, each activity is plotted with values for the probability and consequence into the matrix. Use task IDnr.
Example: If activity IDnr. 1 has been given a probability 3 and D for consequence the risk value become D3, red. This is done for all activities giving them risk values.
In the matrix are different degrees of risk highlighted in red, yellow or green. When an activity ends up on a red risk (= unacceptable risk), risk reducing action has to be taken

Attachment to Risk Assessment report

Annular Combustor

Prosjektnavn	Combustion Instabilities in Annular Combustors
Apparatur	Annular Combustor
Enhet	NTNU
Apparaturansvarlig	Nicholas Worth
Prosjektleder	Nicholas Worth
HMS-koordinator	Morten Grønli
HMS-ansvarlig (linjeleder)	Olav Bolland
Plassering	Combustion Laboratory
Romnummer	C084
Risikovurdering utført av	Håkon Tormodsen Nygård, Nicholas Worth

TABLE OF CONTENTS

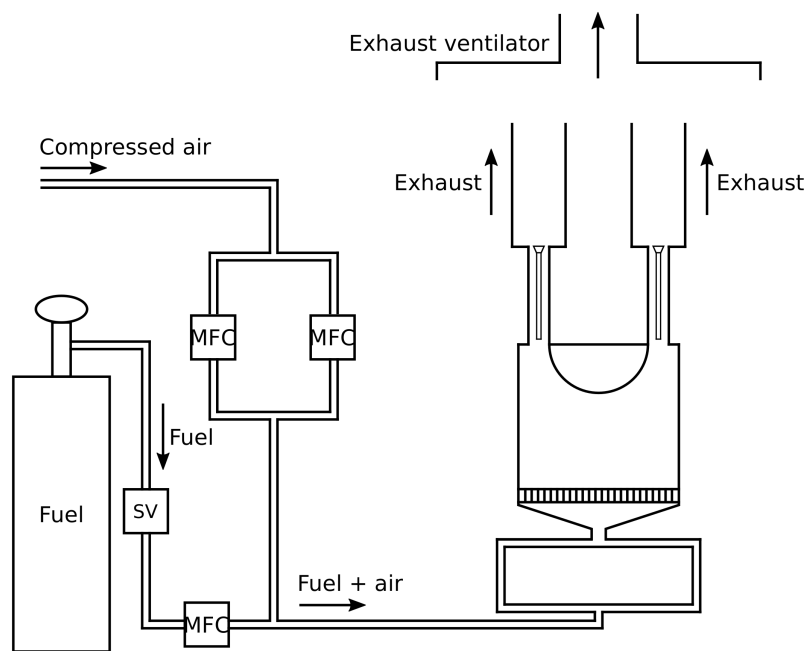**ATTACHMENT A: PROCESS AND INSTRUMENTATION DIAGRAM**

Figure 1: The figure shows a schematic drawing of the test rig with two burners visible. The number of burners can be varied from 12 to 18. SV is the solenoid valve and MFC is the mass flow controllers

ATTACHMENT B: HAZOP TEMPLATE

Project: Combustion Instabilities in Annular Combustors Node: 1 Annular Combustor (Main test rig)					Page	
Ref	Guideword	Causes	Consequences	Safeguards	Recommendations	Action	Date/Sign
1	No flow	- No air pressure - No ethylene pressure - Mass flow meters closed - Solenoid valve closed - Blockage or large leak somewhere in the rig	- Cannot carry out experiments - Wrong mixing ratio - Gas leakage if leakage in the rig - Flame flashback if the air volume flow is too low	- Gas detectors in the room - Good ventilation with dedicated exhaust fan - Check for leaks each time the rig is used - All equipment where pressure can build up is certified for pressure significantly higher than typical working pressures	- Monitor flow rates - Check mass flow meters are working properly - Regular leak checks - Check mass flow controllers	- Repair flow meter or solenoid valve if it is causing the problem - Repair leak if present	
2	Reverse flow	NA					
3	More flow	- Mass flow controller is not working properly	- Incorrect mass flow - Possible change in gas mixture	- No problem if too much air flow - Solenoid emergency switch for fuel supply	- Check mass flow controllers for abnormal behaviour?	- Repair or replace mass flow controllers	
4	Less flow	Ref. 1	- Danger of flashback (see ref.				

Project: Combustion Instabilities in Annular Combustors Node: 1 Annular Combustor (Main test rig)						Page	
Ref	Guideword	Causes	Consequences	Safeguards	Recommendations	Action	Date/Sign
			1)				
5	More level	NA					
6	Less level	NA					
7	More pressure	Ref. 3 - Can also be caused by blockage in the system (see Ref. 1)					
8	Less pressure	Ref. 1					
9	More temperature	- Low or zero air flow - Flame flashback - Fire of the flow conditioner inside the combustor	- Microphones may be damaged - Speakers may be damaged in extreme cases	- Rig is made out of stainless steel, which can withstand high temperatures - Microphones and speakers are replaceable	- Check air mass flow - Be extra alert of internal fire if flashback has occurred	- Wait until rig has cooled down and repair or replace damaged electronics, if any	
10	Less temperature	NA					
11	More viscosity	NA					
12	Less viscosity	NA					
13	Composition Change	- Malfunctioning mass flow controllers - Run out of fuel	- Not the right combustion conditions - Possible flame flashback if low air flow rate	- Emergency solenoid switch for fuel supply	- Check air pressure - Listen for changes in sound and do external visual checks of the combustion process	- Repair or replace mass flow controller - Get more fuel	
14	Contamination	NA					
15	Relief	NA					

	Project: Combustion Instabilities in Annular Combustors					Page	
	Node: 1 Annular Combustor (Main test rig)						
Ref	Guideword	Causes	Consequences	Safeguards	Recommendations	Action	Date/Sign
16	Instrumentation	- No power to instrumentation - Defective instrumentation	- Cannot get data - No fuel flow if the solenoid valve has no power	- No problem if it happens, so no particular safeguards	- Check if all of the required power cords are connected - Check if equipment is damaged	- Plug in power cords if equipment seems fine - Change/repair damaged equipment	
17	Sampling	NA					
18	Corrosion/erosion	NA					
19	Service failure	- No pressure in the central air system in the building - Power outage for the laboratory	- Possible flash back if there is a decrease in air flow		- Check messages and mail for information about routine power shutdowns and shutdown of the central pressurised air system		
20	Abnormal Operation	Se all other references					
21	Maintenance	- Malfunctioning mass flow controllers	- Possible flame flashback if air flow rate is reduced - Cannot conduct experiment	- Mass flow controllers are sent back to the manufacturer for maintenance at recommended intervals	- Send mass flow controllers back to the manufacturer for maintenance at recommended intervals	- Send mass flow controllers back to the manufacturer for maintenance at recommended intervals	
22	Ignition	- Should ignite the	- Cannot run the rig	- Follow the detailed	- Test ignition	- After the room	

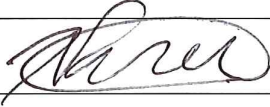| Project: Combustion Instabilities in Annular Combustors | | | | | Page | |
Node: 1 Annular Combustor (Main test rig)						
Ref	Guideword	Causes	Consequences	Safeguards	Recommendations	Action	Date/Sign
		combustible fuel-air mixture in the combustor - If not igniting the ignition conditions are not met	hot - Build-up of combustible gas in the laboratory room	shut down procedure within 5 seconds of opening the fuel supply if the combustor does not ignite - Exhaust ventilator to extract the unburnt fuel from the laboratory room	equipment before opening the fuel supply - Follow the shut-down procedure step by step	has been ventilated well check ignition equipment - Check there is fuel in the fuel canister	
23	Spare equipment	NA					
24	Safety						

ATTACHEMENT D: HAZOP PROCEDURE (TEMPLATE)

Project: Combustion Instabilities in Annular Combustors					Page		
Node: 1 Annular Combustor (Main test rig)							
Ref#	Guideword	Causes	Consequences	Safeguards	Recommendations	Action	Date/Sign
	Not clear procedure	Procedure is too ambitious, or confusingly	- Potential flame flashback - Potentially no ignition	- Emergency shut-down button to cut fuel supply		- Shut off fuel supply to the rig	
	Step in the wrong place	The procedure can lead to actions done in the wrong pattern or sequence	- Potential flame flashback - Potentially no ignition	- Emergency shut-down button to cut fuel supply		- Shut off fuel supply to the rig	
	Wrong actions	Procedure improperly specified	- Potential flame flashback - Potentially no ignition	- Emergency shut-down button to cut fuel supply		- Shut off fuel supply to the rig	
	Incorrect information	Information provided in advance of the specified action is wrong	- Potential flame flashback - Potentially no ignition	- Emergency shut-down button to cut fuel supply		- Shut off fuel supply to the rig	
	Step missing	Missing step, or step requires too much of operator	- Potential flame flashback - Potentially no ignition	- Emergency shut-down button to cut fuel supply		- Shut off fuel supply to the rig	
	Step unsucessful	Step has a high probability of failure	- Potential flame flashback - Potentially no	- Emergency shut-down button to cut fuel supply		- Shut off fuel supply to the rig	

6

Ref#	Guideword	Causes	Consequences	Safeguards	Recommendations	Action	Date/Sign
Project: Combustion Instabilities in Annular Combustors **Node: 1 Annular Combustor (Main test rig)**						**Page**	
			ignition				
	Influence and effects from other	Procedure's performance can be affected by other sources	- Potential flame flashback - Potentially no ignition	- Emergency shut-down button to cut fuel supply		- Shut off fuel supply to the rig	

ATTACHMENT E: PROCEDURE FOR RUNNING EXPERIMENTS

Prosjekt **Combustion Instabilities in Annular Combustors**	Dato	Signatur
Apparatur Annular Combustor		
Prosjektleder Nicholas Worth	25/1/18	*(signature)*

	Conditions for the experiment:	Completed
	Experiments should be run in normal working hours, 08:00-16:00 during winter time and 08.00-15.00 during summer time. Experiments outside normal working hours shall be approved.	
	One person must always be present while running experiments, and should be approved as an experimental leader.	
	An early warning is given according to the lab rules, and accepted by authorized personnel.	
	Be sure that everyone taking part of the experiment is wearing the necessary protecting equipment and is aware of the shut-down procedure and escape routes.	
	Preparations	**Carried out**
	Post the "Experiment in progress" sign.	
	Start-up procedure: 1. Check the access to the door is not blocked and that the general laboratory environment is safe for experimental work 2. Turn on the exhaust ventilator 3. Check if CO alarm is working and check gas levels 4. Check if the annular combustor is securely placed under the exhaust ventilator and that there are no flammable materials near the burner exit 5. Ensure fuel cylinder is securely fastened 6. Visually check condition of fuel and air delivery system (regulators, mass flow controllers, delivery line, threaded fittings) and the combustor 7. Check emergency shut-off circuit is working and that the fuel solenoid valve is connected to the emergency shut-off circuit 8. Turn on primary air supply to the burner and leak test all the joints at working pressure. Pressure is adjusted at the regulator in the incoming air supply line, flow rate is adjusted at the mass flow controllers 9. Open fuel supply regulator and set the flow rate at the mass flow controller 10. Leak test all threaded joints at working pressure 11. Ignite mixture at arms length with a low voltage glow plug or a gas torch. Check that the flame ignites. If not, perform the shutdown procedure	

	During the experiment	
	- Only do short hot runs (1-2 minutes) with breaks in between (10 minutes)	
	- Extinguish the combustor by setting fuel mass flow rate to zero at mass flow controller	
	- During the breaks air should be sent through the rig to allow it to cool between runs	
	- The rig should be monitored at ALL times when run hot	
	End of experiment	
	Shut down procedure:	
	1. Shut off the fuel supply to the rig	
	2. Reduce air volume flow, leaving some air on and allow test rig to cool	
	3. Close fuel supply cylinder, and purge fuel supply lines	
	4. Shut off air flow	
	5. Leave exhaust ventilator ON for a sufficient duration to allow the room to ventilate	
	6. Shut off exhaust ventilator	
	Remove all obstructions/barriers/signs around the experiment.	
	Tidy up and return all tools and equipment.	
	Tidy and cleanup work areas.	
	Return equipment and systems back to their normal operation settings (fire alarm)	
	To reflect on before the next experiment and experience useful for others	
	Was the experiment completed as planned and on scheduled in professional terms?	
	Was the competence which was needed for security and completion of the experiment available to you?	
	Do you have any information/ knowledge from the experiment that you should document and share with fellow colleagues?	

Operator(s):

Navn	Dato	Signatur
Tomas Falkhytten	25/1/2018	*Tomas Falkhytten*

NTNU ◉ SINTEF

ATTACHMENT F: TRAINING OF OPERATORS

Prosjekt Combustion instabilities in Annular Combustors	Dato	Signatur
Apparatur Annular Combustor		
Prosjektleder Nicholas Worth		

	Knowledge about EPT LAB in general	
	Lab • Access • routines and rules • working hour	
	Knowledge about the evacuation procedures.	
	Activity calendar for the Lab	
	Early warning, **iept-experiments@ivt.ntnu.no**	
	Knowledge about the experiments	
	Procedures for the experiments	
	Emergency shutdown.	
	Nearest fire and first aid station.	
	Use of Ethylene • Read MSDS for Ethylene • Storage and use • How to use recommended protective equipment	
	Use of Methane • Read MSDS for Methane • Storage and use • How to use recommended protective equipment	
	Training in usage of the rig (air supply, fuel supply, mass flow controllers, igniting the rig, shutdown procedure, leak detection)	

I hereby declare that I have read and understood the regulatory requirements has received appropriate training to run this experiment and are aware of my personal responsibility by working in EPT laboratories.

Operator(s):

Navn	Dato	Signatur
Tomas Falkhytten	25/1/2018	*Tomas Falkhytten*

10
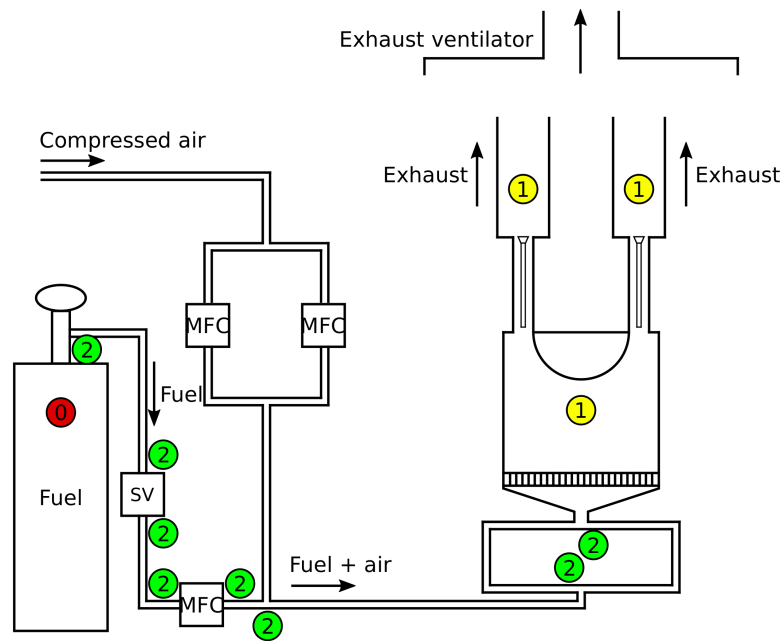
Figure 2: The figure shows a schematic ATEX diagram of the experimental setup. SV is a solenoid valve and MFC is mass flow controllers. The atmosphere in zone 0 is always explosive which is the case inside the fuel tank. In zone 1 the atmosphere is explosive sometimes and in zone 2 it is usually not explosive, but it could happen by accident. All the threaded joints in the rig has the potential to leak and cause an explosive atmosphere by accident, and is thus classified as zone 2.

APPARATURKORT / UNITCARD

Dette kortet SKAL henges godt synlig på apparaturen!
This card MUST be posted on a visible place on the unit!

Apparatur (Unit)	
Prosjektleder (Project Leader)	**Telefon mobil/privat** (Phone no. mobile/private)
Apparaturansvarlig (Unit Responsible)	**Telefon mobil/privat** (Phone no. mobile/private)
Sikkerhetsrisikoer (Safety hazards)	
Sikkerhetsregler (Safety rules)	
Nødstopp prosedyre (Emergency shutdown)	

Her finner du (Here you will find):

Prosedyrer (Procedures)	aaa
Bruksanvisning (Users manual)	bbb

Nærmeste (Nearest)

Brannslukningsapparat (fire extinguisher)	aaaa
Førstehjelpsskap (first aid cabinet)	bbbb

NTNU
Institutt for energi og prosessteknikk

SINTEF Energi
Avdeling energiprosesser

Dato

Dato

Signert

Signert

FORSØK PÅGÅR /EXPERIMENT IN PROGRESS

Dette kortet SKAL henges opp før forsøk kan starte!
This card MUST be posted on the unit before the experiment startup!

Apparatur (Unit)	
Prosjektleder (Project Leader)	**Telefon mobil/privat** (Phone no. mobile/private)
Apparaturansvarlig (Unit Responsible)	**Telefon mobil/privat** (Phone no. mobile/private)
Godkjente operatører (Approved Operators)	**Telefon mobil/privat** (Phone no. mobile/private)
Prosjekt (Project)	
Forsøkstid / Experimental time (start - stop)	
Kort beskrivelse av forsøket og relaterte farer (Short description of the experiment and related hazards**)**	

NTNU
Institutt for energi og prosessteknikk

Dato

_____

Signert

_____

SINTEF Energi
Avdeling energiprosesser

Dato

_____

Signert

_____